

学位論文

Probing the Structure of Ultra-fast Outflows
in Active Galactic Nuclei with X-ray Spectroscopy

(X線分光を用いた活動銀河核における超高速噴出流の構造の研究)

平成 26 年 12 月博士（理学）申請

東京大学大学院理学系研究科
物理学専攻
萩野 浩一

Probing the Structure of Ultra-fast Outflows in Active Galactic Nuclei with X-ray Spectroscopy

Kouichi Hagino

A Thesis presented for the degree of
Doctor of Philosophy

Department of Physics
Graduate School of Science
University of Tokyo

December 18, 2014

Abstract

The ultra fast outflows (UFOs) in active galactic nuclei (AGN) are potentially the most effective process for transporting energy to their host galaxies, so that they are considered to play an important role in the coevolution of supermassive black holes and galaxies. However, the launching and accelerating mechanisms of UFOs are still unknown. An interesting and possibly important feature of UFOs is their varies spectra. For example, PDS 456, which is known with its strongest UFO feature, shows strong variability of absorption lines in a time scale of as short as a few days. Similar variability seems to exist in the other UFO candidates. Therefore, this variability is probably caused by a common essential physical property of UFOs. In order to reveal the physical origin of the various spectra of the UFOs, we constructed a new Monte Carlo simulation code to self-consistently calculate X-ray spectra reprocessed in an assumed 3-dimensional disk wind geometry, and used it for the spectral analysis of the observational UFO data.

By using our Monte Carlo simulations, we analyzed multi-epoch observational data of PDS 456 and APM 08279+5255, which are well known as showing strong UFO feature. We successfully reproduced all the spectra observed in different epochs by our simulation model. For both sources, all the fundamental parameters were found to be largely unchanged, with only a change in the relative angle between the line of sight and outflowing direction sufficient to explain the observations. This result indicates that the variability of the UFO spectra is explained by the instability of the outflowing direction of the wind. This is predicted by the hydrodynamic simulations of the UV line driven disk wind, but is for the first time strongly indicated based on the observational data. The obtained best estimates of the physical parameters of the UFOs in PDS 456 and APM 08279+5255 showed similar values between the two sources, and we found these values can be explained under the UV line driving scenario.

We next analyzed a peculiar AGN 1H 0707-495 showing a sharp spectral drop above ~ 7 keV, by using our disk wind model. Many works has tried to explain the origin of this spectral feature, but no one has tried to explain its spectra in the context of UFOs. We tried to reproduce the peculiar spectra by our simulations, and obtained a model giving acceptably good fits to all the observed spectra. Thus, the spectral drop in 1H 0707-495 can be explained as originating in UFOs. The obtained physical parameters are similar to PDS 456 and APM 08279+5255, indicating that the UFOs can be launched in both low mass black holes like 1H 0707-495 and high mass black holes such as PDS 456 and APM 08279+5255. Alternatively, we tried a wind model with a large turbulent velocity and a slower terminal velocity, which also gave acceptable fit statistics. This model is interpreted as a “failed wind” which is theoretically expected from the UV line driving

mechanism.

From the analysis of 3 AGN with our Monte Carlo simulations, we revealed that the various spectra of UFOs is explained by a difference of relative angles between our line of sight and outflowing angle of the wind. Also, their similarity despite a large difference of black hole mass suggests that the UV line driving is not likely to be dominant in UFOs. However, if the wind in 1H 0707-495 is a “failed wind”, all the observed spectra are understood under the UV line driving scenario.

Contents

Abstract	ii
1 Introduction	1
2 Accretion disk winds from supermassive black holes	3
2.1 Active Galactic Nuclei	3
2.1.1 Observational classifications and unified scheme	3
2.1.2 Estimating black hole masses	5
2.1.3 Eddington luminosity and Eddington accretion rate	7
2.1.4 Radiation from a standard accretion disk	8
2.1.5 X-ray spectrum of AGN	9
2.2 Observations of AGN outflows	10
2.2.1 Importance of the AGN winds	10
2.2.2 BAL and warm absorbers	12
2.2.3 Ultra-fast outflows	13
2.2.4 Wind driving mechanisms	15
2.2.5 P-Cygni profiles as a probe of the wind	17
2.3 Radiation Processes	19
2.3.1 Photoionized plasma	19
2.3.2 Photon interactions with photoionized plasma	20
3 Instrumentation	27
3.1 The <i>Suzaku</i> Observatory	27
3.1.1 X-ray Telescope (XRT)	29
3.1.2 X-ray Imaging Spectrometer (XIS)	29
3.2 The <i>XMM-Newton</i> Observatory	31
3.2.1 X-ray telescopes	34
3.2.2 European Photon Imaging Camera (EPIC)	34

4	Disk wind model and calculation of the spectrum	37
4.1	Approach to Radiative Transfer	37
4.1.1	Emission and absorption lines	37
4.1.2	Radiation transfer in a realistic geometry	38
4.2	Monte Carlo simulation	40
4.2.1	MONACO framework	40
4.2.2	Atomic processes	40
4.2.3	Relativistic effects	45
4.3	Wind geometry	47
4.4	Ionization structure	50
4.5	Comparison with previous work	51
4.5.1	Ionization structures	52
4.5.2	Doppler beaming	53
4.6	Phenomenological model for parameter search	56
4.6.1	Model description	56
4.6.2	Extraction of physical parameters of AGN winds from the spectral parameters	58
4.7	Application to observational data	59
5	Analysis of PDS 456	63
5.1	Observational data	63
5.2	Spectral characterization	64
5.2.1	Gaussian absorption and emission	64
5.2.2	Physical absorption lines: KABS and Gaussian emission	65
5.2.3	Absorption accompanied by emission: PCYGX	67
5.3	Comparison of the Monte Carlo simulations and the 2007 spectra	69
5.3.1	Parameter choice	69
5.3.2	Absorption lines	72
5.3.3	Emission lines from the wind	78
5.3.4	Emission lines from the wind and reflection from the disk	78
5.4	Study of variability in absorption lines	79
5.4.1	Variability in continuum spectra and absorption lines	79
5.4.2	Modeling the variability with MONACO	84
5.5	Summary	89
6	Analysis of APM 08279+5255	91
6.1	Observational data	91

6.2	Comparison of the Monte Carlo simulations and the 2002 spectra	92
6.2.1	Parameter choice	92
6.2.2	Parameter constraints of the 2002 spectrum	96
6.3	Study of the spectral variability	99
6.4	Searching of a large parameter space with a phenomenological model . .	101
6.5	Summary of the analysis of APM 08279+5255	104
7	Discussion on the accretion disk winds in high mass AGN	107
7.1	Instability of the wind geometry	107
7.2	Inhomogeneous wind	110
7.3	Launching mechanism of UFOs	111
7.3.1	Can UFOs be launched by UV line driving?	111
7.3.2	Prediction of the relation between black hole mass and UFO ac- celeration	113
7.4	Future prospects	114
8	Disk wind interpretation of peculiar spectra in 1H 0707-495	117
8.1	Observational data	117
8.2	Parameter estimation with the phenomenological model	119
8.3	Comparison with the Monte Carlo simulations of the disk wind	122
8.4	Solution of the failed wind	126
8.5	Discussion on the peculiar spectral drop	131
8.5.1	Self-similar disk wind	131
8.5.2	The failed wind in UV-line driving model	131
9	Conclusion	135
	Acknowledgements	145

List of Figures

2.1	Typical X-ray spectrum of unobscured AGN (a thick black line). The primary X-ray continuum absorbed by warm absorber, soft excess, reflection hump and a Fe $K\alpha$ emission line are shown in magenta, cyan, green and red, respectively. The components are described in more detail in the text. This figure is taken from Risaliti & Elvis (2004)	9
2.2	M - σ relation. This figure is taken from Gültekin et al. (2009).	11
2.3	Spectrum of warm absorber in IRAS 13349+2438 observed by <i>XMM-Newton</i> /RGS. Absorption lines labeled in blue are lowly ionized component ($\xi \sim 1$ –2), while lines labeled in black are highly ionized component ($\xi \sim 2.0$ –2.5). Low- ξ lines are blue shifted with $v \sim 400$ km s $^{-1}$. This figure is taken from Sako et al. (2001).	13
2.4	The distributions of the column density N_{H} , the outflow velocity v_{out} and the ionization parameter ξ in UFOs. Blue and black vertical lines indicate the mean values of <i>XMM-Newton</i> and <i>Suzaku</i> analyses respectively. This figure is taken from Gofford et al. (2013).	14
2.5	A schematic view of the formation of P-Cygni profile. This figure is taken from Owocki (2000).	17
2.6	A schematic view of Sobolev approximation. A photon with an energy slightly smaller than a line (bound-bound) transition energy does not interact with the wind until the redshifted photon energy in the rest frame of the wind matches the transition energy. In a rapidly accelerating wind, such a photon is absorbed at a local point within a Sobolev length l_{Sob} . This figure is taken from Owocki (2004).	18
2.7	Fluorescence yields for K, L, and M shells for $3 \leq Z \leq 110$. The plotted curves for the L and M shells represent average subshell effective yields. This figure is taken from Thompson et al. (2009).	22
3.1	Schematic view (left) and side view (right) of <i>Suzaku</i> taken from Mitsuda et al. (2007)	28

3.2	Effective area of XRT taken from Serlemitsos et al. (2007).	30
3.3	Quantum efficiency of XIS taken from Koyama et al. (2007).	31
3.4	Energy resolutions of the XIS FI (XIS 2) taken from Koyama et al. (2007)	32
3.5	XIS background counting rate as a function of energy. The background rate of <i>ASCA</i> , <i>Chandra</i> and <i>XMM-Newton</i> adopted from Katayama et al. (2004) are shown for comparisons. This figure is taken from Mitsuda et al. (2007).	32
3.6	Sketch of <i>XMM-Newton</i> taken from Jansen et al. (2001).	33
3.7	Effective area taken from <i>XMM-Newton</i> Users Handbook.	34
3.8	Quantum efficiency of MOS1 and pn. the figure for MOS1 is taken from <i>XMM-Newton</i> Users Handbook, and that for pn is taken from Strüder et al. (2001).	35
3.9	Light curve of a MOS1 observation affected by soft proton flares. This figure is taken from <i>XMM-Newton</i> Users Handbook.	36
4.1	The spectra from a spherically symmetric outflow with a velocity of $0.3c$. The direct (transmitted) components are plotted in red, the reprocessed components are in blue and the sums of these components are in black.	38
4.2	Schematic concept of the Monte Carlo simulation. This figure is taken from Odaka et al. (2011).	41
4.3	Comparison of the spectra calculated by MONACO (black) and XSTAR (red). Ionization parameter is a typical value for UFOs, $\log \xi = 4$. The turbulent velocity is $v_t = 0 \text{ km s}^{-1}$. <i>Top</i> : Rebinned to 10 times of the original bin size of XSTAR spectra. <i>Bottom</i> : Plotted in original bin size of XSTAR spectra.	42
4.4	Comparison of the spectra calculated by MONACO (black) and XSTAR (red). All parameters are same as Fig. 4.3 except for the turbulent velocity $v_t = 500 \text{ km s}^{-1}$	45
4.5	The top panel shows the MONACO spectra from the spherical shell with an outflow velocity of $0.3c$ observed from the various angles of $\cos \theta = 0.975$ (black), 0.525 (red), 0.025 (green), -0.475 (blue) and -0.975 (magenta). The data points are the simulated spectra and the lines are the best fit functions. In the bottom panel, Doppler factor obtained by fitting the simulated spectra are plotted against $\cos \theta$. The red curve is the expected function (Eq. 4.3).	46

4.6	The schematic view of the bi-conical wind geometry (Shlosman & Vitello, 1993), which is adopted in our model. The cyan region is filled with the outflowing materials.	47
4.7	Adopted geometry for our wind model and geometric variables. The shaded region is filled with outflowing material. The wind is rotationally symmetric about the z-axis.	48
4.8	The geometry used for ionization calculation.	51
4.9	Distributions of mean Fe ionization state and kinetic temperature. The upper panel shows the mean charge states of Fe atoms (left) and the electron temperature (right) in the wind structure. The bottom panel is the same figures as the top panel but calculated by Sim et al. (2010a). Please be careful of the difference of the color definitions between top and bottom panels.	54
4.10	The simulated spectra for a various viewing angles ($\mu \equiv \cos \theta = 0.875, 0.675, 0.575, 0.475$ and 0.275) by the wind model in Sim et al. (2010a) (left) and our wind model (right). The direct components are plotted in red, the reprocessed components are in blue and the sums of these components are in black.	55
4.11	Schematic view of the phenomenological model for the parameter search. The absorption lines of the Fe XXV and Fe XXVI ions for the Doppler factors of $\delta = 1.32$ (red), 1.34 (green) and 1.36 (blue) are plotted with the dotted lines. The black solid line is the phenomenological model, which is convolved with the different velocity components of $\delta = 1.32$ – 1.36	57
4.12	Dependence of the mean Doppler factor δ_0 and the width of the Doppler factor $\Delta\delta$ on the terminal velocity v_∞ and the relative angle $\theta_{\text{incl}} - \theta_{\text{min}}$. These maps are used to translate the spectral parameters (δ_0 and $\Delta\delta$) to the physical parameters (v_∞ and $\theta_{\text{incl}} - \theta_{\text{min}}$).	59
4.13	A variety of spectra simulated by MONACO. Each panel shows the spectra observed at a different line-of-sight orientation angle. The red, blue and black lines represent the direct components, reprocessed components and their sum, respectively. The parameters for these spectra are the same as the model for PDS 456: the terminal velocity is $v_\infty = 0.3c$ and the mass outflow rate is $\dot{M}_{\text{wind}}/\dot{M}_{\text{Edd}} = 0.13$	60
5.1	<i>Suzaku</i> spectra (black points) fitted with the Gaussian emission and absorption model (red solid line). The lower panel shows the residuals in units of χ . The spectra are shown in the rest frame of PDS 456.	65

5.2	<i>Suzaku</i> spectra (black points) fitted with KABS and Gaussian emission (red line). The lower panel shows the residuals in units of χ . The spectra are shown in the rest frame of PDS 456.	68
5.3	<i>Suzaku</i> spectra (black points) fitted with PCYGX (red line). The lower panel shows the residuals in units of χ . The spectra are shown in the rest frame of PDS 456.	69
5.4	MONACO spectra with $L = 4 \times 10^{44}$ erg s ⁻¹ , $\dot{M} = 10 M_{\odot}$, $v_0 = v_{\text{turb}} = 1000$ km s ⁻¹ , $\beta = 1$ and $R_{\text{min}} = 20R_g$. The direct component and re-processed component are plotted in red and blue respectively. The total spectrum is plotted in black. Y-axis is normalized to the input powerlaw spectrum.	73
5.5	Ratio of H-like to He-like iron through the wind, together with the lines of sight for $\theta_{\text{incl}} = 46^\circ, 50^\circ, 54^\circ$ and 70° for the same simulation as in Fig. 5.4, labeled with the total column density along that line of sight. Higher inclination samples material at smaller radii, where it is still accelerating so the density is higher hence the abundance of He-like iron is higher. .	73
5.6	<i>Top</i> : <i>Suzaku</i> data and MONACO spectrum with $L = 4 \times 10^{44}$ erg s ⁻¹ , $\dot{M} = 10 M_{\odot}$ yr ⁻¹ , $v_0 = v_{\text{turb}} = 1000$ km s ⁻¹ , $\beta = 1$ and $R_{\text{min}} = 20R_g$. Best fit parameters are $z = 0.165 \pm 0.007$ ($v \simeq 0.315c$), $\theta_{\text{incl}} = 49.0 \pm 0.9^\circ$ and $\Gamma = 2.35(\text{fix})$. Fit statistic is $\chi^2/\text{dof} = 32.32/27$. <i>Bottom</i> : Same figure as the left panel except with $L = 1 \times 10^{44}$ erg s ⁻¹ . Best fit parameters are $z = 0.174 \pm 0.005$ ($v \simeq 0.308c$), $\theta_{\text{incl}} = 47.1 \pm 0.4^\circ$ and $\Gamma = 2.35(\text{fix})$. Fit statistic is $\chi^2/\text{dof} = 21.48/27$. All spectra are shown in the rest frame of PDS 456.	74
5.7	Dependence on the ionizing luminosity. The grey, magenta and cyan lines show the fiducial parameter simulation with $L = 4 \times 10^{44}$ erg s ⁻¹ , $\dot{M} = 10 M_{\odot}$ yr ⁻¹ , while the black, red and blue curves show the same parameters except with an ionizing luminosity $L = 1 \times 10^{44}$ erg s ⁻¹	76
5.8	Ratio of H-like to He-like iron through the wind, together with the lines of sight for $\theta_{\text{incl}} = 46^\circ, 50^\circ, 54^\circ$ and 70° for the same simulation as in Fig. 5.7, labeled with the total column density along that line of sight. H-like ion is smaller than Fig. 5.5.	77
5.9	<i>Suzaku</i> data and MONACO spectrum in 2-10 keV band with $L = 1 \times 10^{44}$ erg s ⁻¹ , $\dot{M} = 10 M_{\odot}$ yr ⁻¹ , $v_0 = v_{\text{turb}} = 1000$ km s ⁻¹ , $\beta = 1$ and $R_{\text{min}} = 20R_g$. Best fit parameters are $\theta_{\text{incl}} = 47.3 \pm 0.4^\circ$ and $\Gamma = 2.33 \pm 0.01$, and the redshift is fixed at $z = 0.174$ ($v \simeq 0.308c$). Fit statistic is $\chi^2/\text{dof} = 106.49/105$	77

- 5.10 *Top* : *Suzaku* data and MONACO spectrum in 2-10 keV band with $L = 1 \times 10^{44}$ erg s $^{-1}$, $\dot{M} = 10 M_{\odot}$ yr $^{-1}$, $v_0 = v_{\text{turb}} = 1000$ km s $^{-1}$, $\beta = 1$, $R_{\text{min}} = 20R_g$ and $\theta_{\text{min}} = 35^{\circ}$. Best fit parameters are $\theta_{\text{incl}} = 37.4 \pm 0.4^{\circ}$, $\Gamma = 2.30 \pm 0.01$, and the redshift is fixed at $z = 0.174$ ($v \simeq 0.308c$). Fit statistic is $\chi^2/\text{dof} = 103.62/105$. *Bottom* : *Suzaku* data and MONACO spectrum with blurred disk reflection (black dotted line at the bottom of the spectrum) in 2-10 keV band with $L = 1 \times 10^{44}$ erg s $^{-1}$, $\dot{M} = 10 M_{\odot}$ yr $^{-1}$, $v_0 = v_{\text{turb}} = 1000$ km s $^{-1}$, $\beta = 1$, $R_{\text{min}} = 20R_g$ and $\theta_{\text{min}} = 55^{\circ}$. Best fit parameters are $\theta_{\text{incl}} = 56.8 \pm 0.3^{\circ}$, $\Gamma = 2.40 \pm 0.04$ and reflection fraction $R \simeq 0.27$, and the redshift is fixed at $z = 0.174$ ($v \simeq 0.308c$). Fit statistic is $\chi^2/\text{dof} = 103.91/104$. We changed the y-axis scale to show the reflected spectrum. All spectra are shown in the rest frame of PDS 456. 80
- 5.11 *Suzaku* XIS FI spectra from 2007 (black), 2011 (red), 2013a (green), 2013b (blue) and 2013c (cyan), unfolded against $\Gamma = 2$ powerlaw. All spectra are shown in the rest frame of PDS 456. 81
- 5.12 *Suzaku* spectra (black points) of PDS 456 fitted with KABS*ZXIPCF*(POWERLAW+GAUSS) (red line). From top left, the spectra of 2011, 2013a, 2013b and 2013c are plotted. The continuum spectra are modeled by the power law with the ionized partial covering absorber ZXIPCF. The additional Fe absorption lines and the Fe emission line are modeled with the KABS model and a Gaussian. 82
- 5.13 Contour plots of the wind outflowing angle θ_{min} and the terminal velocity v_{∞}/c for all the observations (2007, 2011, 2013a, 2013b and 2013c). The contours shown in red, green and cyan represent confidence levels of 68% ($\simeq 1\sigma$), 90% and 99%, respectively. 86
- 5.14 The best fit MONACO spectra (red line) with $\dot{M}_{\text{wind}} = 8 M_{\odot}$ yr $^{-1}$ and *Suzaku* spectra (black points) for 2011, 2013a, 2013b and 2013c. The lower panel shows the residuals in units of χ . All spectra are shown in the rest frame of PDS 456. 88
- 6.1 *XMM-Newton* spectra (black points) fitted with an absorbed power law model (red lines). The lower panels show the residuals in units of χ 93

6.2	<p><i>XMM-Newton</i> spectra of APM 08279+5255 fitted with the MONACO model used for PDS 456. The spectra obtained by the MOS detectors and their models are plotted in red and green, respectively. The data points and the line shown in black are the data and model for the pn camera. The mass outflow rate is lower ($\dot{M}_{\text{wind}} = 3 M_{\odot} \text{ yr}^{-1}$) and the inclination angle is higher ($\theta_{\text{incl}} = 68.9^{\circ}$) compared with the best fit values for PDS 456.</p>	95
6.3	<p>Spectra and best fit model with $v_{\infty} = 0.3c$, $\dot{M}_{\text{wind}} = 50 M_{\odot} \text{ yr}^{-1}$. <i>Left:</i> pn (black), MOS1 (red) and MOS2 (green) spectra and model. <i>Right:</i> pn zoom-in spectrum and model.</p>	96
6.4	<p>Spectra and best fit model with $v_{\infty} = 0.4c$, $\dot{M}_{\text{wind}} = 70 M_{\odot} \text{ yr}^{-1}$. <i>Left:</i> pn (black), MOS1 (red) and MOS2 (green) spectra and model. <i>Right:</i> pn zoom-in spectrum and model.</p>	97
6.5	<p>Contour plots of the terminal velocity and the mass outflow rate, fitted with powerlaw model multiplied by the MONACO spectra (left), and the model with an additional reflection component REFLIONX (right). The region filled with red represents the 1-σ confidence level, i.e. the fit statistics are smaller than $\chi_{\text{min}}^2 + 2.3$. The green and cyan regions correspond to 90% and 99% confidence levels respectively.</p>	97
6.6	<p>Spectra and best fit model with $v_{\infty} = 0.3c$, $\dot{M}_{\text{wind}} = 70 M_{\odot} \text{ yr}^{-1}$. The disk reflection component REFLIONX is added. <i>Left:</i> pn (black), MOS1 (red) and MOS2 (green) spectra and model. <i>Right:</i> pn zoom-in spectrum and model.</p>	98
6.7	<p>Spectra and best fit model with $v_{\infty} = 0.4c$, $\dot{M}_{\text{wind}} = 70 M_{\odot} \text{ yr}^{-1}$ for all the <i>XMM-Newton</i> observations (2001, 2002, 2007a and 2007b). The spectra and models of pn, MOS1 and MOS2 are plotted in black, red and green, respectively. The lower panels show the residuals in units of χ.</p>	100
6.8	<p><i>XMM-Newton</i> spectra of APM 08279+5255 observed in 2002 and the best fit model. The model is composed of the absorbed power law and ionized reflection multiplied by the velocity convolved absorption lines and edges. The spectra and models of pn, MOS1 and MOS2 are plotted in black, red and green, respectively.</p>	101
6.9	<p>A contour plot of δ_0 and $\Delta\delta$ for the 2002 spectra. Each line corresponds to 1-σ (black), 90% (red) and 99% (green) significance levels.</p>	103

- 6.10 Contour plot of the relative angle $\Delta\theta$ ($\theta_{\text{incl}} - \theta_{\text{min}}$) and the terminal velocity v_{∞} . The best fit value is shown by a black cross. *Left* : The red region shows a calculated from 90% error for each parameter (δ_0 and $\Delta\delta$). In this plot, correlation between δ_0 and $\Delta\delta$ is not considered. *Right* : The red, green and blue contours represent 1- σ , 90% and 99% confidence levels, respectively. The regions correspond to those shown in Fig. 6.9. 103
- 6.11 The distribution of the column density (left) and the ratio (right) of the H/He-like Fe ions with $\dot{M}_{\text{wind}} = 40 M_{\odot} \text{ yr}^{-1}$ in the 90% confidence interval of v_{∞} and $\Delta\theta$ 104
- 6.12 A projection of the 3-dimensional contour plot of the relative angle $\Delta\theta$ ($\theta_{\text{incl}} - \theta_{\text{min}}$), the terminal velocity v_{∞} and the mass outflow rate \dot{M}_{wind} . The red, yellow, green and blue regions correspond to the 38% ($\sim 0.5\sigma$), 68% ($\sim 1\sigma$), 90% and 99% confidence intervals. 105
- 7.1 Sequence of density maps calculated by axisymmetric time-dependent hydrodynamic simulations of line-driven disk winds. The panels show the density maps at 13.3 (left), 14.6 (middle) and 16.47 yr (right) respectively. This figure is taken from Proga, Stone & Kallman (2000). 108
- 7.2 Time variability of the ranges of the viewing angle obtained by hydrodynamic simulations. The regions where the UFOs are detected are filled with cyan. The solid, dashed and dotted lines represents angles of 72.4°, 65.7° and 77.2°. This figure is taken from Nomura (2014). 108
- 7.3 A velocity field map of the hydrodynamic simulations. Only the poloidal velocity component is plotted. This figure is taken from Proga, Stone & Kallman (2000). 109
- 7.4 Steady structure of the line-driven disk wind for the Eddington ratio of $\epsilon = 0.5$ and black hole mass of $M_{\text{BH}} = 10^8 M_{\odot}$, calculated by a non-hydrodynamical method. This figure is taken from Nomura et al. (2013). 112
- 7.5 Predicted spectral energy distributions for spin zero black holes of mass 10^6 (blue) and $10^9 M_{\odot}$ (red). The black vertical line is at 13.6 eV Hydrogen ionization point which corresponds to the UV line driving bandpass. Here, we use OPTXAGNF (Done et al., 2012) and assume $L/L_{\text{Edd}} = 1$ 114

7.6	The observed (left) and simulated (right) spectra of the radio galaxy 3C 111. The left panel shows the <i>Suzaku</i> spectrum observed in 2008 with a 100 ks exposure time. The spectrum in the right panel is a simulated SXS spectrum with the same exposure time of 100 ks. In the SXS spectrum, the absorption lines of the UFO is clearly detected. These figures are taken from Kaastra et al. (2014).	115
7.7	The expected spectra of the UFOs in the energy range of 5–100 keV calculated by our Monte Carlo simulation. The direct components are plotted in red, the reprocessed components are in blue and the sums of these components are in black.	116
8.1	All spectra observed by <i>XMM-Newton</i> /pn and <i>Suzaku</i> /FI detectors, unfolded against a $\Gamma = 2$ power law.	119
8.2	Best fit model and spectrum of Obs12. Left: ionized reflection REFLIONX, right: Gaussian emission	120
8.3	Contour plots of the physical parameters with the 90% confidence level for the Obs12 spectrum. The result from the model with ionized reflection REFLIONX is shown in red, and Gaussian emission model is in black.	121
8.4	Observed spectrum and MONACO model with $v = 0.2c$ and $\dot{M}_{\text{wind}}/\dot{M}_{\text{Edd}} = 0.20$ for Obs12.	122
8.5	Observed spectra and MONACO models with $v = 0.2c$ and $\dot{M}_{\text{wind}}/\dot{M}_{\text{Edd}} = 0.2$ for all the observations.	124
8.6	Best fit model and spectra of Obs12 with a large turbulence model.	126
8.7	Dependence of $N(\text{Fe XXV} + \text{Fe XXVI})$ on the terminal velocity v_{∞} and relative angle $\theta_{\text{incl}} - \theta_{\text{min}}$. Left panel is for $\dot{M}_{\text{wind}} = 0.025 M_{\odot} \text{ yr}^{-1}$, and right panel is for $\dot{M}_{\text{wind}} = 0.125 M_{\odot} \text{ yr}^{-1}$	127
8.8	Observed spectra and MONACO models with $v = 0.15c$, $v_t = 10000 \text{ km s}^{-1}$ and $\dot{M}_{\text{wind}}/\dot{M}_{\text{Edd}} \simeq 0.5$ for all the observations.	130
8.9	The wind geometry calculated by a non-hydrodynamical method. The failed wind is shown in red lines. This figure is taken from Risaliti & Elvis (2010).	132
8.10	A schematic view of the failed wind in the low mass systems such as narrow line Seyfert 1s. This figure is taken from Gardner & Done (2014).	133

List of Tables

3.1	Specifications of the XRTs. Values are taken from the <i>Suzaku</i> Technical Description.	29
3.2	Specifications of the XISs. Values are taken from the <i>Suzaku</i> Technical Description.	30
3.3	Specifications of the X-ray telescopes onboard <i>XMM-Newton</i> . Values are taken from <i>XMM-Newton</i> Users Handbook	34
3.4	Specifications of the EPIC. Values are taken from <i>XMM-Newton</i> Users Handbook	36
4.1	Comparison of the lines	44
4.2	Parameters of the simulation geometry and the seed photons	49
4.3	Model parameters used for the comparison between our wind model and Sim et al. (2010a)'s wind model.	52
5.1	<i>Suzaku</i> observations of PDS 456	64
5.2	Spectral parameters of Gaussian emission and absorption model for the 2007 spectrum	66
5.3	Spectral parameters of KABS model for the 2007 spectrum	68
5.4	Spectral parameters of PCYGX model for the 2007 spectrum	70
5.5	Model parameters for MONACO simulations of PDS 456.	72
5.6	Spectral parameters for all <i>Suzaku</i> observations	83
5.7	MONACO parameters for all <i>Suzaku</i> observations	87
6.1	<i>XMM-Newton</i> observations of APM 08279+5255	91
6.2	Parameters for APM 08279+5255	95
6.3	Best fit parameters of the MONACO model for all the <i>XMM-Newton</i> observations.	99
6.4	Fitting result of the convolved absorption model	102

7.1	Full numerical calculation of UV-line driven winds. All accretion rates are in units of the Eddington accretion rate. (Shane Davis, private communication)	113
8.1	<i>XMM-Newton</i> and <i>Suzaku</i> observations of 1H 0707-495	118
8.2	Fitting result of Obs12 spectrum with the convolved absorption model	120
8.3	MONACO fit with $v = 0.2c$ and $\dot{M}_{\text{wind}}/\dot{M}_{\text{Edd}} = 0.2$	125
8.4	Fitting result of Obs12 spectrum with the phenomenological absorption model without a velocity convolution ($\Delta\delta = 0$).	127
8.5	MONACO fit with $v = 0.15c$, $v_t = 10000 \text{ km s}^{-1}$ and $\dot{M}_{\text{wind}}/\dot{M}_{\text{Edd}} \simeq 0.5$	129

Chapter 1

Introduction

One of the most unexpected and important discoveries in astrophysics is a tight correlation between the black hole mass M and the velocity dispersion σ of the bulge of its host galaxy, which is called the M - σ relation (e.g., Ferrarese & Merritt, 2000; Merritt & Ferrarese, 2001; Tremaine et al., 2002; Gültekin et al., 2009). This discovery suggests the black holes and their host galaxies coevolve by regulating the growth of each other. This relation requires a process transporting energy from the black hole to its host galaxy.

Accretion disk winds in active galactic nuclei (AGN) are potentially the most effective way of transporting energy and momentum from the nuclear scales to their host galaxy. If winds with kinetic energies of ~ 0.05 of the Eddington luminosity exist, they can quench star formation in the bulge by sweeping away the gas reservoir, and quantitatively reproduce the M - σ relation (e.g., King, 2010). In $\sim 50\%$ of AGN, narrow absorption lines called “warm absorbers” are observed, but they outflows with a moderate velocity of hundreds to few thousand km s^{-1} (Blustin et al., 2005; Piconcelli et al., 2005; McKernan, Yaqoob & Reynolds, 2007). Therefore, this carries only a small fraction of the kinetic energy, as the amount of materials and outflow velocities are both quite small (e.g., Blustin et al., 2005).

Recently, the most powerful outflows called “ultra-fast outflows (UFOs)” are detected as highly ionized absorption lines in X-ray energies. Such winds in a few AGN have substantial column densities of material outflowing at speeds of up to $\sim 0.3c$ (Tombesi et al., 2010; Gofford et al., 2013). These high velocities and high column densities mean the UFO can play an important role in the coevolution of the black holes and galaxies.

However, the launching and acceleration mechanism of the UFOs remain unclear due to the limited sensitivities of current instruments in $\gtrsim 8 \text{ keV}$, where the blue shifted absorption lines of UFOs are observed. Most of the UFO candidates reported in Tombesi et al. (2010) and Gofford et al. (2013) are not detected with significance of $> 3\sigma$, so

that most of them are not appropriate for studying their physical properties in detail. Therefore, in order to study the physical mechanisms of UFOs, a thorough investigation of a few sources with strong UFO features is needed.

The strongest UFO feature is observed in PDS 456, and it shows strong variability of absorption lines in a time scale of as short as a few days (Gofford et al., 2014; Reeves et al., 2014). Such a variability is observed in the other UFO candidates (Tombesi et al., 2010; Gofford et al., 2013), so that it possibly arise from common essential properties of UFOs. Current analysis methods utilizing one-dimensional radiation transfer does not allow us to study the origin of this variability. Thus, a new analysis method is required.

In this thesis, in order to reveal the origin of the various spectra of UFOs depending on the observational epochs, we develop a new Monte Carlo simulation code, which can self-consistently calculate X-ray spectra reprocessed in an assumed 3-dimensional disk wind geometry. We analyze PDS 455 and APM 08279+5255, which show strong features of UFOs, by using our simulations. Also, we analyze an AGN with a peculiar spectral drop above ~ 7 keV, namely 1H 0707-495. The origin of its spectral feature is controversial, but we try to explain their spectra in the context of UFOs.

This thesis is organized in the following order. In Chapter 2, we review the current understanding of accretion disk winds in AGN and important physical processes. Chapter 3 introduces the instruments we used, namely *XMM-Newton* and *Suzaku*. Chapter 4 provides the description on our Monte Carlo simulations. Chapter 5 and 6 are devoted to the analysis results by using our Monte Carlo simulations of PDS 456 and APM 08279+5255, respectively. Chapter 7 discusses the results obtained Chapter 5 and 6. Chapter 8 describes the analysis of a peculiar source 1H 0707-495 by utilizing our wind model. Finally, in Chapter 9, our conclusions are stated. Most of the texts and figures in sections 4.1–4.4 and 7.2 and Chapter 5 are taken from Hagino et al. (2015).

Chapter 2

Accretion disk winds from supermassive black holes

2.1 Active Galactic Nuclei

One of the most remarkable achievements in modern astrophysics is the discovery of the fact that almost all galaxies harbor supermassive black holes (SMBHs) in their centers (e.g., Kormendy & Richstone, 1995; Marconi et al., 2004; Kormendy & Ho, 2013). SMBHs refer to black holes with masses of 10^6 – 10^{10} of solar mass (hereafter represented by M_{\odot}). While most of these are quiescent and can not be observed directly, $\sim 20\%$ of SMBHs show strong activities (e.g., Goulding et al., 2010), which is referred to as “active galactic nuclei” or “AGN” as an abbreviation. Detailed descriptions of observational properties and history of AGN are provided in many texts such as Peterson (1997).

2.1.1 Observational classifications and unified scheme

In general, AGN emits electromagnetic radiation over a range from radio to gamma-ray. Its radiation power in visible light is at least comparable with that of its host galaxy and often exceeds hundred times larger than its host galaxy. Some AGN also luminous in radio band as well as in optical band, while most of AGN are too dim to be undetectable in radio band. Therefore, by using their radio luminosity, AGN are divided in to two subclasses: “radio loud” and “radio quiet”. Majority of AGN are classified as radio quiet AGN and the fraction of radio loud AGN are only $\sim 10\%$ (e.g., Kellermann et al., 1989).

Radio quiet AGN

Historically, radio quiet AGN have been classified in two different classes depending on its B-band ($\lambda = 442$ nm) luminosity. Those with $M_B < -21.5 + 5 \log h_0$ are referred to as quasars, which is typically thought to harbor a 10^8 – 10^9 M_\odot black hole. The less luminous class is called Seyfert galaxies, whose central black hole mass is estimated at 10^6 – 10^7 M_\odot . Here, M_B is the absolute magnitude, h_0 is Hubble constant in units of $\text{km s}^{-1} \text{Mpc}^{-1}$ and $\text{pc} \simeq 3.086 \times 10^{18}$ cm.

Independent from the luminosity, there are two classes based on the optical emission line features. In optical spectra of AGN, broad ($500 \text{ km s}^{-1} \lesssim \text{FWHM} \lesssim 10^4 \text{ km s}^{-1}$) and narrow ($200 \text{ km s}^{-1} \lesssim \text{FWHM} \lesssim 900 \text{ km s}^{-1}$) emission lines are observed. The emission regions of these two kinds of lines are referred to as the broad line region (BLR) and the narrow line region (NLR), which are thought to be main constituents of AGN. AGN showing both broad lines and narrow lines are called “type 1” AGN and those with only narrow lines are called “type 2” AGN. Roughly 3/4 of Seyfert galaxies are classified as type 2, while most of quasars are classified as type 1.

There is a subclass called “narrow line Seyfert 1” showing exceptional emission line properties (e.g., Komossa, 2008). It is defined by relatively narrow broad emission lines and the weakness of narrow forbidden emission lines, namely $\text{FWHM}_{\text{H}\beta} < 2000 \text{ km s}^{-1}$ and $[\text{O III}]/\text{H}\beta_{\text{total}} < 3$ (Osterbrock & Pogge, 1985). Also, the presence of Fe II emission lines, which are usually seen as broad emission lines and not observed in type 2 AGN, is often added to the definition (Véron-Cetty, Véron & Gonçalves, 2001). These characteristics are generally considered as the results of nearly Eddington mass accretion on to the less massive black holes with $M_{\text{BH}} \sim 10^6$ M_\odot . This hypothesis is supported by X-ray observations, where strong soft X-ray excesses indicating nearly or super Eddington accretion disks are detected (e.g., Pounds, Done & Osborne, 1995; Wang & Netzer, 2003; Dewangan et al., 2007; Jin, Ward & Done, 2012, see also section 2.1.5).

Radio loud AGN

There are also subclasses in radio loud AGN, which are radio galaxies and blazars. In blazars, a jet axis is thought to lie close to our line of sight, resulting the strong jet emission enhanced by the Doppler beaming effect. Since the emission in blazars are dominated by the jet emission, blazars exhibit no or very weak emission lines.

Radio galaxies are believed to be misaligned blazars. Unlike blazars, radio galaxies shows emission lines like radio quiet AGN in optical band. By using emission line properties, radio galaxies are divided into two subclasses: broad-line radio galaxies (BLRGs) and narrow-line radio galaxies (NLRGs), which correspond to type 1 and type 2 in radio

quiet AGN respectively.

Unified scheme

Type 1 and type 2 AGN are widely accepted as the same one with different viewing angles. This idea is called unified model or unified scheme (Antonucci, 1993; Urry & Padovani, 1995). In this model, an optically thick absorber called “dusty torus” is introduced to explain their observational differences. If an observer’s line of sight is intercepted by the torus, all radiations emitted from the vicinity of the black hole (broad emission lines and optical/UV/X-ray emissions) are obscured and only narrow emission lines are directly observed. On the other hand, if the line of sight is not obstructed by the torus, all the radiations including both broad emission lines and narrow emission lines are observed. In the unified model, it is thought that type 2 AGN are in the former case and type 1 AGN are in the latter case.

This model is supported by a lot of observational results. The most remarkable one is the polarimetric observation of a type 2 Seyfert galaxy named NGC 1068 (Antonucci & Miller, 1985). In this observation, broad emission lines are detected from the polarized spectrum, which indicates that BLR also exists in type 2 AGN but just obscured by torus. In addition to this, in X-ray band, type 2 Seyfert galaxies are less luminous than type 1 (e.g., Lawrence & Elvis, 1982), and they show a low energy cutoff due to photoelectric absorption (e.g., Awaki et al., 1991). These results are thought to be due to absorption by torus.

Finally, we summarize the typical scales of constituents in the unified model. The observational fact that the broad line is seen in the only allowed line while the narrow line is seen in both of allowed and forbidden lines (see also section 2.3) indicate that the BLR cloud is a fast moving ($\Delta v \sim 5000 \text{ km s}^{-1}$) and high density ($n_e \gtrsim 10^9 \text{ cm}^{-3}$) material. By using the density and the line luminosity, the sizes of BLR and NLR in typical Seyfert galaxies with $M_{\text{BH}} \sim 10^7 M_{\odot}$ are estimated as $\sim 10^{16} \text{ cm}$ ($\sim 10^4 R_g$) and $\gtrsim 10^{18} \text{ cm}$ ($\sim 10^6 R_g$) respectively. Here, R_g is the gravitational radius, whose definition is described in section 2.1.3. The lower limit of the size of torus is estimated as the dust sublimation radius $\sim 10^{17} \text{ cm}$ ($\sim 10^5 R_g$). The emission region of X-ray is thought to locate much closer to the black hole because the hot electrons with temperature of $\sim 100 \text{ keV}$ are needed to generate X-ray radiation (see also section 2.1.5).

2.1.2 Estimating black hole masses

The mass of a black hole is the most fundamental quantity of AGN. The most accurate way to estimate the black hole mass is to directly measure the gas and stellar motion near

the black hole. Also, by using the proper motion of water masers, the black hole mass can be estimated (e.g., Miyoshi et al., 1995). However, in practice, both of these methods are not applicable for most of AGN because it is impossible to spatially resolve the stellar objects or water masers in distant galaxies. Alternatively, there is a way to directly estimate the black hole mass of such distant AGN, and this method is referred to as a reverberation mapping (e.g., Blandford & McKee, 1982). In principle, the reverberation mapping is applicable to all type 1 AGN because it requires only the continuum radiation from the accretion disk and the broad emission lines. Therefore, this reverberation mapping method and an indirect method based on this are widely used to estimate the black hole mass, and these methods are summarized in this section. This subject is reviewed in more detail in Peterson (2013).

Reverberation mapping

Theoretically, reverberation mapping is a technique to obtain the transfer function $\Psi(V_{\text{LOS}}, \tau)$ by using the transfer equation

$$\Delta L(V_{\text{LOS}}, t) = \int \Psi(V_{\text{LOS}}, \tau) \Delta C(t - \tau) d\tau, \quad (2.1)$$

where $\Delta L(V_{\text{LOS}}, t) = L(V_{\text{LOS}}, t) - \langle L(V_{\text{LOS}}) \rangle$ and $\Delta C(t) = C(t) - \langle C \rangle$ are the emission-line variation and the continuum variation, respectively. V_{LOS} is the line-of-sight velocity and τ is the time delay between the continuum variation and the emission line variation, which corresponds to the radius of the emission region.

By applying this method to the broad emission lines, the product $\Delta V^2 \tau$ was revealed to be constant within a given source. Here, ΔV^2 is the line width. This result strongly suggests the BLR is virialized. Therefore, the black hole mass is obtained by

$$M_{\text{BH}} = \frac{R_{\text{BLR}} \Delta V^2}{G} = \frac{f c \tau \Delta V^2}{G}, \quad (2.2)$$

where f is a dimensionless factor of order unity, and represents the effect of the BLR geometry, kinematics, and inclination.

The reverberation mapping was mathematically formalized by Blandford & McKee (1982). Then reverberation mappings have been performed successfully, giving black hole masses for several tens of local AGN (e.g., Wandel, Peterson & Malkan, 1999; Kaspi et al., 2000; Nelson, 2000; Peterson et al., 2004; Bentz et al., 2009a,b,c).

The radius-luminosity relationship

By using the results of reverberation mapping, a relation between the BLR radius R_{BLR} and the continuum luminosity $L_{5100 \text{ \AA}}$ of the form $R_{\text{BLR}} \propto L^{1/2}$ has been established.

This relation is understandable by assuming the ionization structure and the density is same for all AGN. Such an assumption provides us a relation of $R \propto L^{1/2}$.

The radius-luminosity relation and Eq. 2.2 enable us to estimate a black hole mass from the line width of the broad H β line and the continuum luminosity at 5100 Å as following:

$$M_{\text{BH}} = 10^{6.91 \pm 0.02} \left(\frac{\lambda L_{5100 \text{ \AA}}}{10^{44} \text{ erg s}^{-1}} \right)^{0.5} \left(\frac{\text{FWHM}(\text{H}\beta)}{10^3 \text{ km s}^{-1}} \right)^2 M_{\odot} \quad (2.3)$$

(Vestergaard & Peterson, 2006). Although estimating from UV lines such as Mg II λ 2798 and C IV λ 1549 is also possible (e.g., McLure & Jarvis, 2002; Vestergaard & Peterson, 2006), it is still controversial whether the clouds emitting the C IV line are really virialized (e.g., Shemmer et al., 2004; Sulentic et al., 2007).

2.1.3 Eddington luminosity and Eddington accretion rate

An upper limit of the luminosity, which is called the Eddington luminosity, can be estimated by assuming an isotropic and stationary radiation from a black hole. By balancing the radiation pressure and the gravity, the Eddington luminosity L_{Edd} is obtained as follows:

$$\frac{\sigma_{\text{T}} L_{\text{Edd}}}{4\pi cr^2} = \frac{GMm_{\text{p}}}{r^2} \quad (2.4)$$

$$L_{\text{Edd}} = \frac{4\pi GMcm_{\text{p}}}{\sigma_{\text{T}}} \quad (2.5)$$

$$= 1.26 \times 10^{47} \left(\frac{M}{10^9 M_{\odot}} \right) \text{ erg s}^{-1}, \quad (2.6)$$

where M is the black hole mass, m_{p} is the proton mass and σ_{T} is the Thomson cross-section.

In radio quiet AGN, radiation energy is converted from a mass of accreting matters with an efficiency of η so that $L = \eta \dot{M} c^2$. The maximum efficiency η is given by the gravitational potential energy released at the last stable orbit of the black hole, which depends on spin of black hole. For non-rotating Schwarzschild black holes, the last stable orbit is $6R_{\text{g}}$ and the efficiency is estimated to be $\eta = 0.06$ (e.g., Longair, 2011). Here, $R_{\text{g}} \equiv GM/c^2 \simeq 1.5 \times 10^{14} (M/10^9 M_{\odot}) \text{ cm}$ is a so-called gravitational radius. On the other hand, for maximally rotating Kerr black holes, the last stable orbit decreases to $1R_{\text{g}}$ for corotating test particles, and the efficiency is as high as $\eta = 0.42$ (e.g., Longair, 2011). By using the efficiency for Schwarzschild black holes, a mass accretion rate required to

radiate at the Eddington luminosity is written as

$$\dot{M}_{\text{Edd}} = \frac{L_{\text{Edd}}}{\eta c^2} \quad (2.7)$$

$$= 37 \left(\frac{M}{10^9 M_{\odot}} \right) M_{\odot} \text{ yr}^{-1}. \quad (2.8)$$

This is referred to as Eddington accretion rate. The Eddington luminosity, the Eddington accretion rate and the gravitational radius are very convenient and commonly used when comparing black holes with different masses.

2.1.4 Radiation from a standard accretion disk

An accretion disk is thought to play an important role in AGN activity. In this section, we summarize physical properties and radiation of a standard accretion disk model. The standard accretion disk is optically thick so that the radiation from the disk is written as a black body radiation. From Virial theorem, the accretion disk dissipates a half of the gravitational energy as a radiation from their surface between r and $r + \Delta r$.

$$\frac{1}{2} \frac{GM\dot{M}}{r^2} \Delta r = 4\pi r \Delta r \sigma T^4, \quad (2.9)$$

where σ is the Stefan-Boltzmann constant and $4\pi r \Delta r$ is an area of the top and bottom surfaces of the disk. Thus, temperature at a radius r is calculated as

$$T(r) = \left(\frac{GM\dot{M}}{8\pi\sigma r^3} \right)^{1/4}, \quad (2.10)$$

More accurately, by including the effect of viscosity,

$$T(r) = \left[\frac{3GM\dot{M}}{8\pi\sigma r^3} \left(1 - \sqrt{\frac{r_{\text{in}}}{r}} \right) \right]^{1/4}, \quad (2.11)$$

where r_{in} is the inner radius of the accretion disk. In the limit of $r \gg r_{\text{in}}$, this is written in more convenient units:

$$kT(r) = 58 \left(\frac{M}{10^9 M_{\odot}} \right)^{-1/4} \left(\frac{\dot{M}}{\dot{M}_{\text{Edd}}} \right)^{1/4} \left(\frac{r}{R_{\text{g}}} \right)^{-3/4} \text{ eV}, \quad (2.12)$$

where k is the Boltzmann constant. Since black body radiation has a peak at an energy of $E_{\text{max}} = 2.8kT$, thermal radiation at $r = 10R_{\text{g}}$ of an accretion disk around a $M = 10^9 M_{\odot}$ black hole has a peak at ~ 30 eV, which is in UV-band. Less massive black holes such as narrow line Seyfert 1s have a spectral peak near soft-X-ray band.

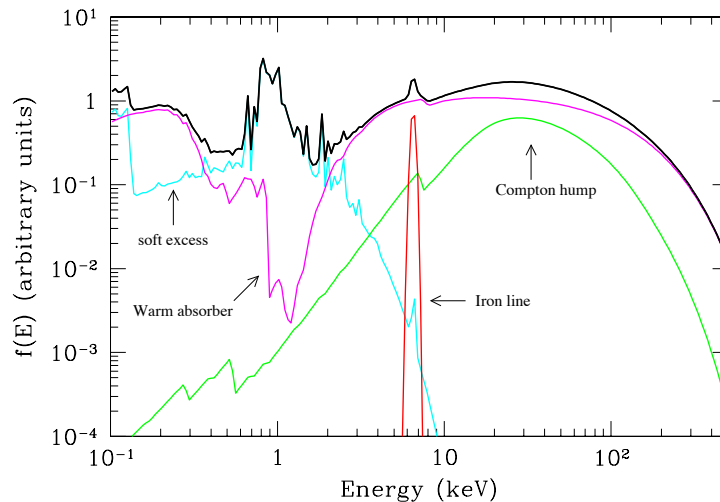


Figure 2.1: Typical X-ray spectrum of unobscured AGN (a thick black line). The primary X-ray continuum absorbed by warm absorber, soft excess, reflection hump and a Fe $K\alpha$ emission line are shown in magenta, cyan, green and red, respectively. The components are described in more detail in the text. This figure is taken from Risaliti & Elvis (2004)

2.1.5 X-ray spectrum of AGN

In X-ray band, AGN spectrum shows complex features as shown in Fig. 2.1. Detailed descriptions on these X-ray spectral features of AGN can be found in many literatures (e.g., Risaliti & Elvis, 2004; Done, 2010). In this section, we briefly review various components seen in X-ray spectrum.

Primary radiation

X-ray radiation from AGN is thought to be the disk UV photons upscattered by inverse Compton process with hot electrons near the black hole. The spectrum of the X-ray continuum is often represented by a cutoff powerlaw model as

$$N(E) = N_0 E^{-\Gamma} \exp\left(-\frac{E}{E_{\text{cut}}}\right), \quad (2.13)$$

where $N(E)$ is the differential photon number density and N_0 , Γ , E_{cut} are a normalization, photon index and cut off energy, respectively. In AGN spectra, photon index and cut off energy are typically $\Gamma \sim 1.8$ and $E_{\text{cut}} \sim 300$ keV (Dadina, 2008). The cutoff energy corresponds to the temperature of the hot electrons, but it is determined for only the most luminous AGN (e.g., Lubiński et al., 2010; Brenneman et al., 2014). Although the photon index can be arbitrary value in principle, interestingly, a correlation between

photon index and Eddington ratio is reported in some literature (Wang, Watarai & Mineshige, 2004; Shemmer et al., 2006, 2008).

Soft excess

In some AGN spectra, a broad excess below ~ 1 keV against the extrapolation of intrinsic powerlaw continuum is observed. This component is referred to as the soft excess. It is well reproduced by a disk black body emission or a thermal plasma emission with $kT \sim 0.1$ – 0.3 keV. Although a lot of explanations for the soft excess are proposed, the origin of soft excess is still controversial.

Reflection

The primary X-ray radiation is reprocessed by ionized or neutral materials. Such a reprocessed emission is called “reflection” component. The primary photons undergo two kinds of interactions, photo-electric absorption and Compton scattering. Compton scattered photons show a characteristic spectral shape peaking around 20–50 keV, which is referred to as reflection hump. This shape is created by a combination of photo-electric absorption for lower energy photons and energy loss via Compton scattering for higher energy photons.

In addition to the reflection hump, after the photo-electric absorption, fluorescence lines are emitted. The most prominent line is a Fe $K\alpha$ line at 6.4 keV because fluorescence yield is higher for higher atomic number and Fe is the last abundant element due to the nucleosynthesis (see also section 2.3).

Absorption

Absorption is also important spectral feature. At least half of local AGN shows absorbed spectra below ~ 2 keV, which is called “warm absorber” (Blustin et al., 2005; Piconcelli et al., 2005; McKernan, Yaqoob & Reynolds, 2007). The detailed properties of warm absorbers are described in section 2.2.

2.2 Observations of AGN outflows

2.2.1 Importance of the AGN winds

Coevolution of SMBHs and their host galaxies is one of the most important problems in modern astrophysics. The widely accepted evidence for the coevolution is the so-called M - σ relation as shown in Fig. 2.2, which is the relation between black hole mass M and

and have established the existence energy transportation from the black hole to \sim Mpc scale structures.

The AGN winds as a main interaction in the quasar mode feedback are naturally expected to exist in high accretion rate AGN (e.g., King & Pounds, 2003; Proga & Kallman, 2004), but there are few observational evidence. Most of the winds observed in AGN are the less powerful winds called “warm absorbers”, which have a moderate velocity of hundreds to few thousand km s^{-1} (Blustin et al., 2005; Piconcelli et al., 2005; McKernan, Yaqoob & Reynolds, 2007). Theoretically, the winds with the momenta close to the Eddington limit is required to reproduce the M - σ relation (Silk & Rees, 1998; King, 2003, 2010), so that such less powerful winds are not sufficient for the quasar mode feedback.

Recently, the most powerful kinds of winds called ultrafast outflows (UFOs), which is the subject of this thesis, are discovered. They are characterized by their extremely fast velocity (typically $\gtrsim 0.1c$), which strongly indicates that a huge amount of kinetic energy is transported to the host galaxy. This makes the UFOs to be a most promising candidate for the quasar mode feedback process.

2.2.2 BAL and warm absorbers

Before discovery of the ultrafast outflows, the presence of two kinds of outflows was known. One is observed in UV or optical spectra and the other is in soft X-ray spectra. The former is divided into three subclasses, depending on their line width: the broad absorption line (BAL; $\text{FWHM} > 2000 \text{ km s}^{-1}$), the mini broad absorption line (mini-BAL; $500 \text{ km s}^{-1} < \text{FWHM} < 2000 \text{ km s}^{-1}$) and the narrow absorption line (NAL; $\text{FWHM} < 500 \text{ km s}^{-1}$). These absorption features are strongly blue-shifted with a few 10^2 km s^{-1} up to several 10^4 km s^{-1} (Misawa et al., 2007; Gibson et al., 2009). BALs including mini-BALs and NALs are observed in ~ 10 – 30% of radio-quiet quasars (Weymann et al., 1991; Hamann, Korista & Morris, 1993; Hewett & Foltz, 2003; Ganguly & Brotherton, 2008; Allen et al., 2011). These absorption features are seen in moderately ionized ions such as C IV, N V and Si IV, where the cross-section of bound-bound transitions is high. Therefore, these winds are thought to be driven by the UV-line radiation pressure (see section 2.2.4).

The other one is the warm absorber as already mentioned, which is observed half of AGN (Blustin et al., 2005; Piconcelli et al., 2005; McKernan, Yaqoob & Reynolds, 2007). Warm absorber is a lower velocity (up to $\sim 2000 \text{ km s}^{-1}$) system compared with BAL. Its column density and ionization parameter are typically between $N_{\text{H}} \sim 10^{20}$ – 10^{22} cm^{-2} and $\xi \sim 10^0$ – $10^3 \text{ erg s}^{-1} \text{ cm}$, respectively. Here, ionization parameter ξ is

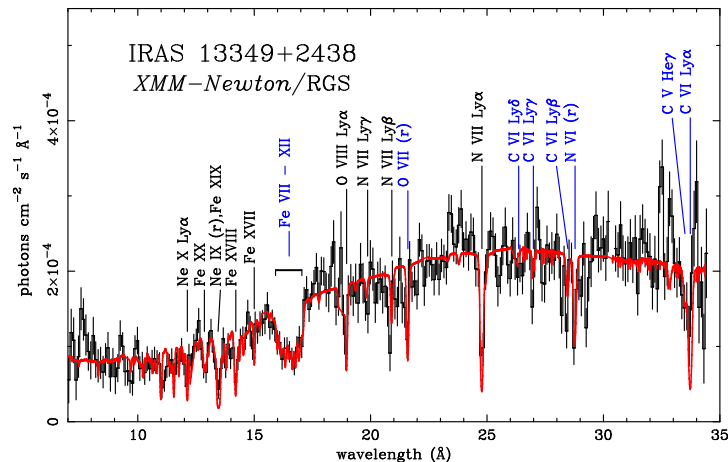


Figure 2.3: Spectrum of warm absorber in IRAS 13349+2438 observed by *XMM-Newton*/RGS. Absorption lines labeled in blue are lowly ionized component ($\xi \sim 1-2$), while lines labeled in black are highly ionized component ($\xi \sim 2.0-2.5$). Low- ξ lines are blue shifted with $v \sim 400 \text{ km s}^{-1}$. This figure is taken from Sako et al. (2001).

defined by $\xi \equiv L/nR^2$ (see section 2.3). Therefore, warm absorber is observed as O VII–VIII, Ne IX–X, Mg XI–XII, Si XIII–XIV and Fe XVII–XXIV lines as shown in Fig. 2.3. According to Blustin et al. (2005), location of its emission region is estimated to be comparable with dusty torus for most of their samples. This result strongly indicates that warm absorber is thermally driven.

2.2.3 Ultra-fast outflows

In X-ray bands, blue shifted absorption lines with an extremely high velocity similar to BALs are discovered in individual sources (e.g., Chartas et al., 2002; Reeves, O’Brien & Ward, 2003; Pounds et al., 2003a,b), including the sources analyzed in this thesis (APM 08279+5255 and PDS 456). Tombesi et al. (2010) first reported the presence of such blue shifted absorption lines in $\sim 30-40\%$ of radio quiet AGN in local Universe by using archival data of *XMM-Newton*. Gofford et al. (2013) confirmed the existence of these absorption lines with independent samples from archival data of *Suzaku*, where UFOs are detected in $\sim 20-30\%$ of samples. Such fast outflows are referred to as “ultra-fast outflows (UFOs)”. According to Tombesi et al. (2010), UFOs are defined as highly ionized absorbers showing Fe XXV He α and Fe XXVI Ly α absorption lines blue shifted with a velocity of $v > 10^4 \text{ km s}^{-1}$ ($\simeq 0.033c$).

Systematic studies performed by Tombesi et al. (2010) and Gofford et al. (2013) revealed the typical properties of UFOs as shown in Fig. 2.4. The mean blue shift velocity of UFOs is $v_{\text{out}} \sim 10^{4.5} \text{ km s}^{-1} \simeq 0.1c$, which is faster than BALs. The mean

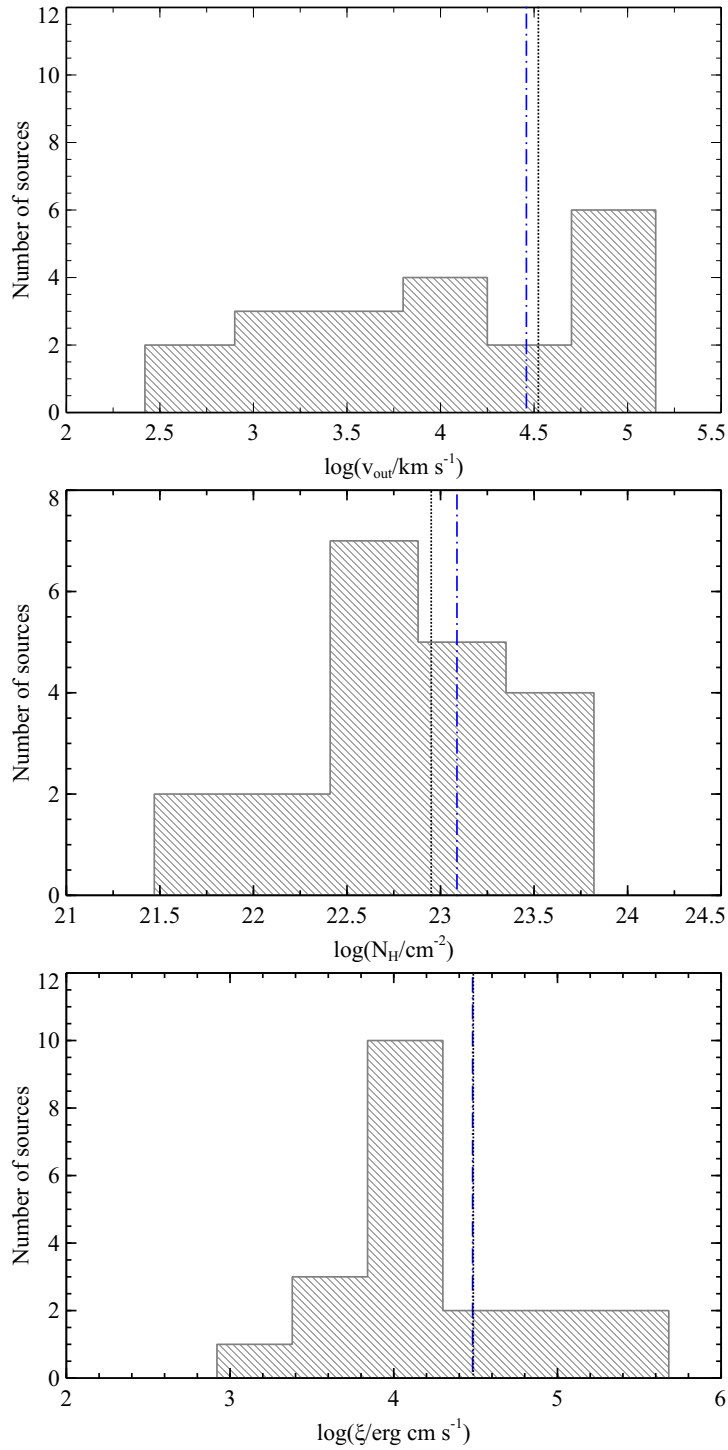


Figure 2.4: The distributions of the column density N_{H} , the outflow velocity v_{out} and the ionization parameter ξ in UFOs. Blue and black vertical lines indicate the mean values of *XMM-Newton* and *Suzaku* analyses respectively. This figure is taken from Gofford et al. (2013).

column density and ionization parameters lie in $N_{\text{H}} \sim 10^{23} \text{ cm}^{-2}$ and $\log \xi \sim 4.5$, where the ionization parameters are defined by $\xi \equiv L/nR^2$ (see also section 2.3). By using these values obtained directly from the spectral fitting, Tombesi et al. (2010) estimated the location of the UFO. On the assumption of compact absorber ($\Delta R/R < 1$), the upper limit of the location of UFO is estimated as $R < L/N_{\text{H}}\xi \sim 10^{16} \text{ cm}$ ($\simeq 10^4 R_g$), which is comparable with the location of BLR. Thus UFOs are thought to be launched from innermost regions of AGN.

However, the driving mechanisms of UFOs are still unknown due to both of the poor sensitivity of current instruments and the lack of the spectral models considering the realistic structure of the winds. In the next section, we summarize the possible wind driving mechanisms.

2.2.4 Wind driving mechanisms

The accretion disk winds are accelerated by the pressure gradient force, the radiation force and the magnetic force. When at least one of these forces exceeds the gravitational force of the black hole, the wind is launched. This can be understood from the equation of motion (Proga, 2007; Reynolds, 2012)

$$\rho \frac{D\mathbf{v}}{Dt} + \rho \nabla \Phi = -\nabla p + \mathbf{F}_{\text{rad}} + \frac{1}{4\pi} (\nabla \times \mathbf{B}) \times \mathbf{B}, \quad (2.14)$$

where ρ , \mathbf{v} and p are the mass density, the velocity and the pressure of the gas in the wind, respectively. D/Dt is the convective derivative or the Lagrangian derivative. The term Φ , \mathbf{B} and \mathbf{F}_{rad} are the gravitational potential, magnetic field and the total radiation force, respectively.

Each force term in the right hand side of Eq. 2.14 corresponds to the possible wind driving mechanisms: (1) the thermal driving, (2) the radiative driving and (3) the magnetic driving mechanisms. This section is devoted to the description of these three wind driving mechanisms.

Thermal driving

If the strong radiation heats the gas on the surface of the accretion disk and its thermal pressure gradient exceeds the gravitational force, the wind is launched. In other words, the wind is launched when the thermal velocity is larger than the escape velocity $v_{\text{esc}} = \sqrt{2GM_{\text{BH}}/r}$, where G , M_{BH} and r are the gravitational constant, black hole mass and the radius from the center of gravity (Begelman, McKee & Shields, 1983). This mechanism is called ‘‘thermal driving mechanism’’.

The maximum velocity of the wind launched by the thermal driving can be estimated by considering “Compton temperature”. Compton temperature is the equilibrium temperature, where heating of the electrons by Compton scattering and cooling by inverse Compton scattering are balanced. By the radiation from the inner and hotter part of the disk, the outer and cooler part of the disk can be heated up to the Compton temperature of $\sim 10^7\text{--}10^8$ K, which corresponds to the launching radius of $\gtrsim 10^4 R_g$ and the outflow velocity of $v_{\text{esc}} \lesssim 4000$ km s $^{-1}$. Therefore, this mechanism is thought to be responsible to the observed warm absorbers, but it cannot accelerate faster winds like UFOs.

Radiation pressure driving

The second term \mathbf{F}_{rad} in Eq. 2.14 is the radiation force due to the gradient of radiation pressure. If the source approaches the Eddington luminosity, continuum radiation pressure launches the outflow. Even if the luminosity is below Eddington, the radiation pressure can contribute to launching the wind. Since the radiation pressure decreases the effective gravity by a factor of $1 - L/L_{\text{Edd}}$, the thermal driving can launch the wind from smaller radius.

The wind can be launched more efficiently if bound-bound transitions of partially ionized ions in UV band are the dominant interaction between photons and matters. It is because cross-section of these interactions gets larger than the Thomson cross-section by a factor of 2000–4000 if the materials are moderately ionized (Castor, Abbott & Klein, 1975). This is often referred to as UV-line driving. The UV-line driven wind is launched at a radius where the local disk radiation is in the UV band. For black holes with highest masses $\sim 10^9 M_\odot$, the winds are launched from the inner part of the disk (see sec. 2.1.4), where the escape velocity is high. This mechanism can potentially accelerate the wind up to a few tens of percents of the speed of light (Risaliti & Elvis, 2010).

Magnetic driving

The last term of Eq. 2.14 is the Lorentz force, which corresponds to the magnetic driving. Since it strongly depends on the unknown magnetic field configuration, it is difficult to constrain its physical properties. However, a lot of simulations for magnetic driven winds have been performed by assuming the self-similarity, where all the physical parameters of the wind have power-law radial dependence (e.g., Fukumura et al., 2010). According to this model, He-like Fe ions can be accelerated up to $v \simeq 0.6c$ at a radius of 10–80 R_g .

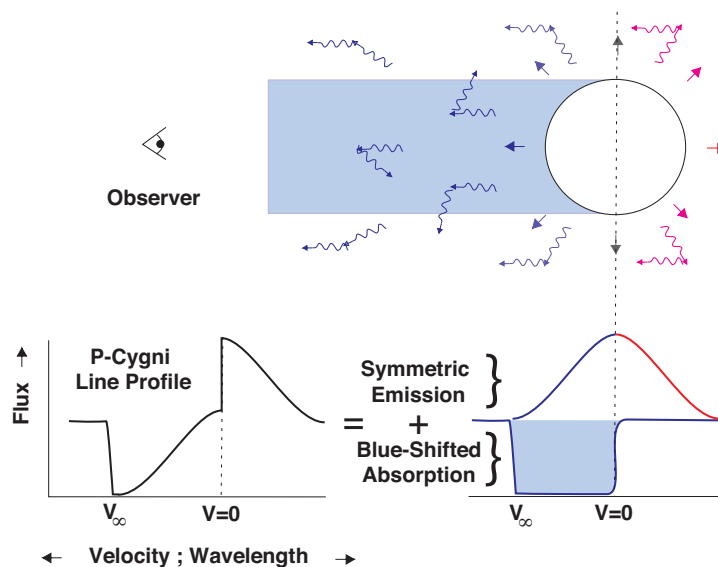


Figure 2.5: A schematic view of the formation of P-Cygni profile. This figure is taken from Owocki (2000).

2.2.5 P-Cygni profiles as a probe of the wind

The wind is often observed as a characteristic spectral feature called “P-Cygni profile”, which consists of a red wing of the emission line and a blue shifted absorption line. It is named after a star P-Cygni, which is first recognized to show such a spectral feature. The P-Cygni profile is formed as shown in Fig. 2.5. Radiation from a star surrounded by a spherically outflowing wind is observed to be accompanied by emission lines and absorption lines. The absorption lines are created by only the materials located between the star and the observer. Since all such materials are approaching to the observer, the absorption lines are blue shifted by the Doppler effect. On the other hand, the emission lines come from both approaching and receding materials so that the emission lines are observed as symmetrically broadened lines. By combining such emission and absorption lines, the P-Cygni profile with emission at higher energy and absorption at lower energy are formed.

The P-Cygni profile can be analytically calculated by treating the radiation transfer with Sobolev approximation. In this approximation, a rapidly accelerating and spherically symmetric wind is assumed. As shown in Fig. 2.6, a photon with an energy slightly smaller than a line (bound-bound) transition energy propagates freely until it is red-shifted by the wind velocity to match the transition energy. Usually, a cross-section of a bound-bound transition is non-zero within a Doppler width of the ion thermal velocity $v_{\text{th}} \equiv \sqrt{2kT/m_a}$ (see also section 2.3), corresponding to a geometric width called a

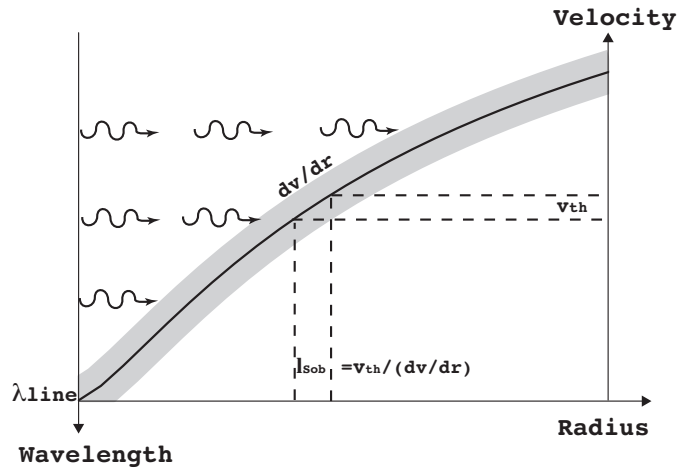


Figure 2.6: A schematic view of Sobolev approximation. A photon with an energy slightly smaller than a line (bound-bound) transition energy does not interact with the wind until the redshifted photon energy in the rest frame of the wind matches the transition energy. In a rapidly accelerating wind, such a photon is absorbed at a local point within a Sobolev length l_{Sob} . This figure is taken from Owocki (2004).

Sobolev length $l_{\text{Sob}} = v_{\text{th}}/(dv/dr)$. For a rapidly accelerating wind, the Sobolev length is very small, so that the key parameters of the wind such as the optical depth and the line force can be treated as a function of local physical parameters.

Although the force for a single line transition can be easily calculated by the Sobolev approximation, the UV-line driven wind requires us to consider contributions from a large number ($\gtrsim 10^5$) of line transitions. In a well-established UV-line driven wind model called CAK model (Castor, Abbott & Klein, 1975), the line force is treated by one parameter called a force multiplier $M(t)$, which is a sum of all the line forces normalized by the radiation force due to Thomson scattering. Here, $t \equiv \sigma_{\text{T}} n l_{\text{Sob}}$ is a local optical depth parameter, and σ_{T} and n are the Thomson cross-section and the gas density. In the CAK model, by approximating the force multiplier as a power law $M(t) = Kt^{-\alpha}$ ($\alpha \sim 0.6$; Stevens & Kallman, 1990), a velocity structure in the wind is written as the so-called CAK velocity law

$$v(r) = v_{\infty} \left(1 - \frac{R_*}{r} \right)^{\beta}, \quad (2.15)$$

where R_* is the radius of the star, $v_{\infty} = v_{\text{esc}} \sqrt{\alpha/(1-\alpha)} \sim v_{\text{esc}}$ is the terminal velocity and $\beta = 1/2$ depends on the acceleration of the wind. The CAK velocity law is widely used for modeling the wind.

In principle, the analysis of the P-Cygni profile can probe the velocity structure in the

wind as well as the terminal velocity. Indeed, in the case of stellar winds, the parameter β is constrained at a little larger value ~ 0.8 (e.g., Pauldrach, Puls & Kudritzki, 1986; Blomme, 1990).

2.3 Radiation Processes

When X-ray photons travel through the AGN wind, the photons interact with the photoionized plasma in the wind, and their spectral energy distribution is distorted. Therefore, understanding the physical processes in the photoionized plasma is essential for the X-ray spectroscopic study of the AGN wind. In this section, we summarize the basic physical processes in the photoionized plasma.

2.3.1 Photoionized plasma

A gas illuminated by strong X-ray or UV photons from bright astrophysical objects such as AGN is ionized via photoionization processes and forms a photoionized plasma. Most of gases or plasmas around AGN such as BLR/NLR clouds and AGN winds are generally accepted as photoionized plasmas because of strong UV/X-ray radiations from AGN.

In photoionized plasmas, the charge state distribution is determined by photoionization equilibrium, where photoionization rate and recombination rate are balanced. Both photoionization and recombination rates depend on the electron temperature via level populations and Milne relation (Eq. 2.20), and the electron temperature is determined by the thermal balance of heating and cooling. However, electron heating and cooling are related to the emission and absorption processes, which depend on the charge state distribution. Therefore, photoionization and thermal balances are strongly coupled, and iterative treatments are essential to determine the ionization structure and electron temperature.

By implementing such an iterative treatment, a computer program XSTAR (Kallman et al., 2004) can self-consistently calculate the ionization states, electron temperature and the radiation spectra in 1-dimensional photoionized plasma. In this program, all the physical processes described in this section are implemented. Although this program can solve only 1-dimensional problems, this is widely used for the spectral analysis of the photoionized plasma such as AGN winds.

Ionization states and electron temperature strongly depend on the ionization parameter (Tarter, Tucker & Salpeter, 1969)

$$\xi = \frac{L}{nR^2}, \quad (2.16)$$

where L is the luminosity of the ionizing radiation, n is the electron number density and R is the distance from the source. Although ionization structures also depend on the other properties such as the spectral shape and the geometrical structure, this parameter is widely used as a good indicator of the ionization structure.

2.3.2 Photon interactions with photoionized plasma

In photoionized plasma, photoionization, photoexcitation, Compton scattering and their inverse processes play important roles. Photoionization and radiative recombination determine the continuum spectral shape including edge structure, while photoexcitation and radiative decay are responsible for the absorption and emission lines. Compton scattering forms re-emitted continuum spectra, adding a characteristic Compton hump feature on the high energy spectra above ~ 10 keV.

In this section, we summarize the interactions between photons and ions or atoms in the photoionized plasma. More detailed descriptions of the radiation processes are given in many textbooks (e.g., Spitzer, 1978; Osterbrock & Ferland, 2006; Rybicki & Lightman, 2008; Draine, 2010; Longair, 2011).

Photoionization and Radiative recombination

Photoionization is a bound-free transition from an initial state composed of a photon γ and an ion X^{+r} to a final state composed of a free electron e^- and an ionized ion X^{+r+1} losing one more electron. An inverse process of this is radiative recombination. These two processes are written as

$$X^{+r} + \gamma \leftrightarrow X^{+r+1} + e^-. \quad (2.17)$$

The photoionization cross-section of Hydrogen-like ions for a photon energy $E \geq Z^2 I_{\text{H}}$ is given by

$$\sigma_{\text{pi}}(E) = \sigma_0 \left(\frac{Z^2 I_{\text{H}}}{E} \right)^4 \frac{\exp(4 - 4 \arctan(x)/x)}{1 - \exp(-2\pi/x)}, \quad (2.18)$$

where $x \equiv \sqrt{E/Z^2 I_{\text{H}} - 1}$, Z is the atomic number and $I_{\text{H}} \simeq 13.6$ eV is the ionization potential of a Hydrogen atom. σ_0 is the cross-section at threshold energy ($= Z^2 I_{\text{H}}$), which is given by

$$\sigma_0 \equiv \frac{2^9 \pi^2}{3 \exp(4)} Z^{-2} \alpha a_0^2, \quad (2.19)$$

where α is fine-structure constant and a_0 is Bohr radius. In the case that the photon energy is close to the threshold ($E \lesssim 100 Z^2 I_{\text{H}}$), the cross-section is approximated as

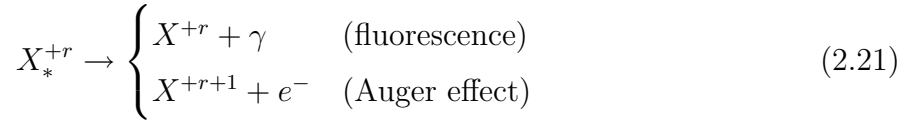
$\sigma_{\text{pe}}(E) \simeq \sigma_0(Z^2 I_{\text{H}}/E)^3 \propto Z^4$. As seen in this equation, the photoionization cross-section has strong dependence on the atomic number Z . Therefore, heavy elements such as Fe contributes greatly in spite of their much lower abundances. The cross-sections for ions with multiple electrons are more complicated but are given as analytic fits.

The cross-section of radiative recombination is related to the photoionization cross-section by applying a principle of detailed balance in thermodynamic equilibrium. The relation sometimes referred to as Milne relation is written as

$$\sigma_{\text{rr}}(v) = \frac{g_r}{g_{r+1}} \left(\frac{E}{m_e c v} \right)^2 \sigma_{\text{pi}}(E), \quad (2.20)$$

where g_r is the statistical weight of the ion X^{+r} , whereas g_{r+1} is the statistical weight of the ion $X^{+(r+1)}$. A photon energy E and an electron velocity v are related as $E = m_e v^2/2 + I$, where I is the ionization potential.

In the case of an ion with three or more electron, photoionization process leaves an ion in a highly excited state with an inner shell vacancy. It undergoes either of the fluorescence and the Auger effect as described below:



In fluorescence process, the excited state is relaxed via radiative decay, emitting a X-ray photon. Instead, in the Auger effect, one electron drops into the vacancy, and the other electron(s) is ejected from the ion. The probability of fluorescence processes in competition with the Auger effect is called fluorescence yields. These yields for the K, L and M shells for the elements with various atomic numbers are plotted in Fig. 2.7. As shown, fluorescence is dominant for elements with larger atomic number.

Photoexcitation

Photoexcitation is a bound-bound transition from a lower energy level l to an upper energy level u . This process occurs when an ion in a level l absorbs a photon having an energy equal to $E_u - E_l$, where E_l and E_u are the energies of lower (l) and upper (u) levels.



As a result of this process, an absorption line at $E_u - E_l$ is observed in the spectrum. After the photoexcitation process, the excited ion relaxes into the ground state, releasing the absorbed energy as a photon or an electron. The former process is called radiative decay,

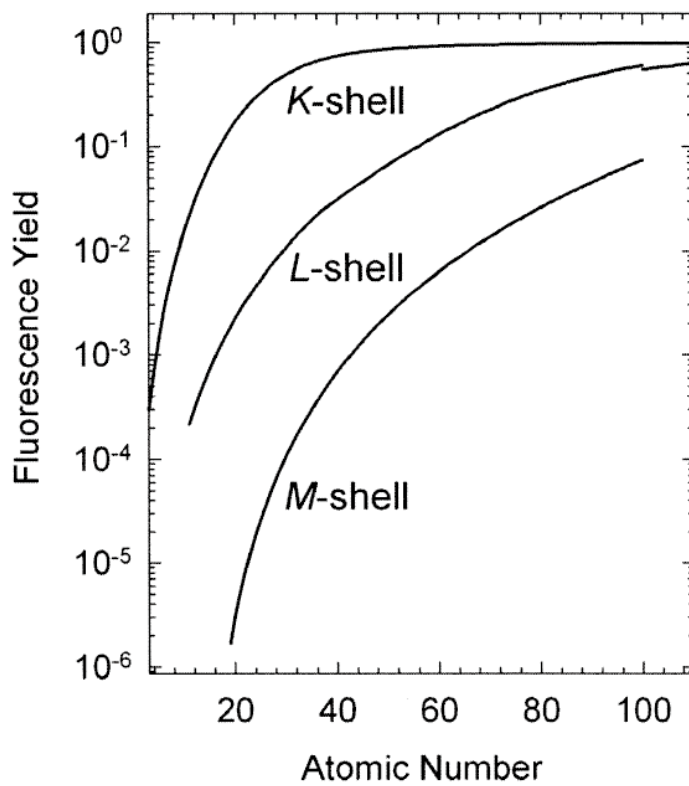


Figure 2.7: Fluorescence yields for K, L, and M shells for $3 \leq Z \leq 110$. The plotted curves for the L and M shells represent average subshell effective yields. This figure is taken from Thompson et al. (2009).

and the latter is called autoionization. Just like the Auger effect, autoionization process can occur only if the ion has multiple electrons. The radiative decay process forms an emission line with the same energy as the absorbed photon. These emission and absorption lines are very important to probe physical properties of the emitting/absorbing matter such as the dynamics, temperature, density and abundances of the material.

The cross-section of photoexcitation between a lower energy level l to an upper level u is proportional to the oscillator strength f_{lu} as a following equation.

$$\sigma_{lu}(\nu) = \frac{\pi e^2}{m_e c} f_{lu} \phi(\nu), \quad (2.23)$$

where $\phi(\nu)$ is the normalized line profile with $\int \phi(\nu) d\nu = 1$. The line profile $\phi(\nu)$ is generally written as a combination of a Gaussian profile and a Lorentzian profile:

$$\phi(\nu) = \frac{1}{\Delta\nu_D \pi^{1/2}} H(a, u), \quad (2.24)$$

where $H(a, u)$ is the Voigt function

$$H(a, u) = \frac{a}{\pi} \int_{-\infty}^{\infty} \frac{\exp(-y^2) dy}{a^2 + (u - y)^2}, \quad (2.25)$$

and a , u and $\Delta\nu_D$ are written as

$$a = \frac{\Gamma}{4\pi\Delta\nu_D} \quad (2.26)$$

$$u = \frac{\nu - \nu_0}{\Delta\nu_D}. \quad (2.27)$$

The Doppler width $\Delta\nu_D$ is defined by

$$\Delta\nu_D = \nu_0 \sqrt{\frac{2kT}{m_a c^2}}, \quad (2.28)$$

which is $\sqrt{2}$ times larger than the standard deviation of the Gaussian profile representing Doppler broadening due to thermal motion with temperature T . Here, m_a is the mass of an atom or an ion. The effect of the turbulence can also be treated as the thermal motion. Γ characterize an effect of natural broadening based on the uncertainty principle, where a large uncertainty of a transition energy is required by a short life time of the corresponding excited state. Thus, Γ is related to a radiative decay rate as

$$\Gamma = \sum_l A_{ul}, \quad (2.29)$$

where A_{ul} is a transition probability per unit time for spontaneous emission (so called the Einstein A-coefficient) from an upper level u to a lower level l and the sum is over all l .

Energy levels for ions are designated by spectroscopic notation. If total orbital angular momentum is L , total spin angular momentum is S and total angular momentum is J , the energy levels are expressed as

$${}^{2S+1}\mathcal{L}_J, \quad (2.30)$$

where $\mathcal{L} = S, P, D, F$ for $L = 0, 1, 2, 3$. Parity of electronic wave function is also important variable. The parity is even if $\prod_i (-1)^{l_i} = 1$, and odd if $\prod_i (-1)^{l_i} = -1$, where l_i is the orbital angular momentum of individual electron orbitals.

The most prominent transitions of H-like ions are Lyman series:

- Ly $\alpha_{1,2}$: $2p \ ^2P_{3/2,1/2} \leftrightarrow 1s \ ^2S_{1/2}$
- Ly $\beta_{1,2}$: $3p \ ^2P_{3/2,1/2} \leftrightarrow 1s \ ^2S_{1/2}$
- Ly $\gamma_{1,2}$: $4p \ ^2P_{3/2,1/2} \leftrightarrow 1s \ ^2S_{1/2}$

These transitions are electric dipole transitions, which satisfies the following selection rules: 1) parity must change, 2) $\Delta L = 0, \pm 1$, 3) $\Delta J = 0, \pm 1$ (except $J = 0 \leftrightarrow 0$), 4) $\Delta l = \pm 1$ and 5) $\Delta S = 0$. The transition satisfying above selection rules is often referred to as an allowed transition.

He-like ions show more complicated transitions than H-like ions as follows:

- w : $1s2p \ ^1P_1 \leftrightarrow 1s^2 \ ^1S_0$
- x : $1s2p \ ^3P_2 \leftrightarrow 1s^2 \ ^1S_0$
- y : $1s2p \ ^3P_1 \leftrightarrow 1s^2 \ ^1S_0$
- z : $1s2s \ ^3S_1 \leftrightarrow 1s^2 \ ^1S_0$

Here, w is the electronic dipole transition, and is also called resonance transition. x and y are referred to as inter combination transitions or semi-forbidden transitions, where the electric dipole selection rules 1 to 4 are satisfied but $\Delta S \neq 0$. These transitions are much weaker than allowed transitions. z is a magnetic dipole transition, where the electric dipole selection rules 1, 4 and 5 are not satisfied (parity is unchanged, $\Delta l = 0$ and $\Delta S \neq 0$). This transition is called forbidden transition. The resonance, inter combination and forbidden transitions are often designated by symbols of r , i and f , respectively. All transitions of He-like ions shown above are only transitions between K-shell and L-shell ($n = 2 \leftrightarrow 1$), which is often called He α . In the same way as Lyman series, transitions of $n = 3 \leftrightarrow 1$ and $n = 4 \leftrightarrow 1$ are called He β and He γ , respectively.

Compton scattering

Compton scattering is an energy exchange process between photons and electrons. The energy of a photon scattered by an electron at rest is calculated by requiring conservation of momentum and energy

$$E_1 = \frac{E_0}{1 + \frac{E_0}{m_e c^2} (1 - \cos \theta)}, \quad (2.31)$$

where E_0 and E_1 are the incident and scattered photon energy and θ is a scattering angle. For low energy photons with $E_0 \ll m_e c^2$, Compton scattering approaches an elastic scattering, which is Thomson scattering.

The differential cross-section of Compton scattering for unpolarized photons is given by the Klein-Nishina formula

$$\frac{d\sigma}{d\Omega} = \frac{r_0^2}{2} \frac{E_1^2}{E_0^2} \left(\frac{E_0}{E_1} + \frac{E_1}{E_0} - \sin^2 \theta \right), \quad (2.32)$$

where $r_0 = e^2/m_e c^2$ is the classical electron radius. The total cross-section is given by

$$\sigma = \sigma_T \frac{3}{4} \left[\frac{1+x}{x^3} \left\{ \frac{2x(1+x)}{1+2x} - \ln(1+2x) \right\} + \frac{1}{2x} \ln(1+2x) - \frac{1+3x}{(1+2x)^2} \right], \quad (2.33)$$

where $x \equiv E_0/m_e c^2$ and $\sigma_T = 8\pi r_0^2/3$ is the Thomson cross-section. For low energy photons ($x \ll 0$), this cross-section approaches to σ_T .

In the case of a scattering by a moving electron, energy is transferred from the electron to the photon. This is the inverse process of Compton scattering, which is called Inverse Compton scattering. By applying the Lorentz transformation, the incident energy in the electron rest frame is written as

$$E'_0 = E_0 \gamma (1 - \beta \cos \theta), \quad (2.34)$$

where $\gamma = (1 - \beta^2)^{-1/2}$, $\beta = v/c$ and v is the electron velocity. A prime indicates the electron rest frame and θ is an incident angle. If the incident photon energy is small ($E_0 \ll m_e c^2$), the cross-section is equals to Thomson cross-section σ_T . Thus, the scattered photon has the same energy as the incident photon in the electron rest frame, namely E'_0 . By applying the Lorentz transformation to the observer's frame, we obtain

$$E_1 = E'_0 \gamma (1 - \beta \cos \phi), \quad (2.35)$$

where ϕ is the scattered angle. By averaging the incident and scattered angle, the scattered photon energy in the observer's frame is written as $E_1 \simeq \gamma^2 E_0$.

Chapter 3

Instrumentation

In this thesis, we use the X-ray archival data of UFOs observed by *Suzaku* and *XMM-Newton*. This chapter describes basic properties of instruments onboard *Suzaku* and *XMM-Newton*.

3.1 The *Suzaku* Observatory

Suzaku (Mitsuda et al., 2007) is the fifth Japanese X-ray astrophysical observatory launched on 2005 July 10. *Suzaku* is placed in a near circular orbit with an orbital period of ~ 96 minutes, altitude of 570 km and an inclination of 31° . *Suzaku* has two types of X-ray instruments in operation, the X-ray Imaging Spectrometers (XISs) and the Hard X-ray Detector (HXD). The XISs are the X-ray sensitive imaging charge coupled device (CCD) cameras, while the HXD is the non-imaging, collimated detector. The XISs cover an energy range up to 12 keV, and the HXD covers much higher energies with 10–600 keV. The X-Ray Spectrometer (XRS) is no longer operational due to the liquid helium coolant venting to space.

Fig. 3.1 shows a schematic view and side view of *Suzaku*. Five sets of the X-Ray Telescope (XRT) are loaded on *Suzaku*, and four XISs and the XRS are located in the focal plane of the XRTs. The HXD is mounted on the base panel, where the XISs are also mounted, but it does not have corresponding XRTs. All these instruments operate simultaneously.

In the following subsections, we describe only the XRTs and XISs, and do not describe the HXD because we do not use the results of the HXD in this thesis.

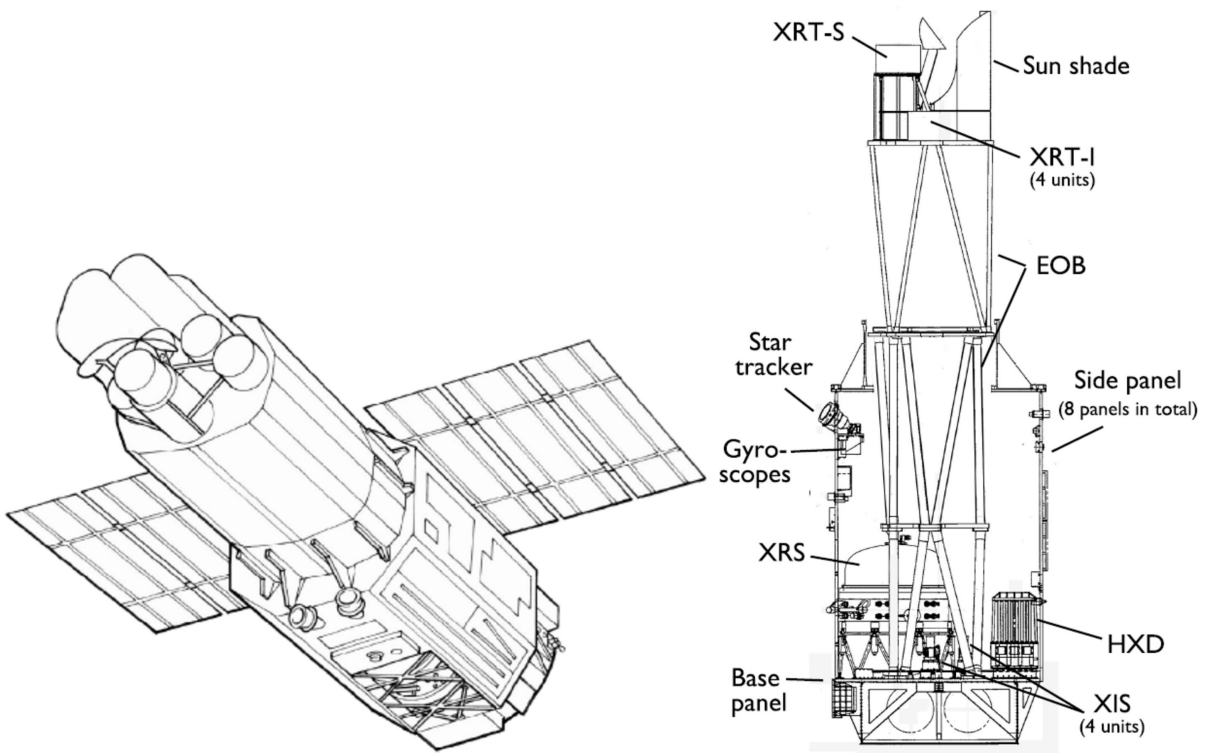


Figure 3.1: Schematic view (left) and side view (right) of *Suzaku* taken from Mitsuda et al. (2007)

Table 3.1: Specifications of the XRTs. Values are taken from the *Suzaku* Technical Description.

Parameter	Value
Focal length	4.75 m
Number of modules	4
Weight/telescope	19.3 kg
Field of view	17' at 1.5 keV 13' at 8 keV
Effective area per XRT	440 cm ² at 1.5 keV 250 cm ² at 8 keV
Spatial resolution (HPD)	2.'0

3.1.1 X-ray Telescope (XRT)

The XRTs (Serlemitsos et al., 2007) are thin-foil-nested Wolter-I type telescopes, developed by NASA/GSFC, Nagoya University, Tokyo Metropolitan University and ISAS/JAXA. These are composed of compactly nested thin conical reflectors, forming ultimate grazing-incidence geometries. In *Suzaku*, by using very thin ($\sim 178 \mu\text{m}$) foils, light-weight and large correction efficiency up to ~ 12 keV are achieved.

The basic properties of XRTs are summarized in Tab. 3.1. The half power diameter (HPD) of the XRTs are typically $\sim 2'$, and ranging from $1'.8$ to $2'.3$. The effective area of the XRTs is 440 cm^2 at 1.5 keV and 250 cm^2 at 7 keV. As shown in Fig. 3.2, the effective area of four XRTs is much better than *Chandra*, and comparable to *XMM-Newton* in the Fe K band (~ 7 keV).

3.1.2 X-ray Imaging Spectrometer (XIS)

The XISs (Koyama et al., 2007) consist of four sensors designated as XIS 0, 1, 2 and 3, and each sensor has one CCD chip. The CCDs of the XISs are MOS-type three-phase CCDs operated in a photon counting mode. Each CCD chip is divided into 1024×1024 pixels, covering a $18' \times 18'$ region on the sky. The pixel size is $24 \mu\text{m}$ square, and the size of a single CCD is $25 \text{ mm} \times 25 \text{ mm}$. The XIS 0, 2 and 3 employ front-illuminated (FI) chips, while the XIS 1 has a back-illuminated (BI) chip. However, in 2006 November, the XIS 2 suffered an impact of micro-meteoroid and lost its entire imaging area. Thus, currently, only the XIS 0, 1, 3 are in operation. In this thesis, all the XISs are available for the data of 1H 0707-495, while only XIS 0, 1, 3 are available for the data of PDS 456.

The basic properties of the XISs are summarized in Tab. 3.2. The FI chips are less

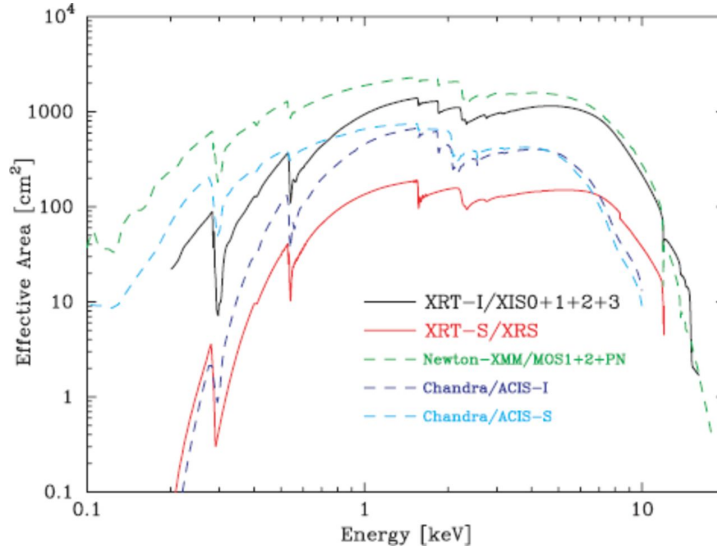


Figure 3.2: Effective area of XRT taken from Serlemitsos et al. (2007).

Table 3.2: Specifications of the XISs. Values are taken from the *Suzaku* Technical Description.

Parameter	Value
Field of view	$17.8' \times 17.8'$
Energy range	0.2–12 keV
Format	1024×1024 pixels
Pixel size	$24 \mu\text{m} \times 24 \mu\text{m}$
Energy resolution	~ 130 eV (FWHM) at 6 keV
Effective area	340 cm^2 (FI), 390 cm^2 (BI) at 1.5 keV 150 cm^2 (FI), 100 cm^2 (BI) at 8.0 keV
Readout noise	~ 2.5 electrons (RMS)
Time resolution	8 s (normal), 7.8 ms (P-sum)

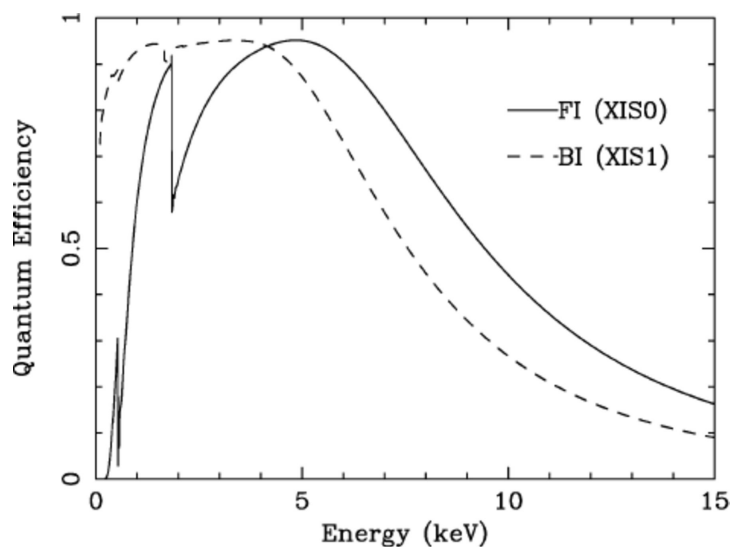


Figure 3.3: Quantum efficiency of XIS taken from Koyama et al. (2007).

sensitive than the BI chip at lower energies because soft X-ray photons are absorbed by a gate structure on the front side of the chip. On the other hand, at higher energies above ~ 4 keV, the FI chips have large effective area. This is because the BI chip has a thinner depletion layer of $\sim 42 \mu\text{m}$ than the FI chips. These properties are shown in Fig. 3.3, where the quantum efficiency for the FI and BI are plotted as a function of energy.

One of the strong points of the XIS compared with the other CCD instruments is the good energy resolution. As shown in Fig. 3.4, the energy resolution of the XIS at 5.9 keV is ~ 130 eV (FWHM; full width at half maximum), which is better than the other CCD instruments such as the EPIC of *XMM-Newton*. Therefore, the FI detector is most sensitive to the blue shifted narrow Fe K absorption lines due to its good energy resolution and large effective area above ~ 7 keV.

Also, the low and stable instrumental background is an advantage of the XIS (Mitsuda et al., 2007). This is because a combination of the low Earth orbit of *Suzaku* satellite and the instrumental design of the XIS. Fig. 3.5 shows the XIS background count rate compared with the *ASCA*, *Chandra* and *XMM-Newton*. As shown, the XIS background is lowest among the instruments in operation, and comparable to *ASCA*, which had the lowest background. This very low background contributes to a high sensitivity for spatially extended sources.

3.2 The *XMM-Newton* Observatory

XMM-Newton (Jansen et al., 2001) is a cornerstone mission of the European Space

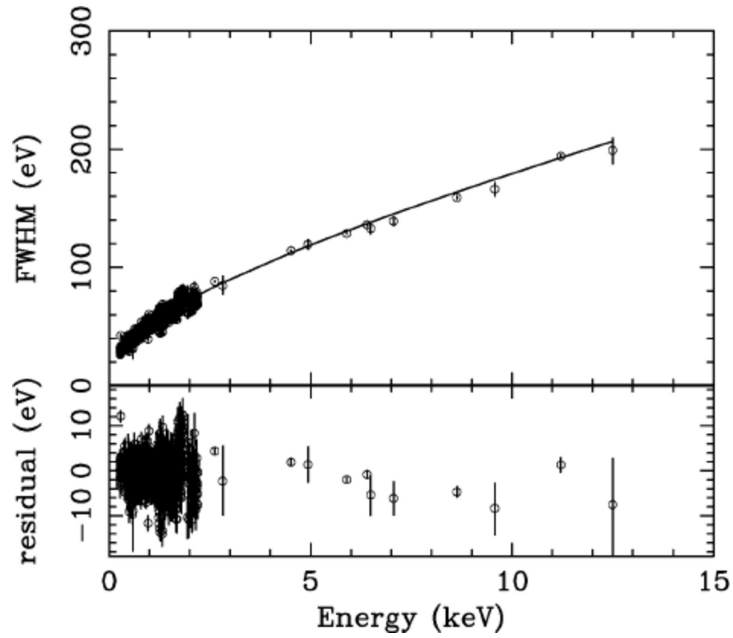


Figure 3.4: Energy resolutions of the XIS FI (XIS 2) taken from Koyama et al. (2007)

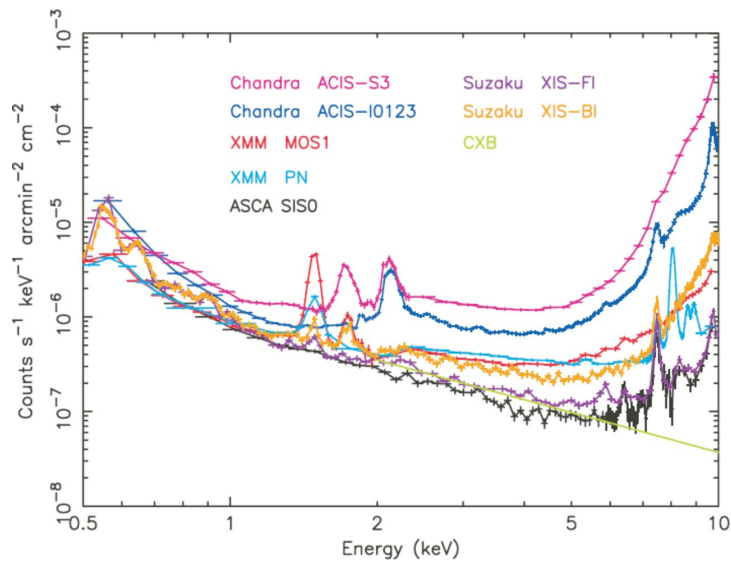


Figure 3.5: XIS background counting rate as a function of energy. The background rate of *ASCA*, *Chandra* and *XMM-Newton* adopted from Katayama et al. (2004) are shown for comparisons. This figure is taken from Mitsuda et al. (2007).

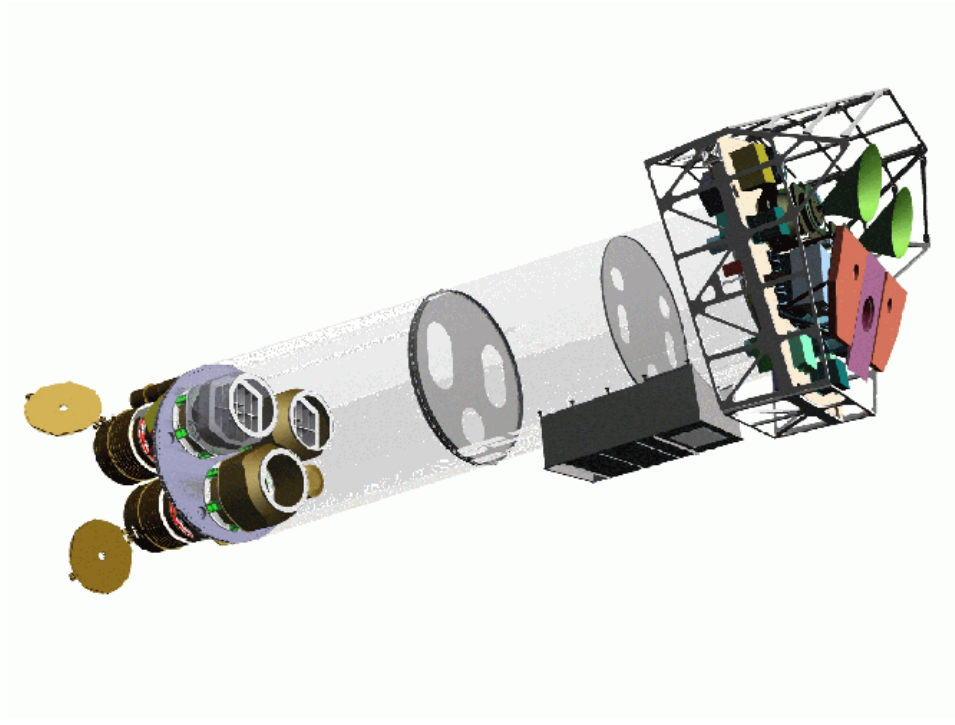


Figure 3.6: Sketch of *XMM-Newton* taken from Jansen et al. (2001).

Agency (ESA) Horizon 2000 programme, launched on December 10, 1999. After the launch, the satellite was sent to a highly eccentric orbit with a perigee of 7000 km and an apogee of 114000 km. Its inclination is $\sim -40^\circ$ and the orbital period is ~ 48 hour. *XMM-Newton* has two types of X-ray instruments, the European Photon Imaging Camera (EPIC) and the Reflection Grating Spectrometer (RGS). The EPICs are the X-ray-sensitive imaging CCDs covering an energy range from 0.15 keV up to 12 keV. The RGSs are spectrometers for high-resolution X-ray spectroscopy with an energy range of 0.35–2.5 keV.

Fig. 3.6 shows a sketch of *XMM-Newton*. Three X-ray telescopes are shown at the lower left of the figure, and two of these are equipped with Reflection Grating Arrays (RGA). The RGA diffract part of the incoming photons to the RGS detectors (pink) mounted on the focal plane shown at the right end of the assembly. The EPIC MOS cameras and the EPIC pn camera are also mounted on the focal plane. In the figure, these EPIC cameras can be identified with their radiators (black/green for MOS and violet for pn).

In the following subsections, only X-ray telescopes and EPIC cameras are described because we use only these instruments in this thesis.

Table 3.3: Specifications of the X-ray telescopes onboard *XMM-Newton*. Values are taken from *XMM-Newton Users Handbook*

Parameter	Value
Focal length	7.500 m
Number of modules	3
Effective area per telescope	1550 cm ² at 1.5 keV
Spatial resolution (HPD)	15''

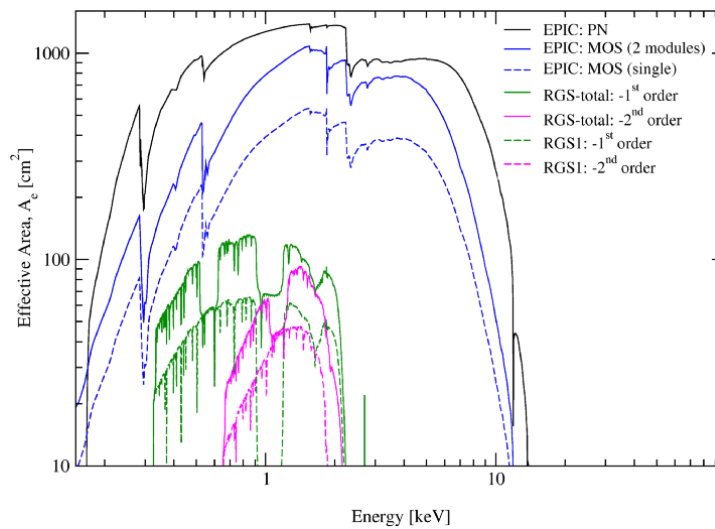


Figure 3.7: Effective area taken from *XMM-Newton Users Handbook*.

3.2.1 X-ray telescopes

Three X-ray telescopes onboard *XMM-Newton* are Wolter-I type telescopes. These consist of 58 mirrors nested in a coaxial and confocal configuration, which provide a large collecting area over a wide energy range.

The basic properties are listed in Tab. 3.3. The HPD of the telescopes are 15'', and the effective area is 1550 cm² for each telescope, so that it is 4650 cm² in total. Fig. 3.7 shows the net effective area of all X-ray telescopes of *XMM-Newton*. As mentioned in section 3.1.1, the effective area around ~ 7 keV is comparable to the XRT of *Suzaku*, but at lower energies, the X-ray telescopes of *XMM-Newton* is much better than *Suzaku* and the other instruments.

3.2.2 European Photon Imaging Camera (EPIC)

The focal plane detectors onboard *XMM-Newton* consists of two EPIC MOS CCD arrays (Turner et al., 2001) and a EPIC pn CCD camera (Strüder et al., 2001). The size of a

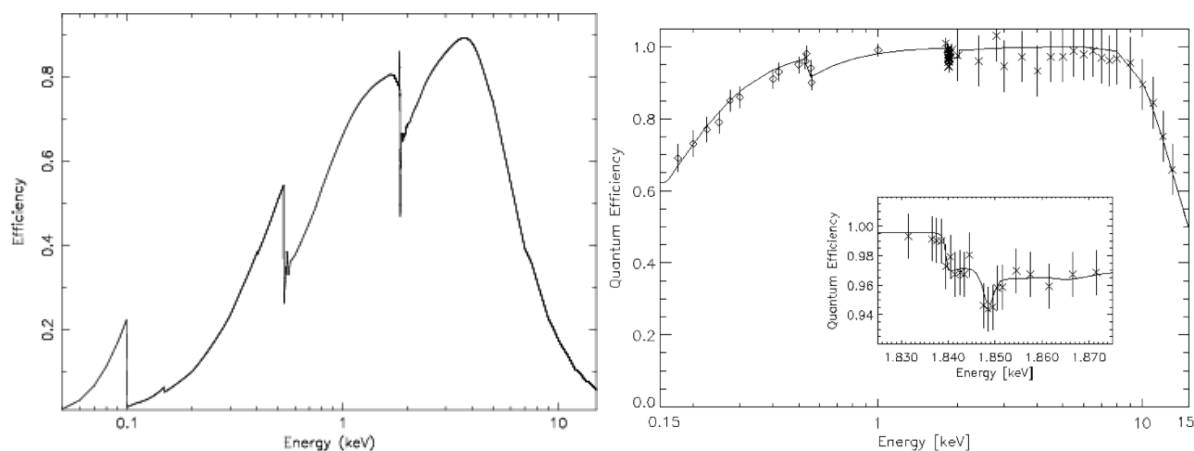


Figure 3.8: Quantum efficiency of MOS1 and pn. the figure for MOS1 is taken from *XMM-Newton* Users Handbook, and that for pn is taken from Strüder et al. (2001).

single MOS CCD chip is $25\text{ mm} \times 25\text{ mm}$, and a mosaic of 7 MOS CCDs covers the focal plane $28.4'$ (62 mm) in diameter on the sky. Each MOS CCD chip consists of 600×600 pixels, whose size is $40\text{ }\mu\text{m}$ square. The pn CCD is divided into 200×64 pixels with the larger pixel size of $150\text{ }\mu\text{m}$ square, and covers a $30\text{ mm} \times 10\text{ mm}$ region. These two kinds of detectors are fundamentally different, but the most important difference is that the MOS CCDs are front-illuminated and the pn CCDs are back-illuminated.

The strong point of the EPIC is a large effective area over a large energy range, which is better than the *Suzaku* XIS. As shown in Fig. 3.7, the effective area of the MOS cameras are worse than the pn camera because of the difference of their quantum efficiency. The quantum efficiency of the MOS and pn are plotted in Fig. 3.8. The difference of MOS and pn in a lower energy range is understandable by the fact that the MOS CCDs are front-illuminated. As for the higher energy, the difference of depletion thickness plays an important role. The actual mean depletion of the flight MOS CCDs is only $\sim 35\text{--}40\text{ }\mu\text{m}$, while that of the pn is $\sim 300\text{ }\mu\text{m}$.

The other important properties of the EPIC are the energy resolution and background rate. As listed in Tab. 3.4, the energy resolution of the EPIC is slightly worse than the *Suzaku* XIS. Also, the background of the EPIC is worse than *Suzaku* because the orbit of *XMM-Newton* satellite causes a flaring background. Such a flaring background component is produced by soft protons with energies less than a few 100 keV, which are thought to be organized in clouds populating the Earth's magneto-sphere. Fig. 3.9 shows a light curve of a MOS1 observation affected by the soft proton flares. Since the spectra of these flares are variable and have no clear correlation between their intensity and spectral shape, these flares are filtered by using light curves such like Fig. 3.9.

Table 3.4: Specifications of the EPIC. Values are taken from *XMM-Newton* Users Handbook

Parameter	MOS	pn
Field of view	30'	30'
Energy range	0.15–12 keV	0.15–12 keV
Pixel size	40 μm	150 μm
Energy resolution (FWHM)	~ 70 eV at 1 keV ~ 150 eV at 6.4 keV	~ 80 eV at 1 keV ~ 150 eV at 6.4 keV
Time resolution	1.75 ms	0.03 ms

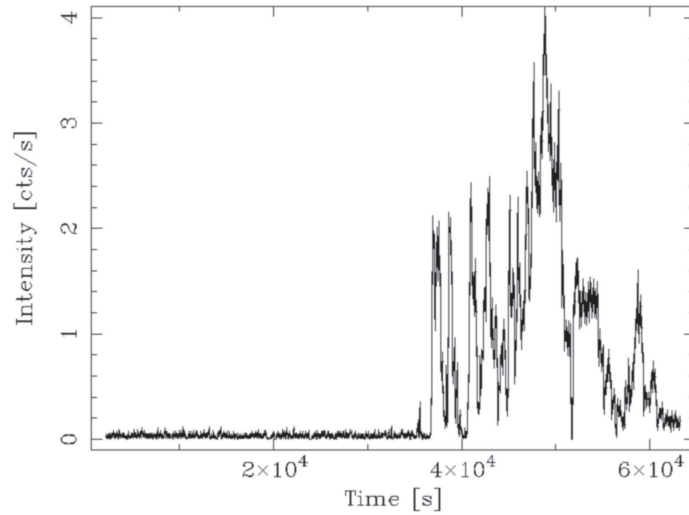


Figure 3.9: Light curve of a MOS1 observation affected by soft proton flares. This figure is taken from *XMM-Newton* Users Handbook.

Chapter 4

Disk wind model and calculation of the spectrum

In order to reveal the origin of the various spectra of UFOs depending on the observational epochs, we develop a new Monte Carlo simulation code, which can self-consistently calculate X-ray spectra reprocessed in an assumed 3-dimensional disk wind geometry. Our code implements radiative transfer in 3-dimensional biconical disk wind geometry, based on the Monte Carlo simulation framework called MONACO (Odaka et al., 2011), which has been developed by us through applications to a variety of astrophysical objects. In this chapter, we describe the details of our simulation code.

4.1 Approach to Radiative Transfer

4.1.1 Emission and absorption lines

The emission lines and the reprocessed continuum emissions from the outflowing materials should be modeled as well as the absorption lines for evaluating the physical properties of the outflows. In general, the absorption lines from outflows are accompanied by the emission lines (e.g., the P-Cygni profile; section 2.2.5), and such a reprocessed component can affect the depth of the absorption lines. Fig. 4.1 is an example of the spectra from a spherically symmetric outflow calculated by our Monte Carlo simulation code described in the following sections. This spectrum is calculated in the following physical conditions: the column density is $N_{\text{H}} = 2 \times 10^{23} \text{ cm}^{-2}$, the inner radius is $r_{\text{in}} = 10^{14} \text{ cm}$, the ionization parameter is $\xi = 10^4 \text{ erg cm s}^{-1}$ and the outflow velocity is $v = 0.3c$. The absorption lines in the transmitted spectrum (red) are deeper than those in the observed spectrum (black; the sum of the reprocessed and transmitted spectra). If the absorption

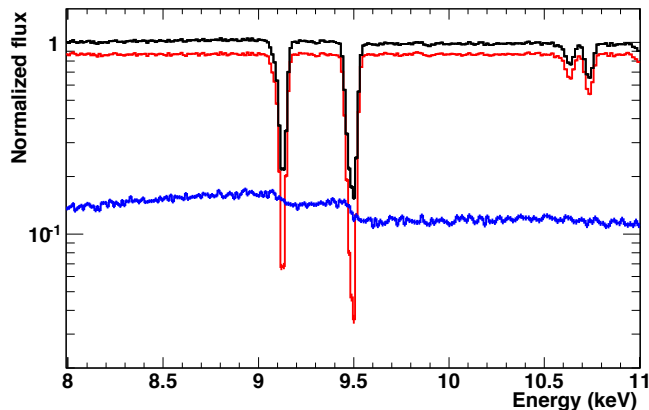


Figure 4.1: The spectra from a spherically symmetric outflow with a velocity of $0.3c$. The direct (transmitted) components are plotted in red, the reprocessed components are in blue and the sums of these components are in black.

lines in the observed spectrum (black) are fitted on the assumption of no contribution from the reprocessed components (blue), the column densities of Fe XXV and Fe XXVI are estimated to be $\sim 30\text{--}40\%$ smaller than the true values. Thus, calculating the reprocessed component and transmitted component self-consistently is essential to evaluate the absorption lines accurately.

Also, the emission lines themselves are important to understand the global structure of the wind. From the absorption lines, only physical properties of the material in our line of sight is available. In contrast to this, the emission lines enable us to investigate the materials located at the outside of our line of sight. Therefore, the emission lines are essential to probe the geometry and the density distribution of the outflow.

Currently, in most of the X-ray spectral analysis, the absorption lines and emission lines are treated as the independent components. This is because the quality of current observational data is not so good. Even for the data of highest quality, the error of the column density is $\sim 50\%$ (Reeves et al., 2009). However, in the near future, *ASTRO-H* (Takahashi et al., 2012) will change this situation by overwhelmingly high quality of its observational data. Therefore, it will be essential to self-consistently model the emission lines and the absorption lines from the outflow with a more realistic geometry.

4.1.2 Radiation transfer in a realistic geometry

In order to calculate the radiation transfer in the 3-dimensional realistic wind geometry, Monte Carlo simulation is the best and probably the only way. The well-established

analytical model for the radiation transfer in stellar winds is based on the Sobolev approximation (section 2.2.5), which assumes the spherical symmetry. Therefore, it is not applicable to the accretion disk winds including the UFO because most of the theoretical work predicts a biconical geometry (e.g., Elvis, 2000; Proga & Kallman, 2004; Fukumura et al., 2010).

Such full Monte Carlo radiation transfer simulations for AGN disk winds were performed by Sim et al. (2008, 2010a), but were applied to only two sources, PDS 456 (Reeves et al., 2014) and PG 1211+143 (Sim et al., 2010a). The other application to the observed data was Tatum et al. (2012), where their spectral model was used in order to search for Compton-thick outflows via a broad emission line structure.

Therefore, in order to use such full Monte Carlo simulations for the analysis of a variety of observational data, we develop by ourselves a new Monte Carlo radiation transfer simulation code. In our simulation codes, the calculation of the ionization structure and the radiative transfer simulation are separately performed in order to synthesize the spectrum from the ionized wind efficiently. In the first step, we determine the ionization structure, i.e. spatial distribution of the ion fractions and the electron temperature, by considering ionization and thermal balances when one-dimensional radiative transfer from the central source is assumed for simplicity. For this calculation we use XSTAR. Once the ionization structure is obtained, we then perform detailed three-dimensional radiative transfer simulation, which treats the Doppler effect due to gas motion and photon transport in a complicated geometry. This calculation procedure was established in the context of X-ray spectral modeling of a photoionized stellar wind in a high-mass X-ray binary (Watanabe et al., 2006).

Ideally, the radiative transfer simulation and the ionization structure calculation should be calculated iteratively since they are strongly coupled (see also section 2.3). However, it is not realistic to repeat the time-consuming Monte Carlo simulations many times. Therefore, we simply calculate the ionization structure by using XSTAR.

To construct the realistic geometry and the distributions of the velocity and density, we basically assume the UV-line driving mechanism. Currently, there is no general model for the UFOs, but two launching mechanisms (the UV-line driving and the magnetic driving) are thought to be the promising candidates. The UV radiation can be observed directly while the magnetic field can be hardly constrained. Therefore, the UV-line driving model is more firmly established, so that we adopt this model.

4.2 Monte Carlo simulation

4.2.1 MONACO framework

We use our Monte Carlo simulation code called MONACO (Odaka et al., 2011) for the detailed radiative transfer. MONACO is a general-purpose framework for synthesising X-ray radiation from astrophysical objects by calculating radiative transfer based on the Monte Carlo approach. This framework utilizes the Geant4 toolkit library (Agostinelli et al., 2003; Allison et al., 2006) in order to calculate particle trajectories and physical interactions of the particles with matter in a complicated geometry. MONACO is designed to treat astrophysical applications in which matter can form into an ionized plasma and can have motion that results in the Doppler shifts and broadenings. A variety of geometries and physical processes of photons are included and selectable for different astrophysical applications.

In the Monte Carlo simulation, a photon is tracked by calculating its propagation and interactions with matter. These calculations are performed in two steps as shown in Fig. 4.2. In the first step, the length to the next interaction position x is determined by sampling from an exponential distribution

$$P(x) = \frac{1}{l} \exp\left(-\frac{x}{l}\right). \quad (4.1)$$

Here, l is the mean free path

$$l = \frac{1}{\sum n_i \sigma_i}, \quad (4.2)$$

where n_i is a number density of a target material and σ_i is a cross section of an interaction labeled by i between the photon and the target, respectively. In the second step, the photon is absorbed or scattered, and then the next interaction position of re-emitted photon(s) or scattered photon is again determined by the first step. This repetition continues until the photon is absorbed or escapes from the system.

4.2.2 Atomic processes

In the MONACO, full treatment of photon processes related to an X-ray photoionized plasma are included. Detailed implementation of the physical processes is described in Watanabe et al. (2006). The simulation tracks photon interactions with ions, namely photoionization and photoexcitation; after these interactions reprocessed photons generated via recombination and atomic deexcitation continue to be tracked. Compton scattering by free electrons is also taken into account. In this work, we consider only H-

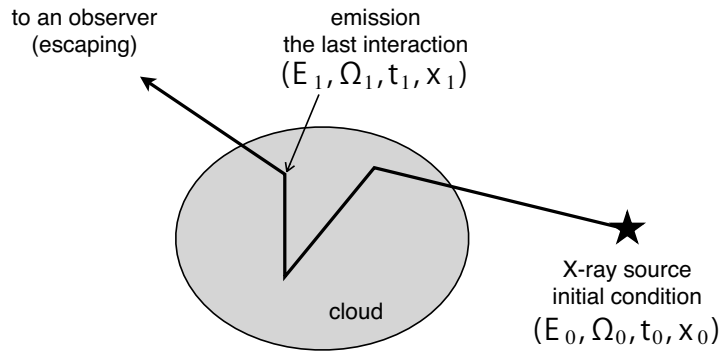


Figure 4.2: Schematic concept of the Monte Carlo simulation. This figure is taken from Odaka et al. (2011).

and He-like ions of Fe and Ni, and we ignore other ions. This assumption is justifiable by the fact that in the region of interest lighter elements are fully stripped, and L-shell ions of Fe and Ni with a few electrons have only a small impact on the absorbed spectrum even if they exist.

We demonstrate the consistency of the atomic processes between the ionization calculation code *XSTAR* and the Monte Carlo code *MONACO*. To compare *XSTAR* (version 2.2.1bn21) and *MONACO*, we assume a simple, spherical shell surrounding a point source at its center and calculate a spectrum emerging from this shell. The ionization parameter at the inner edge of the shell is set to $\log \xi = 4$ and the total column density of the shell is set to $N_{\text{H}} = 10^{23} \text{ cm}^{-2}$. These values are close to the typical ones of UFOs. The ionizing spectrum is assumed to be a power law with photon index $\Gamma = 2.2$ and luminosity $L = 10^{44} \text{ erg s}^{-1}$. The particle density is set to $n = 10^{12} \text{ cm}^{-3}$, so the thickness and inner radius are $\Delta R = 10^{11} \text{ cm}$ and $R = 10^{14} \text{ cm}$, respectively. In the *MONACO* simulation, the ion fractions and electron temperature calculated by *XSTAR* are used and the energies of incident photons are restricted to 2–40 keV. In order to identify all the lines, the turbulent velocity is $v_t = 0 \text{ km s}^{-1}$ so that only thermal broadening and natural broadening are included.

Fig. 4.3 shows the transmitted spectra calculated by *MONACO* (black) and *XSTAR* (red). These spectra are normalized by the incident spectra. In the top panel, the spectra are plotted with 10 times larger bin size than the original bin size of *XSTAR* to make the continuum spectral shape easier to see. As shown, the edge structure around 9–20 keV of the *MONACO* simulation matches well with the *XSTAR* simulation. Thus, we conclude that the photoionization process, which generates the absorption edge structure, is verified.

The lower panel of Fig. 4.3 shows the zoomed spectra output by *MONACO* and *XSTAR*.

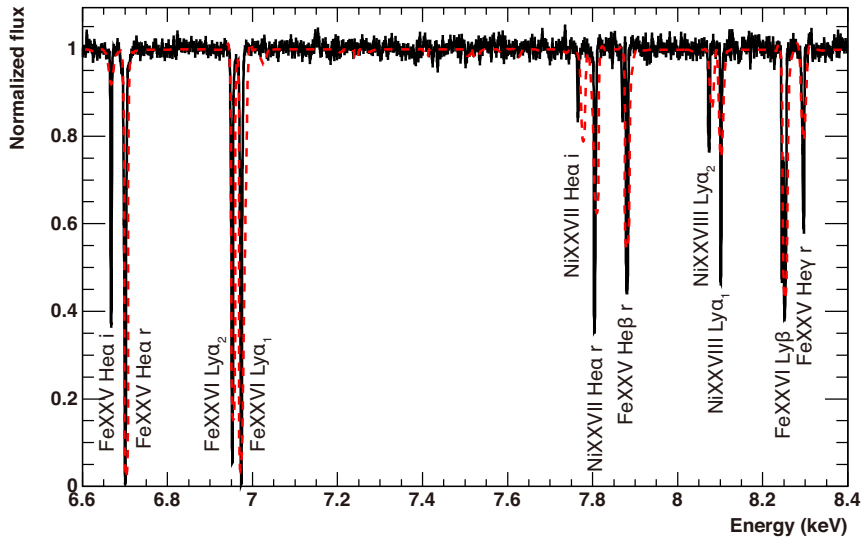
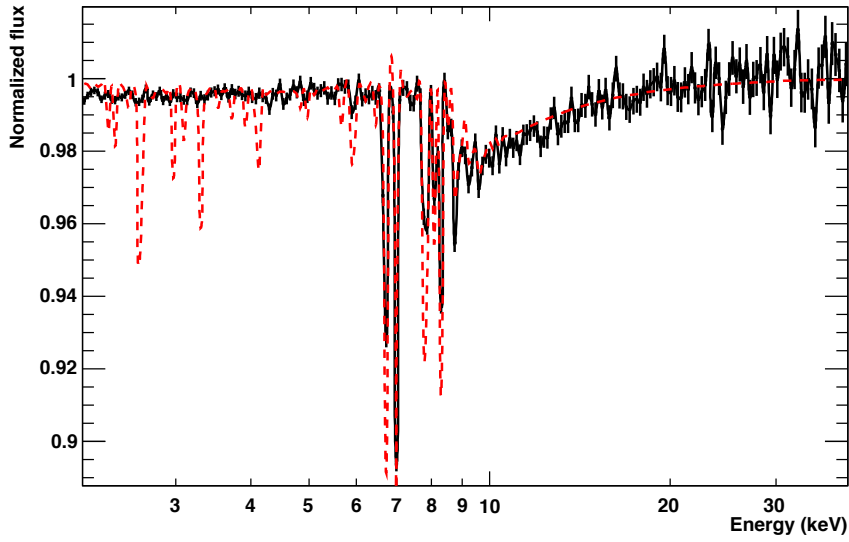


Figure 4.3: Comparison of the spectra calculated by MONACO (black) and XSTAR (red). Ionization parameter is a typical value for UFOs, $\log \xi = 4$. The turbulent velocity is $v_t = 0 \text{ km s}^{-1}$. *Top* : Rebinned to 10 times of the original bin size of XSTAR spectra. *Bottom* : Plotted in original bin size of XSTAR spectra.

The energies of absorption lines of both spectra are well matched except for the inter-combination lines of Ni XXVII He α . Tab. 4.1 shows the line energies and their oscillator strengths of important atomic transitions. For the comparison purpose, the data from AtomDB (<http://www.atomdb.org/>) are also listed in the table. As shown in the table, the energies of Ni XXVII He α triplet differs by ~ 10 eV depending on the databases so that such a small difference between XSTAR and MONACO is inevitable. The other difference in the table is that the fine structures due to total angular momenta J for the He-like Fe/Ni ions are ignored in XSTAR. However, this is not a major issue since the difference is only ~ 20 eV.

Most of absorption lines in the MONACO spectrum are deeper than XSTAR as shown in the top panel of Fig. 4.3. This is due to spectral calculation method used in XSTAR. When calculating the absorption line spectra, XSTAR simply evaluates the Voigt profile of the absorption lines at each energy grid. Since the grid spacing in XSTAR corresponds to 420 km s^{-1} , the maximum depth at the line center is not exact for narrow absorption lines.

Thus, we calculate again the spectra with a sufficiently high turbulent velocity $v_t = 500 \text{ km s}^{-1}$ to equalize the depths of the lines from the two codes, which is shown in Fig. 4.4. These two spectra show nice agreement in most of the lines. Only the strength of inter-combination lines of Fe/Ni He α triplet is inconsistent between XSTAR and MONACO spectra. This is caused by the inconsistency in the oscillator strength. In MONACO their oscillator strengths are $f_{lu} \sim 10^{-1}$ and 10^{-5} , while in XSTAR they are much stronger for Ni and weaker for Fe. Since the values in AtomDB are consistent with MONACO, we conclude that our values are likely to be correct.

Table 4.1: Comparison of the lines

LineID	Lower	Upper	XSTAR		MONACO		AtomDB		Notes
			Energy	f_{lu}^1	Energy	f_{lu}	Energy	f_{lu}	
Fe XXV He α <i>f</i>	$1s^2 \ ^1S_0$	$1s2s \ ^3S_1$	6.634	3.27×10^{-7}	6.637	3.09×10^{-7}	6.647	3.02×10^{-7}	
Fe XXV He α <i>i</i>	$1s^2 \ ^1S_0$	$1s2p \ ^3P_{1,2}$	6.673	1.43×10^{-5}	6.668	6.57×10^{-2}	6.677	5.77×10^{-2}	<i>y</i>
					6.682	1.69×10^{-5}	6.692	1.68×10^{-5}	<i>x</i>
Fe XXV He α <i>r</i>	$1s^2 \ ^1S_0$	$1s2p \ ^1P_1$	6.700	7.75×10^{-1}	6.700	7.26×10^{-1}	6.711	7.17×10^{-1}	
Fe XXV He β <i>r</i>	$1s^2 \ ^1S_0$	$1s3p \ ^1P_1$	7.881	1.52×10^{-1}	7.881	1.39×10^{-1}	7.892	1.37×10^{-1}	
Fe XXV He γ <i>r</i>	$1s^2 \ ^1S_0$	$1s4p \ ^1P_1$	8.296	5.66×10^{-2}	8.295	5.10×10^{-2}	8.309	4.77×10^{-2}	
Fe XXVI Ly α_2	$1s \ ^2S_{1/2}$	$2p \ ^2P_{1/2}$	6.952	1.36×10^{-1}	6.952	1.36×10^{-1}	6.955	1.34×10^{-1}	
Fe XXVI Ly α_1	$1s \ ^2S_{1/2}$	$2p \ ^2P_{3/2}$	6.973	2.71×10^{-1}	6.973	2.73×10^{-1}	6.976	2.69×10^{-1}	
Fe XXVI Ly β_2	$1s \ ^2S_{1/2}$	$3p \ ^2P_{1/2}$	8.246	2.59×10^{-2}	8.246	2.55×10^{-2}	8.250	5.03×10^{-2}	
Fe XXVI Ly β_1	$1s \ ^2S_{1/2}$	$3p \ ^2P_{3/2}$	8.253	5.17×10^{-2}	8.253	5.23×10^{-2}	8.256	1.02×10^{-1}	
Ni XXVII He α <i>f</i>	$1s^2 \ ^1S_0$	$1s2s \ ^3S_1$	7.727	5.13×10^{-7}	7.731	4.88×10^{-7}	7.744	4.74×10^{-7}	
Ni XXVII He α <i>i</i>	$1s^2 \ ^1S_0$	$1s2p \ ^3P_{1,2}$	7.773	2.64×10^{-1}	7.765	8.50×10^{-2}	7.778	7.46×10^{-2}	<i>y</i>
					7.786	2.29×10^{-5}	7.799	2.27×10^{-5}	<i>x</i>
Ni XXVII He α <i>r</i>	$1s^2 \ ^1S_0$	$1s2p \ ^1P_1$	7.801	6.84×10^{-1}	7.805	7.06×10^{-1}	7.819	6.98×10^{-1}	
Ni XXVIII Ly α_2	$1s \ ^2S_{1/2}$	$2p \ ^2P_{1/2}$	8.073	1.36×10^{-1}	8.073	1.36×10^{-1}	8.077	1.34×10^{-1}	
Ni XXVIII Ly α_1	$1s \ ^2S_{1/2}$	$2p \ ^2P_{3/2}$	8.102	2.70×10^{-1}	8.102	2.72×10^{-1}	8.105	2.68×10^{-1}	

¹ f_{lu} is oscillator strength.

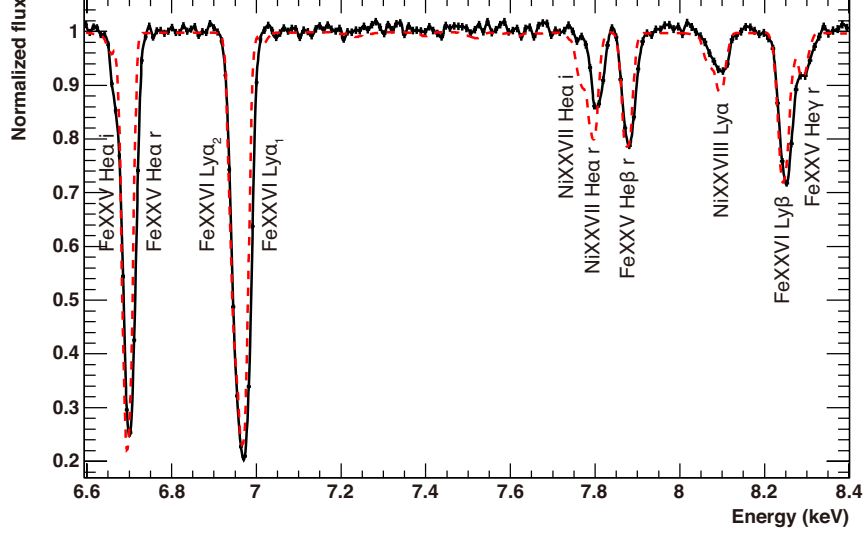


Figure 4.4: Comparison of the spectra calculated by MONACO (black) and XSTAR (red). All parameters are same as Fig. 4.3 except for the turbulent velocity $v_t = 500 \text{ km s}^{-1}$.

4.2.3 Relativistic effects

Doppler shift is one of the most important spectral characteristics in the absorption lines of UFOs. We check whether the Doppler shift is implemented correctly in the MONACO simulations, by assigning a bulk velocity of $v = 0.3c$ along z-axis to the spherical shell model used above. Since the velocity is along z-axis, the Doppler factor δ depends on the polar angle θ

$$\delta = \frac{1}{\Gamma(1 - \beta \cos \theta)}, \quad (4.3)$$

where $\Gamma = (1 - \beta^2)^{-1/2}$ is the Lorentz factor and $\beta = v/c$.

In the top panel of Fig. 4.5, the simulated spectra with $\cos \theta = 0.975$ (black), 0.525 (red), 0.025 (green), -0.475 (blue) and -0.975 (magenta) are shown. We fit the simulated spectra by

$$C \times \exp \left(- \sum_i N_i \sigma_i(E/\delta, \Delta E) \right), \quad (4.4)$$

where C is a constant for the continuum spectra, N_i is the column density, σ_i is the cross-section of Ly α or He α transition (Eq. 2.23) and i represents Fe XXV and Fe XXVI. For simplicity, we approximate the line profile to a Gaussian function with a Doppler

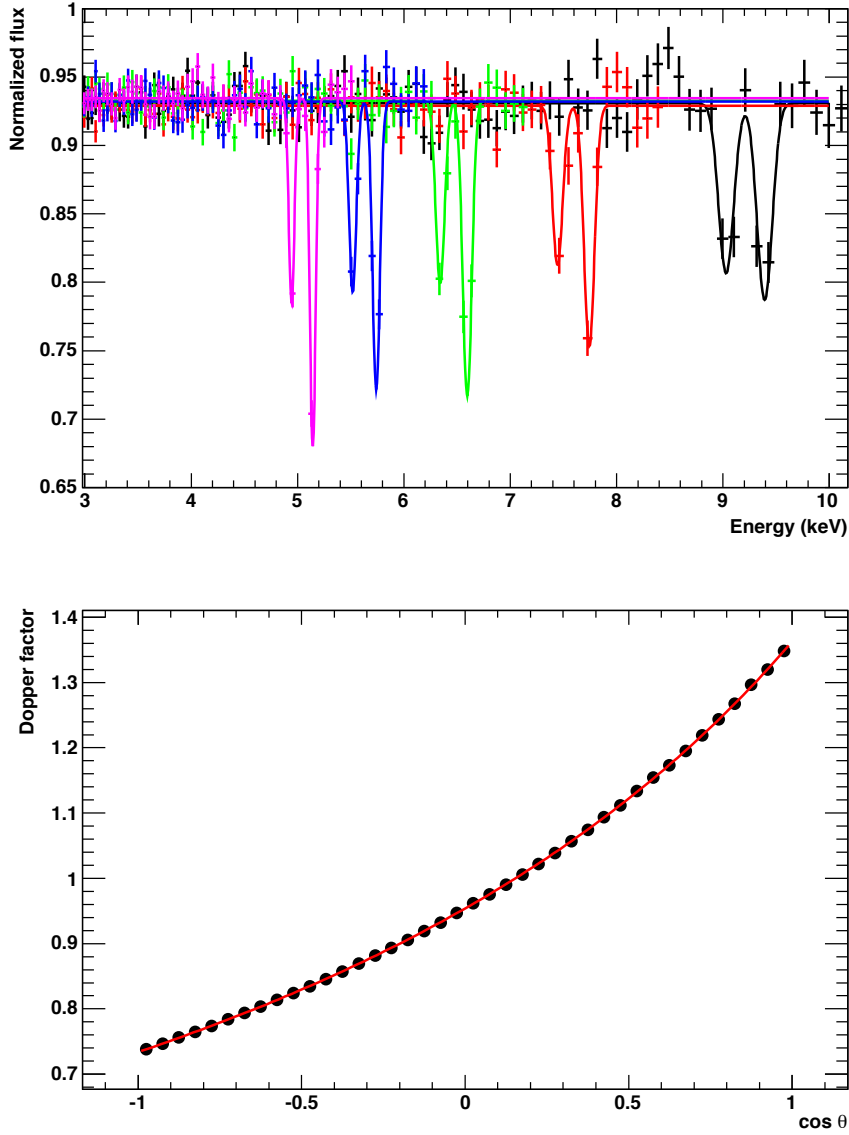


Figure 4.5: The top panel shows the MONACO spectra from the spherical shell with an outflow velocity of $0.3c$ observed from the various angles of $\cos \theta = 0.975$ (black), 0.525 (red), 0.025 (green), -0.475 (blue) and -0.975 (magenta). The data points are the simulated spectra and the lines are the best fit functions. In the bottom panel, Doppler factor obtained by fitting the simulated spectra are plotted against $\cos \theta$. The red curve is the expected function (Eq. 4.3).

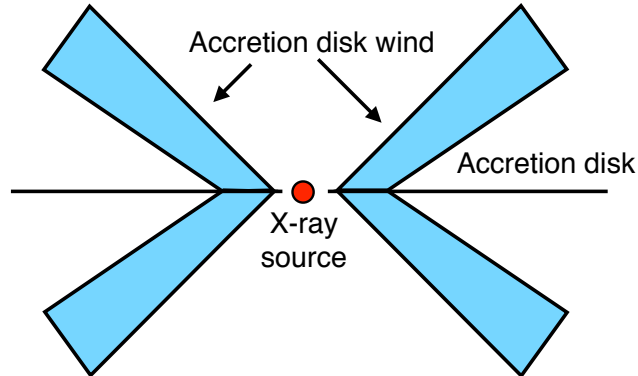


Figure 4.6: The schematic view of the bi-conical wind geometry (Shlosman & Vitello, 1993), which is adopted in our model. The cyan region is filled with the outflowing materials.

width ΔE and only Fe XXV He α and Fe XXVI Ly α lines are fitted. The best-fit functions for the spectra are overplotted in the top panel of Fig. 4.5.

We fit the simulated spectra for 40 angles ranging from $\cos \theta = -0.975$ to 0.975 . The obtained values of the Doppler factors are plotted as a function of $\cos \theta$ in the bottom panel of Fig. 4.5. The fitting errors are also plotted in the figure, but are too small to be seen. The red line in the figure is the theoretical function of Eq. 4.3. As shown, the simulation results are completely consistent with Eq. 4.3.

4.3 Wind geometry

We adopt a biconical geometry as shown in Fig.4.6, which was developed for studying radiative transfer in the wind of cataclysmic variables (Shlosman & Vitello, 1993) and widely used for accretion disk winds (Knigge, Woods & Drew, 1995; Sim et al., 2008, 2010a). As shown in Fig.4.7, this geometry is defined by three parameters. All streamlines in the wind converge at a focal point, which is at a distance d below the source. The wind is launched from R_{\min} to R_{\max} on the disk, we first assume that $d = R_{\min}$ and $R_{\max} = 1.5R_{\min}$. This means that the wind fills a cone between $\theta_{\min} = 45^\circ$ and $\theta_{\max} = 56.3^\circ$ that has a solid angle $\Omega/4\pi = 0.15$. We define a mean launch radius R_0 from the mean streamline i.e. it makes an angle of $\theta_0 \equiv (\theta_{\min} + \theta_{\max})/2$. Thus, $R_0 = d \tan \theta_0$.

The geometry is divided into 100 shells. Each shell has an equal width on a logarithm-

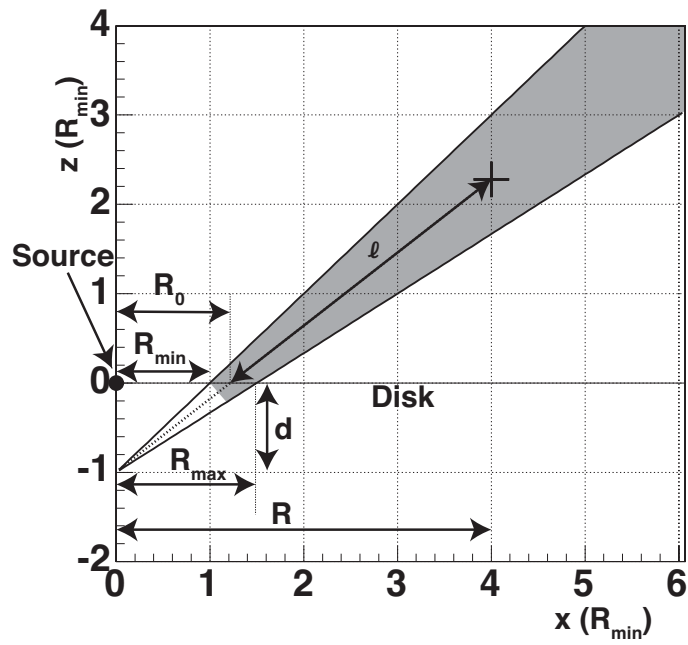


Figure 4.7: Adopted geometry for our wind model and geometric variables. The shaded region is filled with outflowing material. The wind is rotationally symmetric about the z -axis.

Table 4.2: Parameters of the simulation geometry and the seed photons

	Parameters	Values
Seed photons	Number of photons	1.2×10^8
	Initial direction (polar)	$\theta_{\min} - 90^\circ$
	Initial direction (azimuthal)	$0^\circ - 360^\circ$
Geometry	Number of division (radial)	100
	Number of division (polar)	2
	Number of division (azimuthal)	64
	Outer radius	$\sim 10^3 R_{\min}$

mic scale. It is also divided into 64 parts in azimuthal angle and 2 parts in polar angle since each volume can have only one velocity vector in this simulation code. Therefore, $100(\text{radial}) \times 64(\text{azimuthal}) \times 2(\text{polar})$ volumes are constructed in this Monte Carlo simulation. Initial directions of the seed photons are limited to the upper half of the disk because photons below the disk usually cannot penetrate the disk. These parameters are summarized in Tab. 4.2.

A radial velocity is defined as a function of length along the streamline l

$$v_r(l) = v_0 + (v_\infty - v_0) \left(1 - \frac{R_{\min}}{R_{\min} + l} \right)^\beta. \quad (4.5)$$

β determines the wind acceleration law, while v_0 and v_∞ are an initial radial velocity at $l = 0$ and a radial velocity at $l = \infty$. This equation is an extension of the classical CAK model (section 2.2.5). The azimuthal velocity at the launching point R_0 is assumed to be the Keplerian velocity $v_{\phi_0} = \sqrt{GM/R_0}$.

According to angular momentum conservation, v_ϕ is written as a function of R

$$v_\phi(R) = v_{\phi_0} \frac{R_0}{R}. \quad (4.6)$$

The turbulent velocity v_{turb} is composed of an intrinsic turbulent velocity v_t and a velocity shear (Appendix A4 of Schurch & Done 2007).

$$v_{\text{turb}}(i) = v_t + \frac{v_r(i) - v_r(i-1)}{\sqrt{12}}, \quad (4.7)$$

where index i refers to the shell number and v_r is a radial velocity.

According to mass conservation, total mass outflow rate \dot{M}_{wind} is constant. Therefore,

density n is written as

$$\dot{M}_{\text{wind}} = 1.23m_{\text{p}}nv_{\text{r}}4\pi D^2 \frac{\Omega}{4\pi} \quad (4.8)$$

$$= 1.23m_{\text{p}}nv_{\text{r}}4\pi D^2(\cos\theta_{\text{min}} - \cos\theta_{\text{max}}). \quad (4.9)$$

Here, $D = R/\sin\theta_0$ is the distance from the focal point, $1.23m_{\text{p}}$ is an ion mass and Ω is the solid angle of the wind including both sides of the disk.

4.4 Ionization structure

We calculate the ionization structure in the geometry and the distributions of the velocity and the density constructed in the previous section. To determine the ionization structure, XSTAR (Kallman et al., 2004) has been widely used in the X-ray community. XSTAR solves the ionization structure and the radiation field as a function of the distance from the source, by iteratively calculating the electron temperature, charge state distributions and level populations in the condition of thermal and ionization equilibrium.

We run XSTAR version 2.2.1bn16 to calculate the ionization structure sequentially from the inner shell to the outer shell. In the case of this wind geometry, the direct photons from the source should be considered as well as the transmitted photons from the previous shell. For a $(i + 1)$ th shell from the source, input photons (X_{i+1}^{in}) are calculated as follows:

$$X_{i+1}^{\text{in}} = (1 - f_{\text{direct}})X_i^{\text{out}} + f_{\text{direct}}X_0, \quad (4.10)$$

where X_0 is the photons directly come from the source, X_i^{out} is those transmitted and emitted outward from the i th shell and f_{direct} is the fraction of the direct component from the source. The fraction f_{direct} can be calculated geometrically (Fig. 4.8).

$$\alpha_0(i) = \arctan\left(\frac{D_{i+1}\sin\theta_{\text{min}}}{D_{i+1}\cos\theta_{\text{min}} - d}\right) \quad (4.11)$$

$$\alpha_1(i) = \arctan\left(\frac{D_i\sin\theta_{\text{min}}}{D_i\cos\theta_{\text{min}} - d}\right) \quad (4.12)$$

$$\alpha_2(i) = \arctan\left(\frac{D_i\sin\theta_{\text{max}}}{D_i\cos\theta_{\text{max}} - d}\right) \quad (4.13)$$

$$f_{\text{direct}} = (\alpha_1 - \alpha_0)/(\alpha_2 - \alpha_1) \quad (4.14)$$

An input spectrum for XSTAR should be defined in 1–1000 Ry (0.0136–13.6 keV) energy band. The ionization luminosity in this energy range is calculated from the 2–10 keV X-ray luminosity by extrapolating an X-ray powerlaw spectrum.

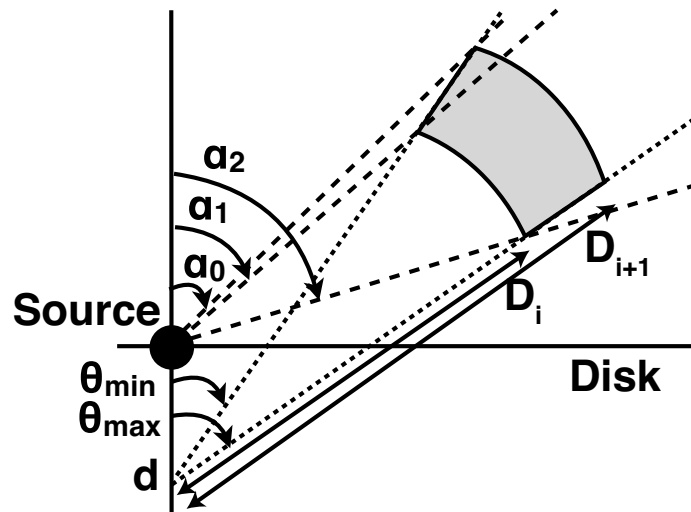


Figure 4.8: The geometry used for ionization calculation.

XSTAR requires a density n , a luminosity L and an ionization parameter $\log \xi = \log(L/(nR^2))$ as input parameters. The density and the luminosity are calculated by Eq.4.9 and Eq.4.14. To get the ionization parameter, the distance R is needed. Here, the distance R is defined to be the distance between the source and the inner edge of each shell. Additionally, we inputted a turbulent velocity calculated by Eq. 4.7. Atomic abundances are assumed to be equal to the solar abundances for all elements.

4.5 Comparison with previous work

In this section, we examine our simulation and physical simulation setup by comparing with the previous work. There are several differences between the treatments of our simulations and Sim et al. (2010a). Sim et al. (2010a) iteratively calculate radiation transfer and ionization and thermal balances. This is a similar method to XSTAR, but XSTAR can calculate only 1 dimensional radiation transfer. We calculate radiation, ionization and thermal balances in 3 dimensional geometry by sequentially running XSTAR for small shells. This method cannot trace photons scattered to azimuthal directions. Adiabatic cooling of the expanding wind is not included in the calculation of thermal balance in XSTAR, while it is included in Sim et al. (2010a). Sim et al. (2010a) consider only Doppler shift and ignore the other relativistic effects, while our simulation can correctly treat relativistic effects.

As described below in detail, only the difference of the relativistic effect affects spectral features, but the others are not so important for the spectral modeling.

Table 4.3: Model parameters used for the comparison between our wind model and Sim et al. (2010a)’s wind model.

Parameters	Values
Black hole mass	$4.3 \times 10^6 M_{\odot}$
X-ray (2–10 keV) luminosity	$10^{43} \text{ erg s}^{-1}$
Photon index	2.38
Inner launch radius R_{\min}	$100R_{\text{g}}$
Outer launch radius R_{\max}	$1.5R_{\min}$
Focal distance d	R_{\min}
Terminal velocity	$v_{\text{esc}} (\simeq 0.14c)$
Turbulent velocity v_t ¹	1000 km s^{-1}
Launch velocity ²	v_t
Mass outflow rate \dot{M}_{wind}	$0.1 M_{\odot} \text{ yr}^{-1}$
Outer radius of the wind	$5 \times 10^{16} \text{ cm}$

¹ Not explicitly given in Sim et al. (2010a).

² Although this is 0 km s^{-1} in Sim et al. (2010a), we fixed it at the turbulent velocity in order to avoid divergence of density.

4.5.1 Ionization structures

Firstly, we calculate the ionization structure and compare the results with the previous work (Sim et al., 2010a). The parameters assumed in this simulation are listed in Tab. 4.3. All the parameters are same as the previous work except for a turbulent velocity and a launch velocity. The value of the turbulent velocity is not described in Sim et al. (2010a) so we use a value selected for PDS 456 (see section 5.3.1). In Sim et al. (2010a), the launch velocity is written as equal to zero, but this causes a problem that the density at the launching point goes to infinity. This is because the density is proportional to the inverse of the velocity as shown in Eq. 4.9. Thus, to avoid this problem, we assume the launch velocity equals the turbulent velocity.

The ionization structure calculated as described in section 4.4 is shown in Fig. 4.9. The top panel is the results of our calculation, while the bottom panel is a figure taken from Sim et al. (2010a). The figures at bottom/top left show the mean charge states of Fe atoms, and the figures at bottom/top right are the electron temperature. All the figures are plotted as color maps on the wind geometry. Since the figures in the bottom panel are not made by us, the definition of colors is not identical with the figures in top panel. Except for the angular distributions, which are ignored in our calculations,

both electron temperature and mean charge state are consistent between our calculation and the previous one. The other major difference is a decreasing trend of the electron temperature at radius larger than $\sim 10^{15}$ cm seen in the bottom right panel. This is because Sim et al. (2010a) includes adiabatic cooling effects, which is ignored in our calculation using XSTAR. However, influence of this on the spectra is not critical because the electron temperature predominately affects radiative recombination processes, which does not make a substantial contribution on spectral feature.

All in all, the results of our simulation and Sim et al. (2010a)'s simulation are consistent except for the adiabatic cooling effect. Therefore, the difference in ionization calculations between our simulations and Sim et al. (2010a) is not crucial for the spectral modeling.

4.5.2 Doppler beaming

Now, we run a MONACO simulation in the ionization structure and electron temperature shown in Fig. 4.9 with an incident photon energy range of 2–500 keV. The simulated spectra are plotted in the right panel of Fig. 4.10. The left panel is taken from Sim et al. (2010a). The red, blue and black lines represent direct components (transmitted spectra), reprocessed components (emitted and scattered spectra) and sum of these components, respectively. The difference in the absorption lines below ~ 5 keV is because we treat only H/He-like Fe/Ni ions in order to speed up the simulations. The reprocessed components are clearly different between two simulations, while the direct components look similar in both simulations. This is because of Doppler beaming, which is ignored in the previous work.

The luminosity from a relativistically moving source is enhanced by the Doppler beaming effect

$$L(E) = \delta^3 L'(E') = \delta^3 L'(E/\delta), \quad (4.15)$$

where L is the source luminosity, δ is the Doppler factor defined by Eq. 4.3 and primes indicates the rest frame of the source. Here, the spectrum is a powerlaw $L(E) = L_0 E^{-\Gamma+1}$ so that

$$L(E) = \delta^3 L'_0 E^{-\Gamma+1} \delta^{\Gamma-1} = \delta^{2+\Gamma} L'(E). \quad (4.16)$$

Since we simulated with $\Gamma = 2.38$ and $v = 0.14c$, the beaming effect should be in the range of $\delta^{4.38} = 1.01$ – 1.80 , 0.83 – 1.85 , 0.77 – 1.85 , 0.72 – 1.80 and 0.66 – 1.69 for $\mu = 0.875$, 0.675 , 0.575 , 0.475 and 0.275 , respectively. All these values are consistent with the differences in the reprocessed spectra. Therefore, the Doppler beaming effect has a large impact on the reprocessed spectra.

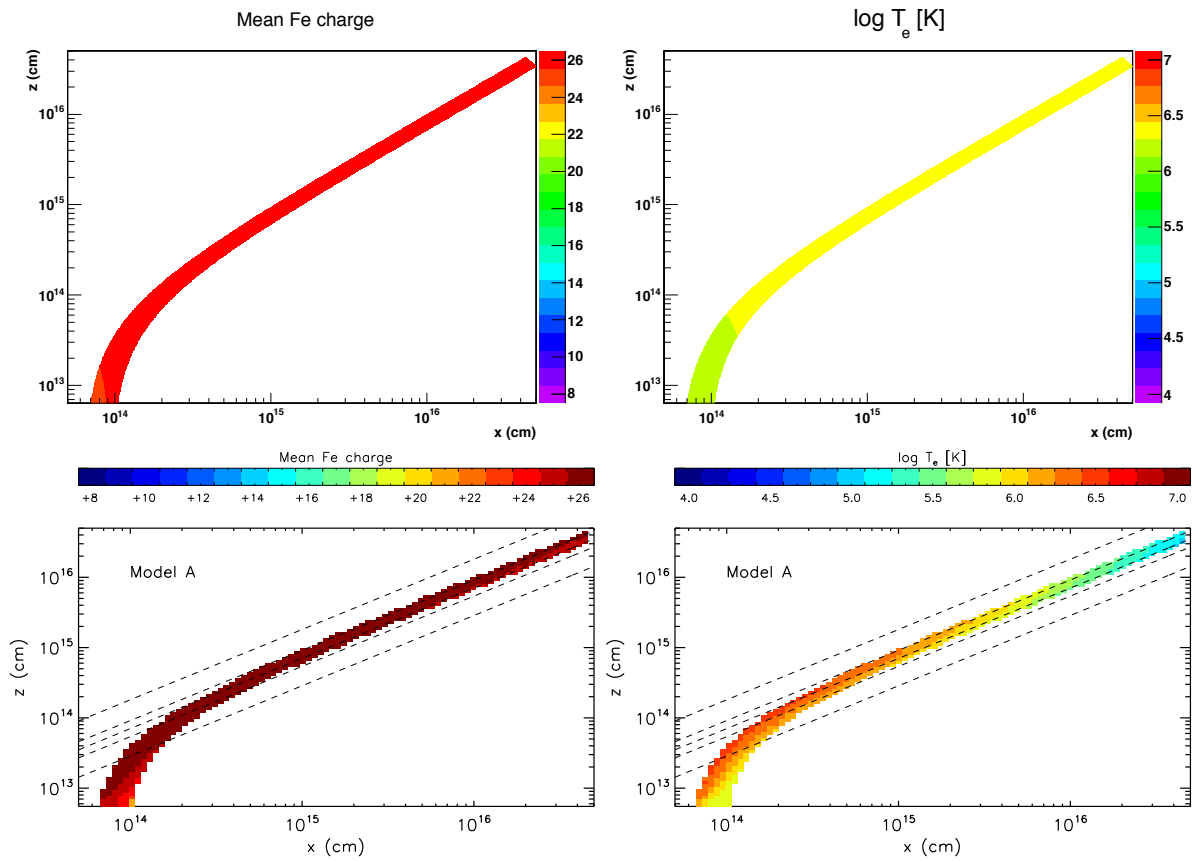


Figure 4.9: Distributions of mean Fe ionization state and kinetic temperature. The upper panel shows the mean charge states of Fe atoms (left) and the electron temperature (right) in the wind structure. The bottom panel is the same figures as the top panel but calculated by Sim et al. (2010a). Please be careful of the difference of the color definitions between top and bottom panels.

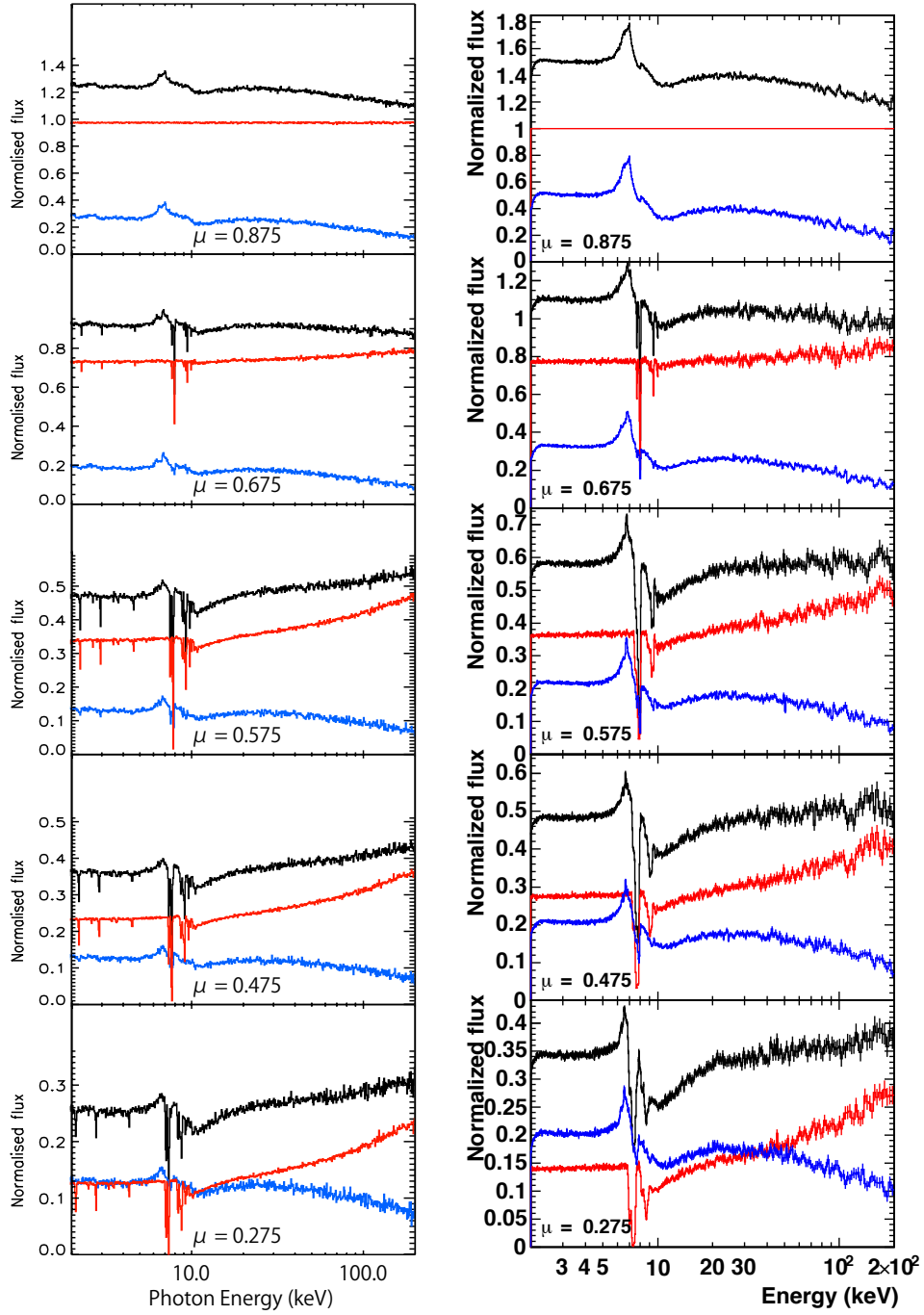


Figure 4.10: The simulated spectra for a various viewing angles ($\mu \equiv \cos \theta = 0.875, 0.675, 0.575, 0.475$ and 0.275) by the wind model in Sim et al. (2010a) (left) and our wind model (right). The direct components are plotted in red, the reprocessed components are in blue and the sums of these components are in black.

4.6 Phenomenological model for parameter search

Although MONACO is a powerful tool to analyze the wind spectra, it is too time-consuming for searching a large parameter space. Therefore, we also construct a phenomenological model, which is simpler than full Monte Carlo simulations but reproduces the major features of the wind spectra. This model is useful for evaluating a spectrum quickly and for searching a large parameter space.

4.6.1 Model description

The phenomenological model for the parameter search is composed of H/He-like Fe K lines and K edges convolved with various velocities in the wind. All K-shell absorption lines of H/He-like Fe ions with oscillator strength $f > 0.001$ are included. Transition energies and oscillator strength of these lines and the parameters for the absorption edges are extracted from the MONACO database.

The absorbed spectrum $F(\nu)$ is calculated as

$$F(\nu) = F_0(\nu) \exp \left[- \int \left(\frac{dN}{d\delta} \right) (\sigma_{\text{bb}}(\nu') + \sigma_{\text{bf}}(\nu')) d\delta \right] \quad (4.17)$$

$$\sigma_{\text{bb}}(\nu) = \frac{\pi e^2}{m_e c} f_{\text{lu}} \phi(\nu) \quad (4.18)$$

$$\sigma_{\text{bf}}(\nu) = \sigma_0 \left(\frac{\nu}{\nu_{\text{thr}}} \right)^\gamma \exp \left(-\frac{\nu}{\tau} \right), \quad (4.19)$$

where F_0 is the incident spectrum, σ_{bb} and σ_{bf} are the cross sections of the line transition (bound-bound) and photoionization (bound-free). In the Eq. 4.17, we divide the column density N to the velocity components, and the velocity is written as the Doppler factor δ . $\nu' = \nu/\delta$ is the frequency or energy of the photon in the rest frame of the wind. σ_0 , γ , τ and ν_{thr} in the photoionization cross-section are the parameters from MONACO database. For simplicity, we assume that the column density is independent of the Doppler factor δ , namely, the differential column density $dN/d\delta$ is constant.

Since we concentrate on the very fast outflows, the line width of the thermal or turbulence motion can be assumed to be larger than the natural broadening. Therefore, we approximate the line profile $\phi(\nu)$ to a Gaussian, and the Doppler width $\Delta\nu_{\text{D}}$ is fixed at $kT = 400$ keV, corresponding to $\sigma = 20$ eV.

Fig. 4.11 shows a schematic view of this model. The spectra shown in red, green and blue are composed of the absorption lines and edges at a single velocity component of $\delta = 1.32, 1.34, 1.36$, respectively. By convolving the absorption lines and edges with $\delta = 1.32$ – 1.36 , we obtain the black spectrum, which is our model. This model can reproduce the absorption features in MONACO spectra.

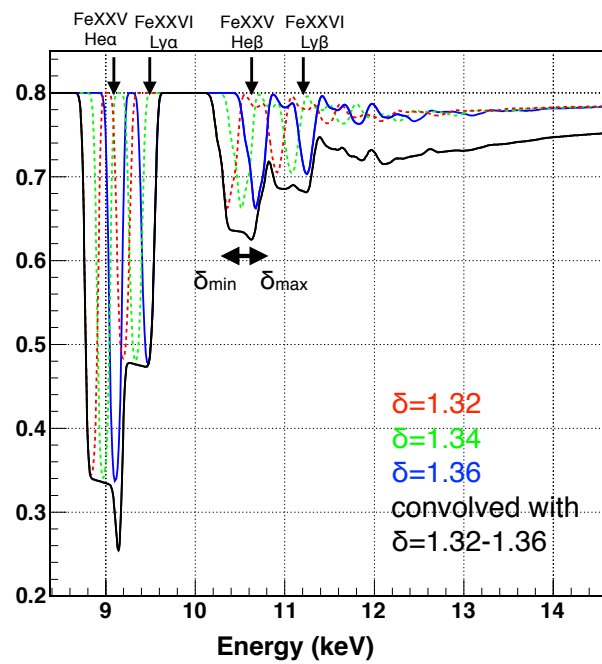


Figure 4.11: Schematic view of the phenomenological model for the parameter search. The absorption lines of the Fe XXV and Fe XXVI ions for the Doppler factors of $\delta = 1.32$ (red), 1.34 (green) and 1.36 (blue) are plotted with the dotted lines. The black solid line is the phenomenological model, which is convolved with the different velocity components of $\delta = 1.32-1.36$.

We implemented the model as a multiplicable model. Free parameters are a mean and a range of Doppler factor (δ_0 , $\Delta\delta$) and column densities of H/He-like Fe ions ($N(\text{Fe XXV})$, $N(\text{Fe XXVI})$).

4.6.2 Extraction of physical parameters of AGN winds from the spectral parameters

Since the free parameters (δ_0 , $\Delta\delta$, $N(\text{Fe XXV})$ and $N(\text{Fe XXVI})$) of the model defined in the previous section are not the physical parameters, we have to interpret them as the physical parameters used in the Monte Carlo simulations. The physical parameters for our MONACO simulation are a mass outflow rate $\dot{M}_{\text{wind}}/\dot{M}_{\text{Edd}}$, a minimum radius of the wind R_{min} , a terminal velocity v_{∞} , a ratio of maximum and minimum radius $R_{\text{max}}/R_{\text{min}}$ (corresponding to the covering fraction), minimum angle θ_{min} and inclination angle θ_{incl} . Therefore, we have 6 physical parameters while the spectral parameters are only 4. In order to extract physical parameters from the spectral parameters, we need some assumptions.

First, we fix the geometry of the wind at the values assumed in the modeling of PDS 456 ($R_{\text{max}}/R_{\text{min}} = 1.5$ and $\theta_{\text{min}} = 45^\circ$). This assumption enables us to constrain v_{∞} and θ_{incl} because δ_0 and $\Delta\delta$ depend on only these 2 parameters. Fig. 4.12 shows a parameter dependence on v_{∞} and $\Delta\theta \equiv \theta_{\text{incl}} - \theta_{\text{min}}$. By using this figure, we can draw the regions on the v_{∞} - $\Delta\theta$ plane, which correspond to the confidence intervals of δ_0 and $\Delta\delta$. Then, the overlap between the regions of δ_0 and $\Delta\delta$ is the allowed region for the terminal velocity v_{∞} and the relative angle $\Delta\theta$. One should note that these constraints are just a conservative one because v_{∞} and $\theta_{\text{incl}} - \theta_{\text{min}}$ can also be constrained by $N(\text{Fe XXV})$ and $N(\text{Fe XXVI})$.

Next, we estimate $\dot{M}_{\text{wind}}/\dot{M}_{\text{Edd}}$ and R_{min} . The inner radius of the wind R_{min} can be fixed at $2R_{\text{g}}/(v_{\infty}/c)^2$ by assuming $v_{\infty} = v_{\text{esc}}(R_{\text{min}})$. The mass outflow rate $\dot{M}_{\text{wind}}/\dot{M}_{\text{Edd}}$ can be estimated if we know the column density because we fix the geometry of the wind. But the spectral fitting does not give us the column density of all materials but of the H/He-like Fe ions.

In order to relate the mass outflow rate and the column density of the H/He-like Fe ions, we run XSTAR for the various values of the mass outflow rates. The XSTAR results provide us the abundance of the ions. Also, combined with the geometry, we can calculate the column density of Fe ions, which is the parameter obtained by the spectral fitting.

In addition to this, a correction factor for the column density is applied because the depths of absorption lines are smaller in the reprocessed component than that in the

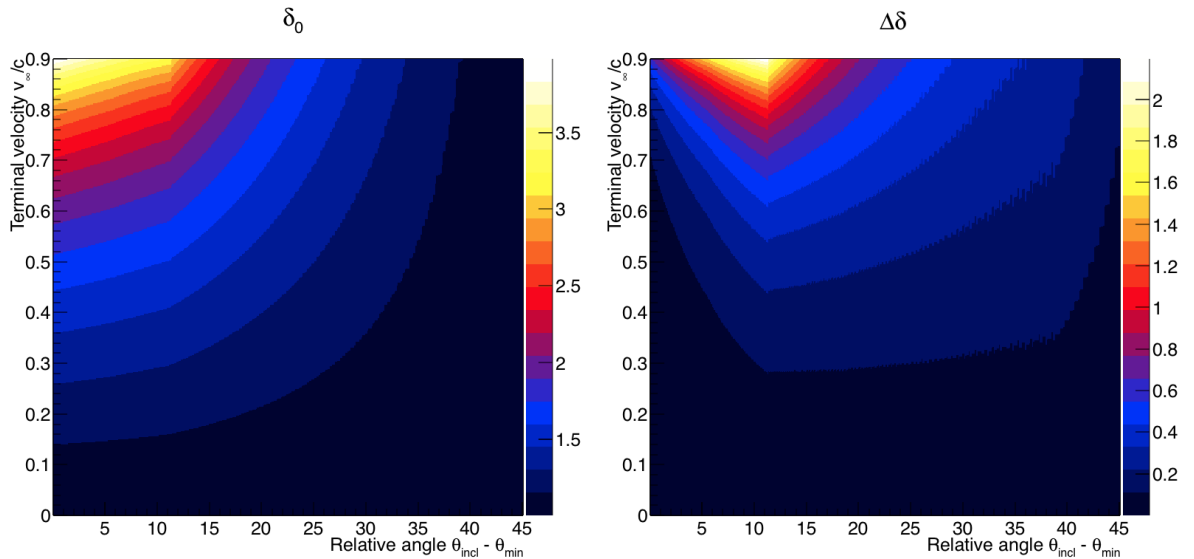


Figure 4.12: Dependence of the mean Doppler factor δ_0 and the width of the Doppler factor $\Delta\delta$ on the terminal velocity v_∞ and the relative angle $\theta_{\text{incl}} - \theta_{\text{min}}$. These maps are used to translate the spectral parameters (δ_0 and $\Delta\delta$) to the physical parameters (v_∞ and $\theta_{\text{incl}} - \theta_{\text{min}}$).

transmitted component. We fit the MONACO spectra with our phenomenological model, and obtain a ratio of apparent column densities between the transmitted component (red lines in Fig. 4.13) and sum of the reprocessed and transmitted component (black lines in Fig. 4.13). By using these values, we generate a correction factor as function of inclination angle.

4.7 Application to observational data

As we constructed a full Monte Carlo radiation transfer calculation of the UFOs, we are now able to study the structure of UFOs by applying our model to the observations of UFOs. Our simulations enable us to obtain the physical parameters of the wind, which can self-consistently explain the observed spectra.

A luminous quasar PDS 456 shows clear UFO features, whose significances of the blue shifted Fe XXV and Fe XXVI absorption lines are $\sim 3.6\sigma$ and $\sim 3.2\sigma$, respectively (Reeves et al., 2009). As well as its high significance of the UFOs, PDS 456 is known to have one of the most energetic UFOs with a high velocity of $\sim 0.3c$ and a large column density of $\gtrsim 10^{24} \text{ cm}^{-2}$ (Reeves et al., 2009). Because of these outstanding UFO properties, it is

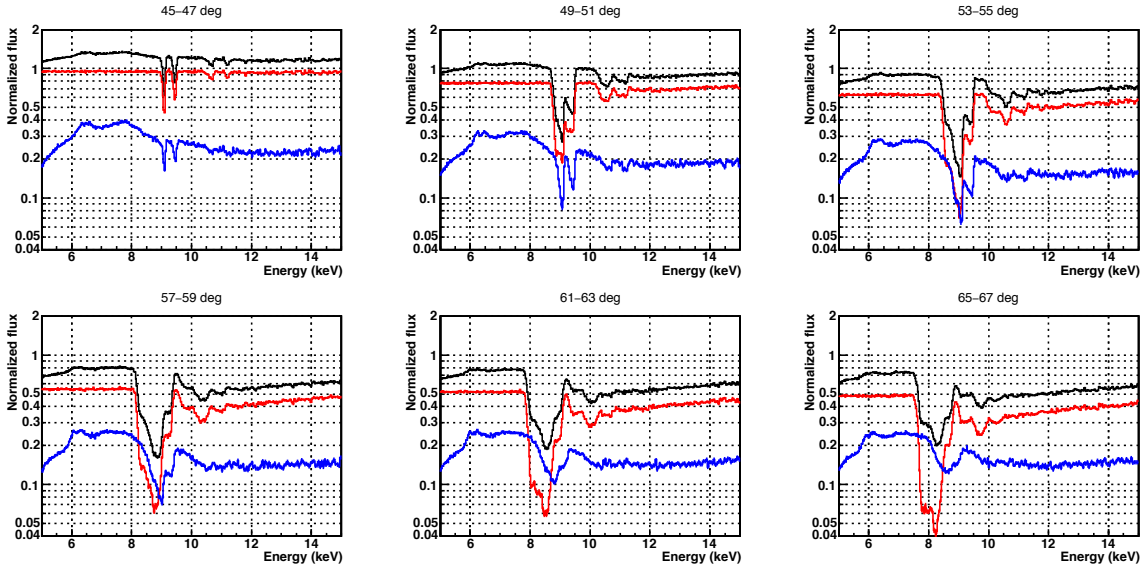


Figure 4.13: A variety of spectra simulated by MONACO. Each panel shows the spectra observed at a different line-of-sight orientation angle. The red, blue and black lines represent the direct components, reprocessed components and their sum, respectively. The parameters for these spectra are the same as the model for PDS 456: the terminal velocity is $v_\infty = 0.3c$ and the mass outflow rate is $\dot{M}_{\text{wind}}/\dot{M}_{\text{Edd}} = 0.13$.

obviously the best target to study the UFO physics in detail.

In order to investigate the essential and common physical properties of UFOs, we must analyze multiple targets and study their differences and similarities. The second strongest UFOs are observed in APM 08279+5255, which is a gravitationally lensed high redshift AGN. Thanks to such high redshift, the UFO features are observed at ~ 2 keV, where the sensitivity of current instruments is much better than $\gtrsim 7$ keV. Therefore, this is the second best target to study the wind structure with our wind model.

In the following chapters of this thesis, we apply our full Monte Carlo simulations to the multi-epoch observational data of PDS 456 and APM 08279+5255 for the purpose of revealing the essential physical parameters underlying in the various spectra of UFOs. Both of selected targets are observed several times, and show a large spectral variability in the absorption features. Such various spectra is suitable to find the underlying essential physical properties of the UFOs.

Also, these two sources show different kinds of absorption features. As shown in Fig. 4.13, MONACO simulation can generate various spectra depending on the observer's line of sight. The spectra of PDS 456 are similar to the top left panel in the figure, showing narrow absorption lines. On the contrary, APM 08279+5255 shows board absorption

lines mixed with absorption edges like the bottom right of the figure. In that sense, these two sources are interesting to study using our simulations.

Chapter 5

Analysis of PDS 456

PDS 456 ($z = 0.184$) is a luminous quasar showing a strongest UFO feature with an outflow velocity of $v \sim 0.3c$. The UFO in this source is the most powerful one known in the local Universe (Reeves, O'Brien & Ward, 2003; Reeves et al., 2009; Tombesi et al., 2010; Gofford et al., 2013). Therefore, this is the best target to study the physical properties of UFOs in detail by using our Monte Carlo simulations.

One more interesting property of this source is its strong variability in a time scale of as short as a few days (Reeves et al., 2002; Behar et al., 2010; Gofford et al., 2014; Reeves et al., 2014). Similar variability is observed in most of the UFO candidates as their appearance and disappearance depending on the observation epoch (Tombesi et al., 2010; Gofford et al., 2013). Therefore, this variability is possibly arise from a common essential properties of UFOs, so that revealing the origin of this variability would provide us a new insight into UFOs.

5.1 Observational data

Suzaku has observed PDS 456 between 2007 and 2013, for a total of five epochs as summarized in Table 5.1. Among these observations we choose the 2007 data, as this has strong wind absorption lines from H- and He-like iron. It also has a steep spectrum with very little absorption from lower ionization species as required by our code (see Reeves et al. 2009, 2014).

We processed and screened XIS data by running AEPIPELINE and applied default data screening and cleaning criteria: grade 0, 2, 3, 4 and 6 events were used, while hot and flickering pixels were removed, data were excluded within 436 s of passage through the South Atlantic Anomaly (SAA), and within an Earth elevation angle (ELV) $< 5^\circ$ and Earth day-time elevation angles (DYE_ELIV) $< 20^\circ$. The total net exposure

Table 5.1: *Suzaku* observations of PDS 456

Obs ID	Start Date	Net exposure (ks)
701056010	2007-02-24 17:58:04	190.6
705041010	2011-03-16 15:00:40	125.5
707035010	2013-02-21 21:22:40	182.3
707035020	2013-03-03 19:43:06	164.8
707035030	2013-03-08 12:00:13	108.3

time is 190.6 ks. Spectra were extracted from circular regions of $2.'9$ diameter, while background spectra were extracted from annular region from $7.'0$ to $15.'0$ diameter. We generated the corresponding response matrix (RMF) and auxiliary response (ARF) files by utilizing XISRMPGEN and XISSIMARFGEN. The spectra and response files for the two front-illuminated XIS 0 and XIS 3 chips were combined using the ftool ADDASCASPEC. The XIS spectra were subsequently grouped to HWHM XIS resolution of ~ 0.075 keV at 5.9 keV and ~ 0.020 keV at 0.65 keV, and then grouped to obtain a minimum 40 counts in each bin.

5.2 Spectral characterization

In this section, we characterize the spectra in order to estimate the input parameters for Monte Carlo simulations of the wind. Since the main interest of this paper is emission and absorption feature from the H- and He-like iron, we ignore the spectrum below 2 keV (observed frame) to exclude the soft excess. We assume that the 2-10 keV continuum can be modelled by a power law over this restricted energy band, with column density fixed to the Galactic value of $2 \times 10^{21} \text{ cm}^{-2}$.

5.2.1 Gaussian absorption and emission

Firstly, the absorption and emission lines are characterized by the simplest model, Gaussian. We fit two negative Gaussian lines to characterize the absorption, plus a single positive Gaussian line to characterize the emission atop a power law continuum. The equivalent width of the absorption lines is $0.110^{+0.035}_{-0.028}$ (He-like) and $0.094^{+0.025}_{-0.035}$ keV (H-like). We confirm the results of Reeves et al. (2009) that the He-like and H-like absorption features have slightly but significantly different blueshift, at $v_{\text{out}} = 0.295 \pm 0.005c$ (He-like) and $0.310 \pm 0.007c$ (H-like). The two absorption lines are constrained to have the same intrinsic width, which is marginally resolved ($\sigma = 0.048 (< 0.096)$ keV). By con-

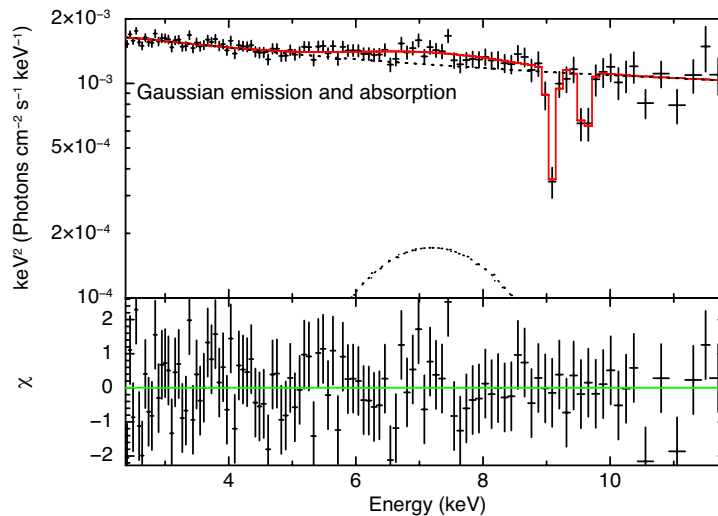


Figure 5.1: *Suzaku* spectra (black points) fitted with the Gaussian emission and absorption model (red solid line). The lower panel shows the residuals in units of χ . The spectra are shown in the rest frame of PDS 456.

trast, the emission line is extremely broad, with $\sigma = 1.3^{+1.5}_{-0.6}$ keV and equivalent width $0.35^{+0.28}_{-0.28}$ keV. The power law continuum is quite steep at $\Gamma = 2.34^{+0.10}_{-0.05}$, and this is a good fit overall, with $\chi^2/\text{dof} = 99.33/98$. All parameters are listed in Table 5.2.

5.2.2 Physical absorption lines: KABS and Gaussian emission

To estimate physical parameters for the following Monte Carlo simulations of the disk wind, we use a more physical absorption line model, where the column density is a fitting parameter. The absorption line profile should be a combination of a Gaussian core, with Lorentzian wings, with the ratio of these two components depending on the total optical depth of the line transition. This profile is incorporated in the KABS model (Kotani et al. 2000 including Erratum in 2006), with the free parameters being the column density of the ion, together with the temperature (equivalent to a turbulent velocity). We include Fe XXV (He-like) and Fe XXVI (H-like) $K\alpha$ and β , so have 4 absorption lines, but we note that the $K\beta$ lines are determined self consistently from the $K\alpha$ line parameters so the fit has the same number of free parameters as the fit with two lines.

This gives an equivalently good fit, with $\chi^2/\text{dof} = 91.74/98$. Again the He-like line velocity is significantly smaller than the H-like, at $0.294^{+0.004}_{-0.004}c$ compared to $0.310^{+0.007}_{-0.006}c$. The derived line broadening temperature of ~ 474 keV corresponds to a velocity width $\sigma = E_0(2kT/[(m_e c^2)(Am_p/m_e)])^{1/2} = 0.029$ keV i.e. a turbulent velocity of 1300 km s^{-1} , where A is an atomic mass.

Table 5.2: Spectral parameters of Gaussian emission and absorption model for the 2007 spectrum

Model Component	Fit Parameter	Value (90% error)
Powerlaw	Γ	$2.34^{+0.10}_{-0.05}$
	$F_{2-10 \text{ keV}}$ ($10^{-12} \text{ erg s}^{-1} \text{ cm}^{-2}$)	$3.77^{+0.07}_{-0.22}$
	$L_{2-10 \text{ keV}}$ ($10^{44} \text{ erg s}^{-1}$)	$3.52^{+0.07}_{-0.21}$
Fe XXV (6.6975 keV)	v_{out}	$0.295^{+0.005}_{+0.005}c$
	σ (keV)	$0.048 (< 0.096)$
	EW (keV)	$0.110^{+0.035}_{-0.028}$
Fe XXVI (6.9661 keV)	v_{out}	$0.310^{+0.007}_{-0.007}c$
	σ	tied to Fe XXV
	EW (keV)	$0.094^{+0.025}_{-0.035}$
Emission	LineE (keV)	$6.74^{+0.47}_{-1.32}$
	σ (keV)	$1.27^{+1.48}_{-0.59}$
	EW (keV)	$0.35^{+0.28}_{-0.28}$
Fit statistics	χ^2/dof	93.33/98
	Null probability	0.61
	χ^2/dof for 6.5–10.0 keV	13.90/20

Fixing both ions to this mean turbulence gives a column density of Fe XXV of $3.7_{-2.1}^{+18.9} \times 10^{18}$ and of Fe XXVI of $3.0_{-1.7}^{+8.1} \times 10^{18} \text{ cm}^{-2}$. The ratio is the important factor in determining the ionization state, and this gives $\text{H}/\text{He} \sim 0.8 (< 3.0)$. It seems most likely that $\text{H}/\text{He} \geq 1$ as otherwise we would expect a significant column density in Fe XXIV and below, which would result in significant $\text{K}\alpha$ absorption lines at lower energies which are not observed. Fixing $\text{H}/\text{He} = 2$ gives $N_{\text{H}}(\text{He}) = 2.2_{-1.2}^{+4.9} \times 10^{18} \text{ cm}^{-2}$ and $N_{\text{H}}(\text{H}) = 4.3_{-2.3}^{+9.9} \times 10^{18} \text{ cm}^{-2}$. These two ion states give an equivalent H column density is $N_{\text{H}} = (N_{\text{FeXXV}} + N_{\text{FeXXVI}})/A_{\text{Fe}} = 2.2 \times 10^{23} \text{ cm}^{-2}$ assuming $A_{\text{Fe}} = 3 \times 10^{-5}$. This is a lower limit as there can be a substantial fraction of material, which is fully ionized (Fe XXVII), which produces no absorption lines.

The strongest line (He-like $\text{K}\alpha$) is just saturated despite this large column density as the line velocity width is large. Hence the required column density does not decrease much with an increasing velocity. However, there is a limit to how high the turbulent velocity can be as velocities larger than 6000 km/s ($\sigma > 0.14 \text{ keV}$, $kT > 10000 \text{ keV}$) give lines, which are broader than observed. This forms a lower limit to the He-like and H-like column densities of 1.8 and $2.5 \times 10^{18} \text{ cm}^{-2}$, respectively. Decreasing the velocity mean both $\text{K}\alpha$ lines saturate, so the column density increases strongly. The lines are marginally resolved in the data, but the profiles are heavily saturated at very low line widths so the lines are broad despite the Doppler core being narrow. Thus there is no formal lower limit to the velocity. However, the gas is highly ionized so is also heated to the local Compton temperature which must be of order 10^6 K ($kT \sim 0.1 \text{ keV}$). This fixes the upper limit to the column density in He and H-like ions of 220 and $270 \times 10^{18} \text{ cm}^{-2}$. This would be Compton thick, with $N_{\text{H}} > 1.6 \times 10^{25} \text{ cm}^{-2}$.

5.2.3 Absorption accompanied by emission: PCYGX

In this section, we check if the very broad emission line obtained by the above analysis is consistent with the absorption lines. We can estimate the maximum emission that could be produced by the wind by using the P-Cygni profile code from Lamers, Cerruti-Sola & Perinotto (1987), as incorporated into XSPEC by Done et al. (2007). This code was designed to model O star winds, i.e. a spherically symmetric, radial outflow. This clearly differs from the diskwind geometry envisaged here, where the wind is not spherical and the velocity structure includes rotation as well as radial outflow. However, it gives a zeroth order estimate of the strength of emission, which might be produced.

The optical depth in each transition is parameterised as $\tau(w) = \tau_{\text{tot}}(1 - w)^\alpha$ where

$$w(r) = v(r)/v_\infty = w_0 + (1 - w_0)[1 - (r_{\text{launch}}/r)]^\beta \quad (5.1)$$

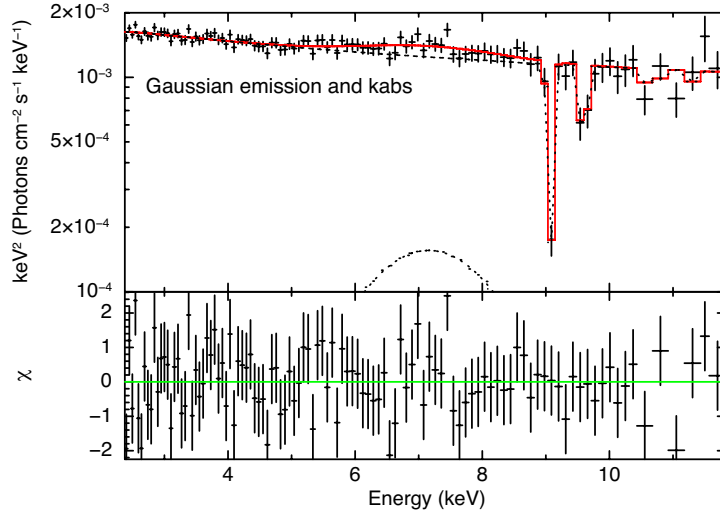


Figure 5.2: *Suzaku* spectra (black points) fitted with KABS and Gaussian emission (red line). The lower panel shows the residuals in units of χ . The spectra are shown in the rest frame of PDS 456.

Table 5.3: Spectral parameters of KABS model for the 2007 spectrum

Model Component	Fit Parameter	Value (90% error)
Powerlaw	Γ	$2.32^{+0.06}_{-0.05}$
	$F_{2-10 \text{ keV}} (10^{-12} \text{ erg s}^{-1} \text{ cm}^{-2})$	$3.78^{+0.11}_{-0.12}$
	$L_{2-10 \text{ keV}} (10^{44} \text{ erg s}^{-1})$	$3.53^{+0.10}_{-0.11}$
Fe XXV	v_{out}	$0.294^{+0.004}_{-0.004}c$
	kT (keV)	$474 (< 10484)$
	Natom (10^{18})	$3.7^{+18.9}_{-2.1}$
	EW (keV)	0.122
Fe XXVI	v_{out}	$0.310^{+0.007}_{-0.006}c$
	kT (keV)	tied to Fe XXV
	Natom (10^{18})	$3.0^{+8.1}_{-1.7}$
	EW (keV)	0.097
Emission	LineE (keV)	$6.8^{+0.4}_{-0.6}$
	σ (keV)	$1.1^{+0.9}_{-0.9}$
	EW (keV)	$0.271^{+0.199}_{-0.182}$
Fit statistics	χ^2/dof	91.74/98
	Null probability	0.66
	χ^2/dof for 6.5–10.0 keV	13.09/20

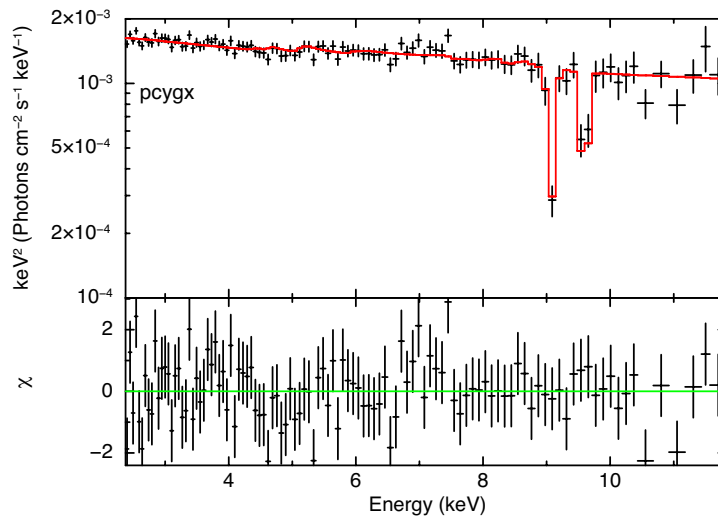


Figure 5.3: *Suzaku* spectra (black points) fitted with PCYGX (red line). The lower panel shows the residuals in units of χ . The spectra are shown in the rest frame of PDS 456.

where w_0 is the initial velocity of the material, β is a parameter determining the acceleration, which is fixed at 1. This gives $v_\infty = 1.05(1.09) \times 10^5 \text{ km s}^{-1}$ for He(H)-like, with a very steep $\alpha \sim -10$ (tied between both ions) and so that most of the column density is at $v \sim v_\infty$. Hence most of the emission is also concentrated at a velocity of $v \sim v_\infty$ but is produced at all azimuths, so the projected velocity (which sets the red and blueshifts) ranges from $-v_\infty \rightarrow v_\infty$ i.e. from 4.9-9.1 keV (He-like) and 5.1-9.5 keV (H-like).

The increase in χ^2/dof from 91.7/98 in KABS to 102.2/101 in PCYGX is significant at less than 99% confidence as there are 3 fewer degree of freedom (the emission line energy, width and intensity), so the F-statistic $F = \Delta\chi^2/\Delta\text{dof}$ becomes $10.5/3 = 3.5$. This shows that the observed broad emission is consistent with arising from the wind rather than requiring a substantial contribution from reflection from the disk.

5.3 Comparison of the Monte Carlo simulations and the 2007 spectra

5.3.1 Parameter choice

We translate the observational data above into appropriate simulation parameters. Firstly, we assume a minimum turbulent velocity $v_{\text{turb},0} = 10^3 \text{ km s}^{-1}$ (Reeves et al., 2009, 2014), and set $v_\infty = 0.3c$ (maximum velocity of H-like iron). This implies a launch radius of $R_{\text{min}} = 20R_g$ for $v_\infty = v_{\text{esc}} = c\sqrt{2R_g/R}$. We assume that this extends to

Table 5.4: Spectral parameters of PCYGX model for the 2007 spectrum

Model Component	Fit Parameter	Value (90% error)
Powerlaw	Γ	$2.37_{-0.03}^{+0.04}$
	$F_{2-10 \text{ keV}}$ ($10^{-12} \text{ erg s}^{-1} \text{ cm}^{-2}$)	$3.79_{-0.05}^{+0.05}$
	$L_{2-10 \text{ keV}}$ ($10^{44} \text{ erg s}^{-1}$)	$3.54_{-0.05}^{+0.05}$
Fe XXV (6.6975 keV)	v_{out}	$0.356_{-0.006}^{+0.007}c$
	τ_{tot}	$0.018_{-0.017}^{+6.577}$
	α	$-10.8_{-0.2}^{+1.6}$
Fe XXVI (6.9661 keV)	v_{out}	$0.378_{-0.009}^{+0.009}c$
	τ_{tot}	0.010 (< 2.544)
	α	tied to Fe XXV
Fit statistics	χ^2/dof	102.24/101
	Null probability	0.45
	χ^2/dof for 6.5–10.0 keV	15.36/23

$R_{\text{max}} = 1.5R_{\text{min}} = 30R_{\text{g}}$. We need the wind to be quite likely to intercept our line of sight in order to see absorption, so we assumed $\Omega/4\pi = 0.15$ (Tombesi et al., 2013).

We assume that the wind is radiation driven, so we can get some ideas of its polar angle from the ratio of a luminosity from $20 - 30R_{\text{g}}$, which will vertically accelerate the wind, to the luminosity from $6 - 20R_{\text{g}}$ which pushes the wind sideways (see e.g. Risaliti & Elvis 2010; Nomura et al. 2013). For a spin zero black hole accreting at $L = L_{\text{Edd}}$ we find $L(20 - 30R_{\text{g}}) = 0.64L(6 - 20R_{\text{g}})$, giving a polar angle of $\sim 57^\circ$. Hence we choose to fill the solid angle in a bicone from $45 - 56.5^\circ$ (Sim et al., 2010a,b).

Conservation of mass (Equation 4.8) means $n(R)$ is proportional to $1/(v_{\text{r}}(R)R^2)$. The total column density along the wind is $\int_{R_0}^{\infty} n(R)dR$, so for fast acceleration, where $v(R) \sim v_{\infty}$ for all R then $\dot{M}_{\text{wind}} = 4\pi v_{\infty} m_{\text{p}} (\Omega/4\pi) 1.23 N_{\text{H}} R_0$. The lower limit to the total hydrogen column density (from the upper limit to the turbulent velocity) implies $N_{\text{H}} = (N_{\text{FeXXV}} + N_{\text{FeXXVI}} + N_{\text{FeXXVII}})/A_{\text{Fe}} > 1.5 \times 10^{23} \text{ cm}^{-2}$ so the absolute minimum mass loss rate is $\dot{M}_{\text{wind}} \sim 0.5 M_{\odot} \text{ yr}^{-1}$ for $\Omega/4\pi = 0.15$. Conversely, the upper limit to the column density from the lowest velocity limit implies an upper limit to the mass loss rate of $\sim 50 M_{\odot} \text{ yr}^{-1}$, though it could be higher still if there is substantial material, which is completely ionized and hence invisible. However, these larger column densities have a very large optical depth to electron scattering ($\tau_{\text{T}} = 1$ corresponds to $N_{\text{H}} = 1.5 \times 10^{24} \text{ cm}^{-2}$ which corresponds to $5 M_{\odot} \text{ yr}^{-1}$), at which point the wind becomes self shielding, and radiative transfer within the wind would lead to low ionization species

which are not seen. Increasing the mass loss rate increases the optical depth, to $\tau = 10$ for $50 M_{\odot} \text{ yr}^{-1}$. This would completely obscure the X-ray source along all directions, which intercept the wind.

We can set an upper limit on the wind mass loss by the mass accretion rate. We use the accretion disk code OPTXAGNF (Done et al., 2012) with Galactic reddening of 0.48 (Simpson, 2005) and simulate an accretion disk spectrum for a black hole of mass $2 \times 10^9 M_{\odot} \text{ yr}^{-1}$ (Reeves et al., 2009). We match the observed B and V band fluxes (Ojha et al., 2009) for $L = 0.4L_{\text{Edd}}$ for a spin 0 black hole, i.e. a bolometric luminosity of $\sim 10^{47} \text{ ergs s}^{-1}$ and mass accretion rate of $\dot{M} = 31 M_{\odot} \text{ yr}^{-1}$. Alternatively, this gives $L = 2L_{\text{Edd}}$ for a spin 0.998, corresponding to $L_{\text{bol}} \sim 5 \times 10^{47} \text{ ergs s}^{-1}$ and mass accretion rate of $\dot{M} = 27 M_{\odot} \text{ yr}^{-1}$. The lack of dependence of the derived mass accretion rate on black hole spin is as expected, as spin only affects the disk structure on size scales comparable to the last stable orbit, whereas the optical emission, which we use to derive mass accretion rate is produced from further out in the disk. Clearly the maximum mass loss rate is then equal to the mass input rate of $30 M_{\odot} \text{ yr}^{-1}$, but we set a conservative limit of $15 M_{\odot} \text{ yr}^{-1}$, where we can lose up to half of the input mass accretion rate.

The density of the material is also determined by the opening angle of the wind with $n(R) \propto \dot{M}_{\text{wind}}/[R^2 v(R)(\Omega/4\pi)]$ (Equation 4.8). A wider opening angle means that the wind is more likely to intercept the line of sight, but also means that the same mass loss rate is spread into a larger volume, so this has lower density. This determines the ionization parameter $\xi = L/(nR^2) \propto v(R)(\Omega/4\pi)/\dot{M}_{\text{wind}}$, which controls the ratio of H-like to H-like ion column density. The fact that the data (weakly) require He-like and H-like to have different velocities implies that the ionization is not constant in the wind as might be expected if all the absorption is produced after the wind has been accelerated to its terminal velocity (so $v = v_{\infty}$ and is constant). This shows that it is feasible to use observational data to constrain the wind acceleration.

As a summary, we listed the chosen parameters for the simulation of the wind in PDS 456 in Tab. 5.5. Here, the parameters with same values as the sample model simulated in section 4.5 are not written in this table. The outer boundary of the wind geometry $5 \times 10^{18} \text{ cm}$ is selected to be much larger than an inner radius $R_{\text{min}} = 20R_g \simeq 5.9 \times 10^{15} \text{ cm}$ so that the density at the outer boundary is negligible compared with that at R_{min} . Although the photon index $\Gamma = 2.5$ seems to be larger than the observed value, there are no big change ($\log \xi$ decreases by 10–20%) even if we use $\Gamma = 2.2$.

We show results for $\dot{M} = 10 M_{\odot} \text{ yr}^{-1}$. We calculate the ionization using the measured 2–10 keV X-ray luminosity of $4 \times 10^{44} \text{ ergs s}^{-1}$. The results for this for a series of inclination angles through the wind are shown in Fig. 5.4. The lines clearly increase in both equivalent width and intrinsic width at higher inclinations, and the ratio of H-like

Table 5.5: Model parameters for MONACO simulations of PDS 456.

Parameters	Values
Black hole mass	$2 \times 10^9 M_{\odot}$
X-ray (2–10 keV) luminosity	$10^{44} \text{ erg s}^{-1}$
Photon index	2.5
Inner launch radius r_{\min}	$20R_g$
Terminal velocity	$0.3c$
Turbulent velocity v_t	1000 km s^{-1}
Mass outflow rate \dot{M}_{wind}	$10 M_{\odot} \text{ yr}^{-1}$
Outer radius of the wind	$5 \times 10^{18} \text{ cm}$

to He-like iron decreases.

Fig. 5.5 shows the ionization structure of the wind, with the lines of sight marked on it. At larger radii, the product of the density and the radius squared (nR^2) is almost constant according to Eq. 4.8, due to the saturated velocity. Therefore the H/He ratio shows a slight decrease, which is caused by the decrease of the luminosity due to the wind absorption. On the other hand, since the wind is still accelerating at the smaller radii, there is more He-like than H-like iron (see also Sim et al., 2008). As shown in the figure, the high inclination line of sight includes material at smaller radii, where the wind is denser and less ionized. This gives the increase in equivalent width and more He-like than H-like iron.

5.3.2 Absorption lines

In order to constrain the parameters efficiently, we first focus on only the absorption lines, which are more sensitive to the model parameters than the emission lines. The condition of the simulation adopted above is close to the largest feasible mass outflow rate, so is close to the lowest possible ionization for the observed 2–10 keV X-ray luminosity of $4 \times 10^{44} \text{ ergs s}^{-1}$ for the assumed launch radius of $20 - 30R_g$ and solid angle $\Omega/4\pi = 0.15$. However, it is remarkably difficult to reproduce the observed absorption line equivalent and intrinsic widths from this, irrespective of the velocity law chosen, as the material is very highly ionized (so produces a weak He-like line) except at high inclination angles. But at these high inclination angles, the line of sight intercepts a large range of velocities, so the lines are broad and blend into each other rather than producing the two narrow lines seen in the data. Also, material at high inclination is somewhat shielded from the ionizing luminosity by the rest of the wind. Hence it has lower ionization state, so at large inclinations, the He-like ion is produced preferentially at larger radii than the H-like ion,

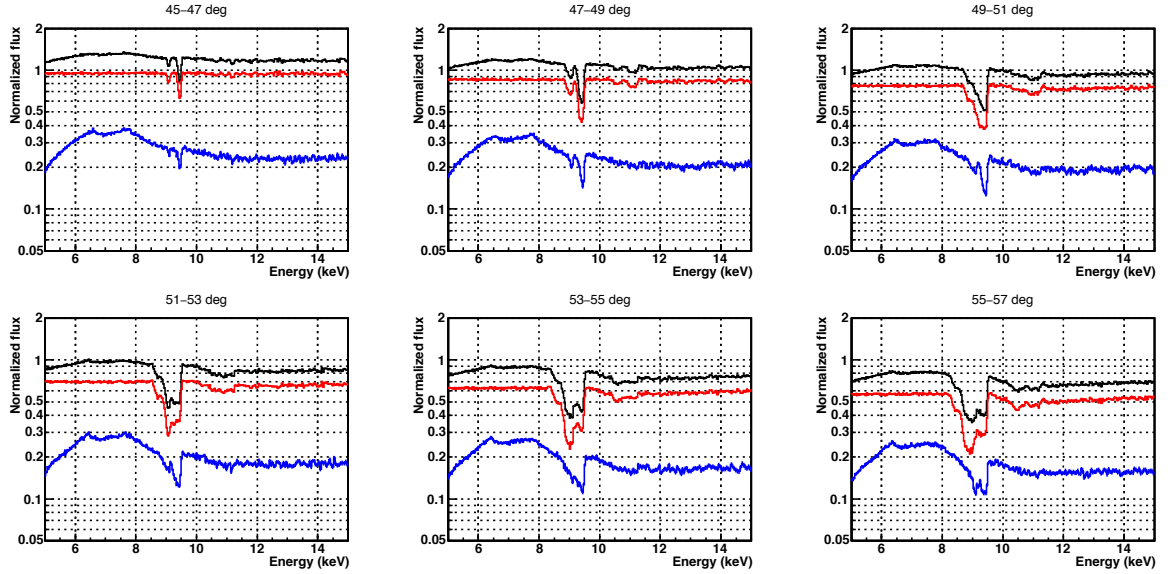


Figure 5.4: MONACO spectra with $L = 4 \times 10^{44} \text{ erg s}^{-1}$, $\dot{M} = 10 M_{\odot}$, $v_0 = v_{\text{turb}} = 1000 \text{ km s}^{-1}$, $\beta = 1$ and $R_{\text{min}} = 20R_g$. The direct component and reprocessed component are plotted in red and blue respectively. The total spectrum is plotted in black. Y-axis is normalized to the input powerlaw spectrum.

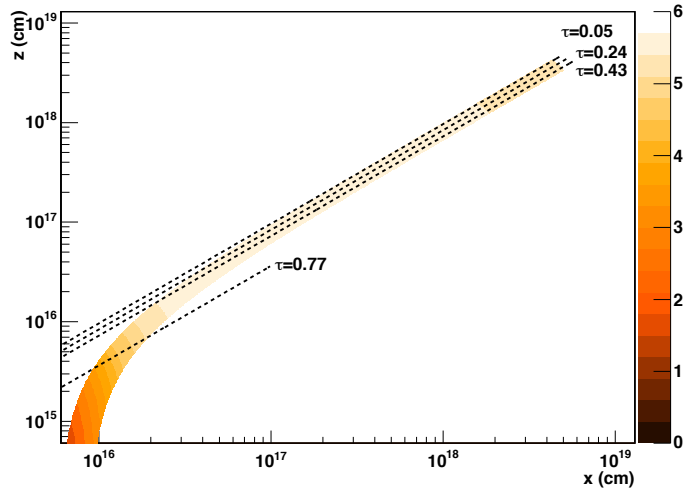


Figure 5.5: Ratio of H-like to He-like iron through the wind, together with the lines of sight for $\theta_{\text{incl}} = 46^\circ, 50^\circ, 54^\circ$ and 70° for the same simulation as in Fig. 5.4, labeled with the total column density along that line of sight. Higher inclination samples material at smaller radii, where it is still accelerating so the density is higher hence the abundance of He-like iron is higher.

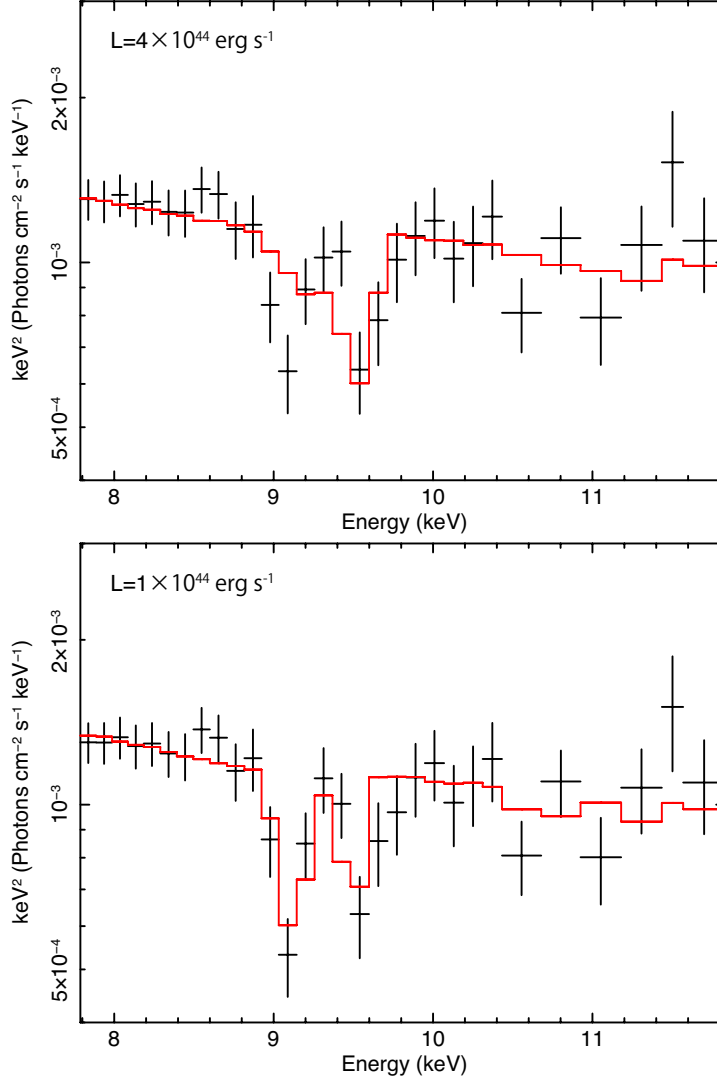


Figure 5.6: *Top* : *Suzaku* data and MONACO spectrum with $L = 4 \times 10^{44} \text{ erg s}^{-1}$, $\dot{M} = 10 M_{\odot} \text{ yr}^{-1}$, $v_0 = v_{\text{turb}} = 1000 \text{ km s}^{-1}$, $\beta = 1$ and $R_{\text{min}} = 20R_{\text{g}}$. Best fit parameters are $z = 0.165 \pm 0.007$ ($v \simeq 0.315c$), $\theta_{\text{incl}} = 49.0 \pm 0.9^{\circ}$ and $\Gamma = 2.35(\text{fix})$. Fit statistic is $\chi^2/\text{dof} = 32.32/27$. *Bottom* : Same figure as the left panel except with $L = 1 \times 10^{44} \text{ erg s}^{-1}$. Best fit parameters are $z = 0.174 \pm 0.005$ ($v \simeq 0.308c$), $\theta_{\text{incl}} = 47.1 \pm 0.4^{\circ}$ and $\Gamma = 2.35(\text{fix})$. Fit statistic is $\chi^2/\text{dof} = 21.48/27$. All spectra are shown in the rest frame of PDS 456.

giving the He-like line a higher outflow velocity than the H-like, contrary to observations. Thus both the narrow line width and the slightly higher velocity in H-like than He-like imply that the inclination angle through the wind is not too high, but low inclination angles through the wind are too highly ionized, producing too small an equivalent width of He-like Fe for low inclination angles through the wind, and too broad lines for higher inclination angles.

We show this by fitting the MONACO model to the 6.5–10 keV data. We tabulate the model as multiplicative factors, and apply these to a power law continuum with Galactic absorption. The MONACO model has two free parameters of redshift z and inclination angle θ_{incl} . We allowed redshift to be free rather than fixing it to the cosmological redshift of $z = 0.184$ as this allows us to fit for a slightly different wind velocity than is included in the simulation. The 6.5–10 keV spectrum is used in order to concentrate on the absorption lines. The best fit, shown in the left panel of Figure 5.6, is not very good, with $\chi^2/\text{dof} = 32/27$ in the 6.5–10 keV range. This is significantly worse than the phenomenological fits in Table 5.2, 5.3, 5.4. It is clear from the left panel of Figure 5.6 that the ionization state of this model is much higher than in the data.

Changing the velocity law does not substantially change this conclusion. A much higher initial velocity $v_0 = 0.15c$ gives a slightly better fit as this means that the higher inclination lines of sight through the wind intercept a smaller range of the velocity, so the lines are narrower. Similarly, decreasing β also gives a more homogeneous velocity structure as then most of the acceleration happens very close to the disk. Full results for these two cases are shown in the Appendix, but none of these give a particularly good fit to the data, with $\chi^2/\text{dof} > 33/27$ for the 6.5–10 keV bandpass.

Increasing the distance at which the wind is launched gives a lower ionization parameter. The UV line driven disk wind models of Risaliti & Elvis (2010) have $v_\infty/v(R_0)_{\text{esc}} \sim$ a few, at which point the wind could be launched at $R_{\text{min}} \sim 50R_g$. However, the ratio of accretion power at this point to the total accretion power is small, so such a wind would be expected to be more equatorial if it is driven by radiation as the ratio of the luminosity under the wind pushing it up $L(50 - 75R_g)$ is much smaller compared to $L(6 - 50R_g)$ which is the radiation from the inner disk pushing it outwards.

We cannot reduce the ionization by shielding the gas, as we observe $L_x = 4 \times 10^{44}$ ergs s^{-1} on our line of sight through the wind, so the wind also should see this luminosity. However, the outflow velocity is high enough that the X-ray luminosity as seen in the rest frame of the wind is substantially reduced by Doppler de-boosting, so that $L_{\text{obs}} = L_x \delta^{3+\alpha} \approx 0.25L_x$ where $\delta = [\gamma(1 - \beta \cos \theta)]^{-1} \approx 0.73$ (see Appendix A3 of Schurch & Done 2007). Thus the ionizing luminosity as seen by the wind varies from $4 - 1 \times 10^{44}$, depending on the velocity of the wind. Since the data show that the majority

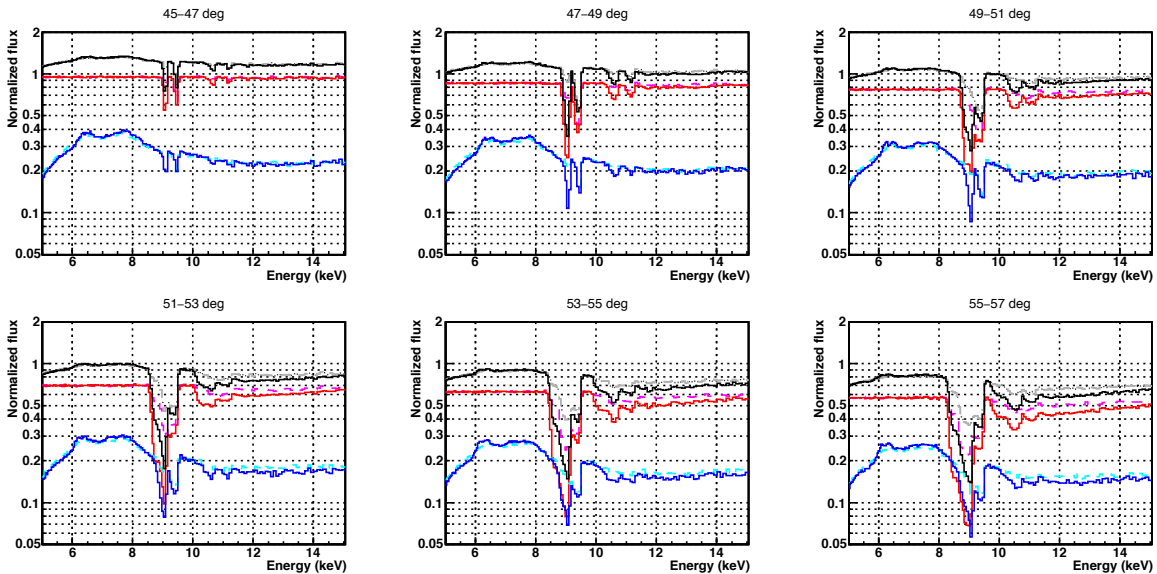


Figure 5.7: Dependence on the ionizing luminosity. The grey, magenta and cyan lines show the fiducial parameter simulation with $L = 4 \times 10^{44} \text{ erg s}^{-1}$, $\dot{M} = 10 M_{\odot} \text{ yr}^{-1}$, while the black, red and blue curves show the same parameters except with an ionizing luminosity $L = 1 \times 10^{44} \text{ erg s}^{-1}$.

of the absorption takes place at $v \sim v_{\infty}$, we use an ionizing luminosity of $10^{44} \text{ erg s}^{-1}$.

We re-simulate the wind over a range of parameters with this ionizing luminosity. The full simulation results are shown in Fig. 5.7 and Fig. 5.8, showing clearly that the ionization state is lower, as expected.

We fit this model to the data, with the best fit shown in the right panel of Fig. 5.6. This is a better fit, as expected, with fit statistic of 21.5/27, which is not significantly different to the phenomenological fits in Table 5.2, 5.3, 5.4. We also simulated with $\dot{M} = 15 M_{\odot} \text{ yr}^{-1}$, $8 M_{\odot} \text{ yr}^{-1}$, $3 M_{\odot} \text{ yr}^{-1}$, $1 M_{\odot} \text{ yr}^{-1}$. Although $15 M_{\odot} \text{ yr}^{-1}$ and $8 M_{\odot} \text{ yr}^{-1}$ give comparably good fits, lower wind outflow rates give increasingly poor fits ($\chi^2 = 28$ and 51 respectively) as the absorption lines become too weak.

By interpolating the values of χ^2 , the 90% confidence intervals of the mass outflow rate \dot{M}_{wind} and the terminal velocity v_{∞} are estimated to be $\dot{M}_{\text{wind}} > 6.7 M_{\odot} \text{ yr}^{-1}$ and $v_{\infty} = 0.308_{-0.010}^{+0.008} c$. We should note that these values are conservative because we assume the best fit value of the mass outflow rate is $10 M_{\odot} \text{ yr}^{-1}$. The value of χ^2 at the true minimum can be smaller than that at $\dot{M}_{\text{wind}} = 10 M_{\odot} \text{ yr}^{-1}$.

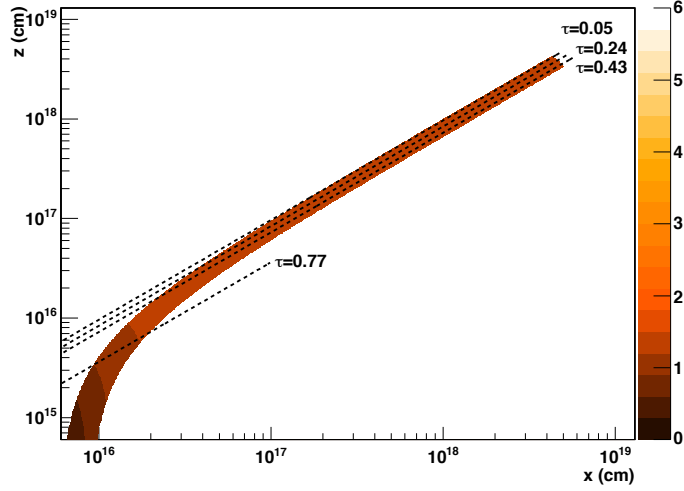


Figure 5.8: Ratio of H-like to He-like iron through the wind, together with the lines of sight for $\theta_{\text{incl}} = 46^\circ, 50^\circ, 54^\circ$ and 70° for the same simulation as in Fig. 5.7, labeled with the total column density along that line of sight. H-like ion is smaller than Fig. 5.5.

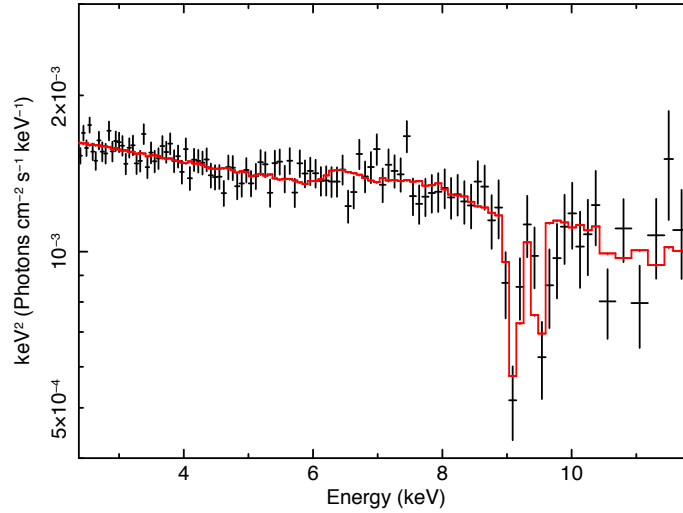


Figure 5.9: *Suzaku* data and MONACO spectrum in 2-10 keV band with $L = 1 \times 10^{44} \text{ erg s}^{-1}$, $\dot{M} = 10 M_{\odot} \text{ yr}^{-1}$, $v_0 = v_{\text{turb}} = 1000 \text{ km s}^{-1}$, $\beta = 1$ and $R_{\text{min}} = 20R_{\text{g}}$. Best fit parameters are $\theta_{\text{incl}} = 47.3 \pm 0.4^\circ$ and $\Gamma = 2.33 \pm 0.01$, and the redshift is fixed at $z = 0.174$ ($v \simeq 0.308c$). Fit statistic is $\chi^2/\text{dof} = 106.49/105$.

5.3.3 Emission lines from the wind

We now compare the emission lines of the MONACO spectrum and the observed spectrum, by re-simulating the best MONACO fit to the absorption lines shown in the right panel of Fig 5.6 over an extended energy grid from 2–200 keV. Fig 5.9 shows the best fit comparison of this simulation with the 2–10 keV Suzaku data, where the MONACO data are again incorporated as a multiplicative model. The fit parameters are power law index and normalization, and the redshift is fixed at $z = 0.174$ ($v_\infty \simeq 0.308c$). This gives $\chi^2/\text{dof} = 106.5/105$, which is not significantly worse than the phenomenological fits in Table 5.2, 5.3, 5.4 due to the smaller number of free parameters. For example, the model using KABS absorption lines with a broad Gaussian emission line has $\chi^2/\text{dof} = 91.7/98$, a difference of $\Delta\chi^2 = 15$ for 7 additional degrees of freedom. This gives $F = 15/7$ which is 2.1, which is only better at 96% confidence.

Unlike absorption, the line is emitted from the wind at all azimuths, and at all radii. Where the wind has already reached its terminal velocity, it has also expanded enough that its azimuthal velocity is small compared to its radial outflow velocity. Thus the projected velocity in our line of sight ranges from $-v_\infty$ ($\theta = 0$, along our line of sight as we look through the wind) to $-v_\infty \cos(\theta_{\text{incl}} + \theta_{\text{max}}) \sim -v_\infty \cos 2\theta_0$ giving a corresponding line energy of 6.04–9.13 keV for the 6.7 keV line while the 6.95 keV H-like extends from 6.26–9.47 keV for this simulation.

Thus the maximum red extension of the emission line can give direct information on the opening angle of the wind. However, this is difficult to measure as the line is very broad, and the discussion above neglects the emission from the wind at small radii where the initially Keplerian azimuthal velocity is important. This line emission from small radii could have a larger projected velocity with $-v_{\phi_0} \cos(\theta_{\text{incl}} + 90^\circ) \simeq (v_\infty/\sqrt{2}) \sin(\theta_{\text{incl}})$ at maximum, giving a red extension at ~ 5.7 keV for the He-like line. Our model shows that the red wing extends down to 6.0–6.3 keV (Fig 5.9). This would be better matched to the data if it happened at 6.5–6.7 keV, so we experiment with different θ_{min} but keep the same solid angle of the wind. We get better fit for a wind with $\theta_{\text{min}} = 35^\circ$ (Fig 5.10).

5.3.4 Emission lines from the wind and reflection from the disk

While the wind produces broadened emission lines from the H- and He-like material in the wind, the disk should also contribute to the emission via reflection. In our geometry, the disk still exists from $20R_g$ down to the innermost stable circular orbit. Hence we include neutral reflection (PEXMON) from this inner disk, with relativistic blurring from KDBLUR with outer radius fixed at $20R_g$, inner radius fixed at $6R_g$ and emissivity fixed at 3. We assume that the inclination angle for both PEXMON and KDBLUR is tied to

inclination angle of the wind model. We obtained fit statistics of 103.62, 105.69, 103.91, 107.93 and 111.16, with reflection fractions of 1×10^{-3} , 0.15, 0.27, 0.30 and 0.35 for respective values of $\theta_{\min} = 35, 45, 55, 65, 75^\circ$. We show the fit with $\theta_{\min} = 55^\circ$ as this allows a contribution from the inner disk reflection, as expected. The spectrum is shown in the right panel of Fig. 5.10.

5.4 Study of variability in absorption lines

In this section, we study the variability of the absorption lines in the PDS 456 spectra, by applying our MONACO models to the *Suzaku* data observed on 2011 March 16, 2013 February 21, 2013 March 3 and 2013 March 8 (Table 5.1). Hereafter, we refer to the data as 2011, 2013a, 2013b and 2013c respectively. The data were processed and grouped in the same way as the 2007 data. The total net exposure times are 125.5 ks, 182.3 ks, 164.8 ks and 108.3 ks respectively.

Figure 5.11 shows the fluxed spectra of all *Suzaku* observations. The spectra show a large variability in both the continuum shape and Fe absorption lines. At first sight this variability appears correlated, with strongest absorption lines in the hardest spectra. We first assess the extent of the correlation of the absorption with spectral shape using the KABS model, and then fit using the MONACO spectra.

5.4.1 Variability in continuum spectra and absorption lines

First, we characterize the observed spectral variability. Here, we assume that the intrinsic spectral shape is same as the 2007 observation, and only additional absorption makes spectral difference. Hence we model the continuum spectra by a powerlaw model with photon index $\Gamma = 2.35$ and an ionized partial covering absorber ZXIPCF. Additional Fe absorption lines are modeled with KABS models. The best fit parameters are listed in Table 5.6 and the spectra are shown in Fig. 5.12.

While the absorption lines are indeed strongest in one of the spectra with the strongest low energy absorption (2013c, cyan in Fig. 5.11) there is not a one-to-one correlation. The equivalent widths of absorption lines vary by more than a factor of 2 in 2013 data, while the continuum absorption is rather similar (2013a, b and c i.e. green blue and cyan in Fig. 5.11). Conversely, the absorption line equivalent width in 2013a (green in Fig. 5.11) is significantly less than that in the 2007 (unabsorbed) data. Thus the continuum shape change is not directly correlated with the wind, and is hence is unlikely to arise from a decrease in the ionization state of the entire wind structure. Instead, it more probably represents an additional absorbing cloud along the line of sight.

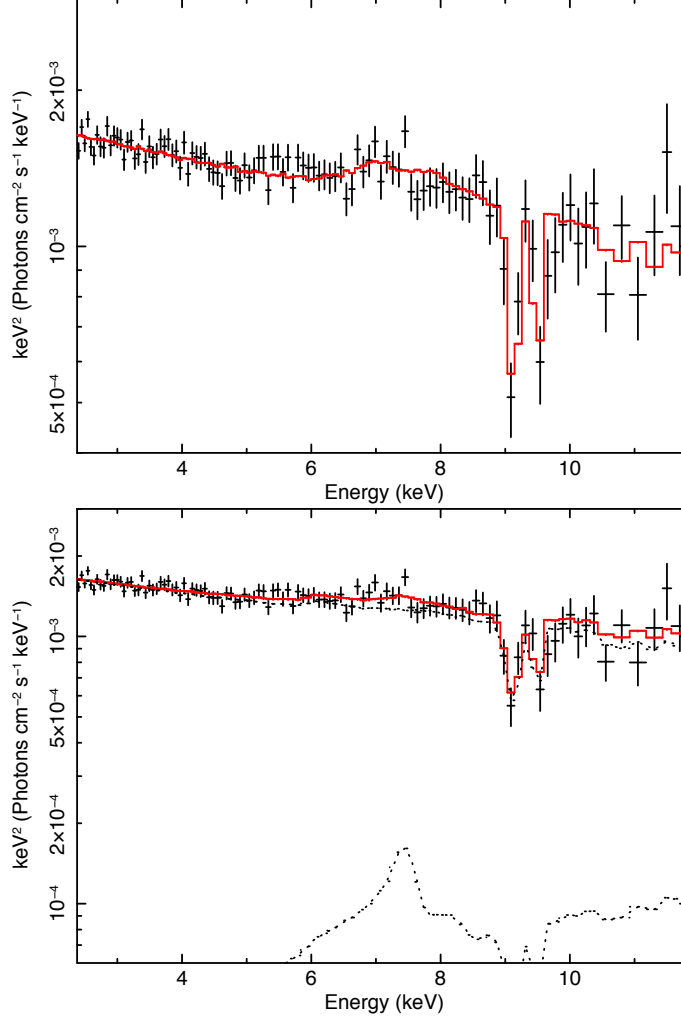


Figure 5.10: *Top* : *Suzaku* data and MONACO spectrum in 2-10 keV band with $L = 1 \times 10^{44}$ erg s $^{-1}$, $\dot{M} = 10 M_{\odot}$ yr $^{-1}$, $v_0 = v_{\text{turb}} = 1000$ km s $^{-1}$, $\beta = 1$, $R_{\text{min}} = 20R_{\text{g}}$ and $\theta_{\text{min}} = 35^{\circ}$. Best fit parameters are $\theta_{\text{incl}} = 37.4 \pm 0.4^{\circ}$, $\Gamma = 2.30 \pm 0.01$, and the redshift is fixed at $z = 0.174$ ($v \simeq 0.308c$). Fit statistic is $\chi^2/\text{dof} = 103.62/105$. *Bottom* : *Suzaku* data and MONACO spectrum with blurred disk reflection (black dotted line at the bottom of the spectrum) in 2-10 keV band with $L = 1 \times 10^{44}$ erg s $^{-1}$, $\dot{M} = 10 M_{\odot}$ yr $^{-1}$, $v_0 = v_{\text{turb}} = 1000$ km s $^{-1}$, $\beta = 1$, $R_{\text{min}} = 20R_{\text{g}}$ and $\theta_{\text{min}} = 55^{\circ}$. Best fit parameters are $\theta_{\text{incl}} = 56.8 \pm 0.3^{\circ}$, $\Gamma = 2.40 \pm 0.04$ and reflection fraction $R \simeq 0.27$, and the redshift is fixed at $z = 0.174$ ($v \simeq 0.308c$). Fit statistic is $\chi^2/\text{dof} = 103.91/104$. We changed the y-axis scale to show the reflected spectrum. All spectra are shown in the rest frame of PDS 456.

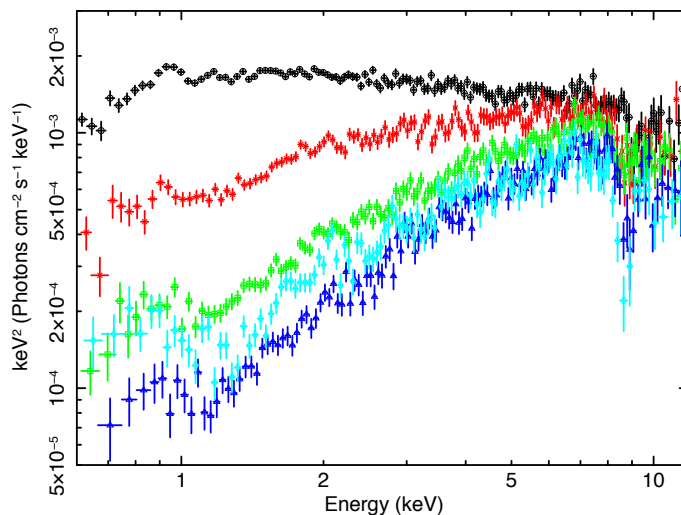


Figure 5.11: *Suzaku* XIS FI spectra from 2007 (black), 2011 (red), 2013a (green), 2013b (blue) and 2013c (cyan), unfolded against $\Gamma = 2$ powerlaw. All spectra are shown in the rest frame of PDS 456.

This cloud could be either be between the continuum source and the wind i.e. the wind also sees the same change in illuminating spectrum as we do, or it could be between the wind and us, in which case the wind sees the original, unabsorbed ionizing continuum. We use *XSTAR* to see if the data can distinguish between these two absorber locations. However, the observed H-like to He-like ratio is mainly determined by hard X-ray illumination, and this is not dramatically changed by the absorber. Hence the current data are not able to locate the additional absorption, and so we assume that it is outside of the wind, and that the wind sees the unobscured continuum.

We note that similar, long lived, external absorption is clearly seen in NGC 5548 (Kaastra et al., 2014), though this is typically much lower ionization with $\log \xi \sim -0.5$ compared to the $\log \xi \sim 2$ required by the 2013 data. This higher ionization is caused by $K\alpha$ (~ 6.4 keV) and $K\beta$ (~ 7.1 keV) absorption lines from moderately ionized Fe ions, which are (marginally) seen in our data (see Fig.5.12).

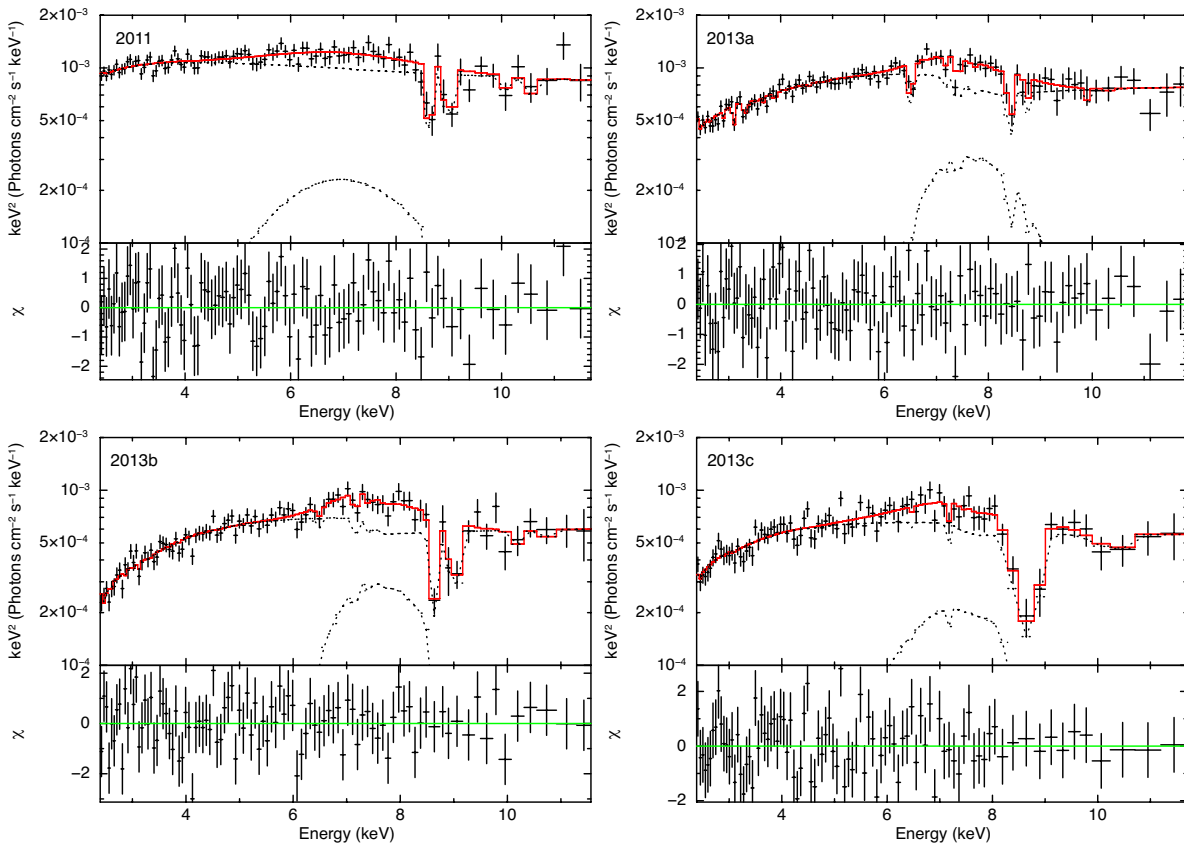


Figure 5.12: *Suzaku* spectra (black points) of PDS 456 fitted with $\text{KABS}^*\text{ZXIPCF}^*(\text{POWERLAW}+\text{GAUSS})$ (red line). From top left, the spectra of 2011, 2013a, 2013b and 2013c are plotted. The continuum spectra are modeled by the power law with the ionized partial covering absorber ZXIPCF. The additional Fe absorption lines and the Fe emission line are modeled with the KABS model and a Gaussian.

Table 5.6: Spectral parameters for all *Suzaku* observations

Model Component	Fit Parameter	Value (90% error)			
		2011	2013a	2013b	2013c
Partial covering absorber	N_{H} (10^{22} cm $^{-2}$)	$1.33^{+7.83}_{-1.03}$	$23.27^{+5.90}_{-7.00}$	$13.67^{+2.80}_{-3.70}$	$10.90^{+2.47}_{-5.62}$
	$\log \xi$	$-0.74(< 2.35)$	$2.35^{+0.16}_{-0.20}$	$2.01^{+0.17}_{-0.70}$	$1.92^{+0.26}_{-0.59}$
	f_{cov}	$0.78(> 0.33)$	$0.87^{+0.12}_{-0.08}$	$1.00(> 0.90)$	$0.89(> 0.84)$
Powerlaw	Γ	2.35 (fix)			
	$F_{2-10 \text{ keV}}$ (10^{-12} erg s $^{-1}$ cm $^{-2}$)	$3.14^{+0.36}_{-0.47}$	$3.27^{+0.43}_{-0.21}$	$2.45^{+0.16}_{-0.19}$	$2.21^{+0.30}_{-0.49}$
	$L_{2-10 \text{ keV}}$ (10^{44} erg s $^{-1}$)	$2.93^{+0.34}_{-0.44}$	$3.06^{+0.40}_{-0.20}$	$2.29^{+0.15}_{-0.18}$	$2.07^{+0.28}_{-0.46}$
Fe XXV He α	v_{out}	$0.248^{+0.007}_{-0.007c}$	$0.224^{+0.035}_{-0.019c}$	$0.250^{+0.009}_{-0.009c}$	$0.223^{+0.014}_{-0.021c}$
	kT (keV)	474 (fix)	474 (fix)	2391 (< 46431)	11503 (< 38843)
	Natom (10^{18})	$2.33^{+7.00}_{-1.47}$	1.01 (< 2.02)	$2.48^{+3.48}_{-1.31}$	2.08 (< 6.42)
	EW (keV)	0.088	0.057	0.135	0.125
Fe XXVI Ly α	v_{out}	tied to Fe XXV			
	kT (keV)	tied to Fe XXV			
	Natom (10^{18})	$6.19^{+24.14}_{-4.25}$	0.59 (< 3.72)	$4.00^{+21.09}_{-2.96}$	11.98 (< 20.41)
	EW (keV)	0.101	0.025	0.126	0.232
Emission	LineE (keV)	$6.35^{+0.57}_{-1.29}$	$7.54^{+0.24}_{-0.22}$	$7.49^{+0.20}_{-0.18}$	$7.08^{+0.47}_{-0.82}$
	σ (keV)	$1.43^{+1.15}_{-0.53}$	$0.87^{+0.27}_{-0.23}$	$0.82^{+0.29}_{-0.20}$	$1.19^{+1.00}_{-0.52}$
	EW (keV)	0.605 (< 1.152)	$0.667^{+0.423}_{-0.218}$	$0.762^{+0.320}_{-0.234}$	$0.734^{+0.757}_{-0.709}$
Fit statistics	χ^2/dof	82.85/90	80.72/95	87.35/88	85.40/82
	Null probability	0.69	0.85	0.50	0.38
	χ^2/dof for 6.5–10.0 keV	19.81/13	12.84/18	13.02/11	2.26/5

5.4.2 Modeling the variability with MONACO

In order to determine the simulation parameters, we compared the 6.5–10.0 keV spectra of the observations between 2011 and 2013 with the model with $L = 1 \times 10^{44}$ erg s $^{-1}$, $v_\infty = 0.3c$, $v_0 = v_{\text{turb}} = 1000$ km s $^{-1}$, $\beta = 1$ and $R_{\text{min}} = 20R_g$. We optimize 3 parameters of the mass outflow rate \dot{M}_{wind} , the inclination angle θ_{incl} and the wind velocity v_∞ . Since v_∞ works like a redshift z for absorption lines, we use z instead of v_∞ . We simulate 4 grids of mass outflow rates, 15, 10, 8 and 3 M_\odot yr $^{-1}$. The geometrical parameter θ_{min} is fixed at 45° because it does not have a large effect on the absorption line features.

As the results, the mass outflow rates are constrained to be $\dot{M}_{\text{wind}} = 7$ (> 4.6), 8 (> 3.6), 7 (> 6.3) and 9 (> 6.5) M_\odot yr $^{-1}$, respectively for 2011, 2013a, 2013b and 2013c observations. The best fit values of redshift are $z = 0.232$, 0.267, 0.218 and 0.238 respectively, which correspond to $v = 0.263_{-0.011}^{+0.017}c$, $0.237c$ ($< 0.260c$), $0.273_{-0.015}^{+0.017}c$ and $0.259_{-0.014}^{+0.025}c$. Here, the obtained values of mass outflow rate are corrected by the terminal velocity because the terminal velocity is assumed to be $0.3c$ in the simulations. According to Eq. 4.8, the mass outflow rate \dot{M}_{wind} is proportional to the density n and the outflow velocity v as $\dot{M}_{\text{wind}} \propto nv$. Since the density determines the ionization structure and the absorption column density, the density in the simulation n_{sim} has to be equal to that in the observed spectra n_{obs} . Thus, the corrected mass outflow rate is $\dot{M}_{\text{obs}} \simeq \dot{M}_{\text{sim}}v_{\text{obs}}/v_{\text{sim}}$. Since all the observed spectra can be reproduced with the mass outflow rate of $\dot{M}_{\text{wind}} = 8 M_\odot$ yr $^{-1}$, the mass outflow rate is fixed at this value in the following analysis.

All the observed spectra in the wide energy range of 2–10 keV are fitted by the model with a fixed mass outflow rate of $\dot{M}_{\text{wind}} = 8 M_\odot$ yr $^{-1}$. The model spectra are simulated for various values of the terminal velocity v_∞ and the outflowing angle θ_{min} , namely $v_\infty = 0.22, 0.24, 0.26, 0.28, 0.30, 0.31, 0.32c$ and $\theta_{\text{min}} = 36, 38, 40, 42, 44, 45, 46^\circ$. In this fitting, the inclination angle θ_{incl} is fixed at 48°, which is the best fit value for the 2007 spectrum.

As the results, both parameters are well constrained, and significantly variable. Fig. 5.13 shows the obtained contours of the outflowing angle and the terminal velocity for all the observations. The contours plotted in red, green and cyan correspond to 68%, 90% and 99% confidence levels, respectively. While the outflowing angles for 2007, 2011 and 2013a are around $\sim 45^\circ$, those for 2013b and 2013c are significantly smaller values around $\sim 40^\circ$. The terminal velocity is also variable from $\sim 0.24c$ to $\sim 0.31c$.

With these best fit parameters, the observed spectra are successfully reproduced by the simulated spectral model as shown in Fig. 5.14. The parameters and fit statistics are listed in Tab. 5.7. When the outflowing angle θ_{min} is close to the inclination angle

θ_{incl} , the line of sight crosses only the fast and less dense materials at the outer part of the wind. Therefore, the model spectra for 2007, 2011 and 2013a show relatively narrow and shallow absorption lines. On the other hands, since the slow and dense materials are also observed for the wind with smaller outflowing angles, the model spectra for 2013b and 2013c show broad and deep absorption lines.

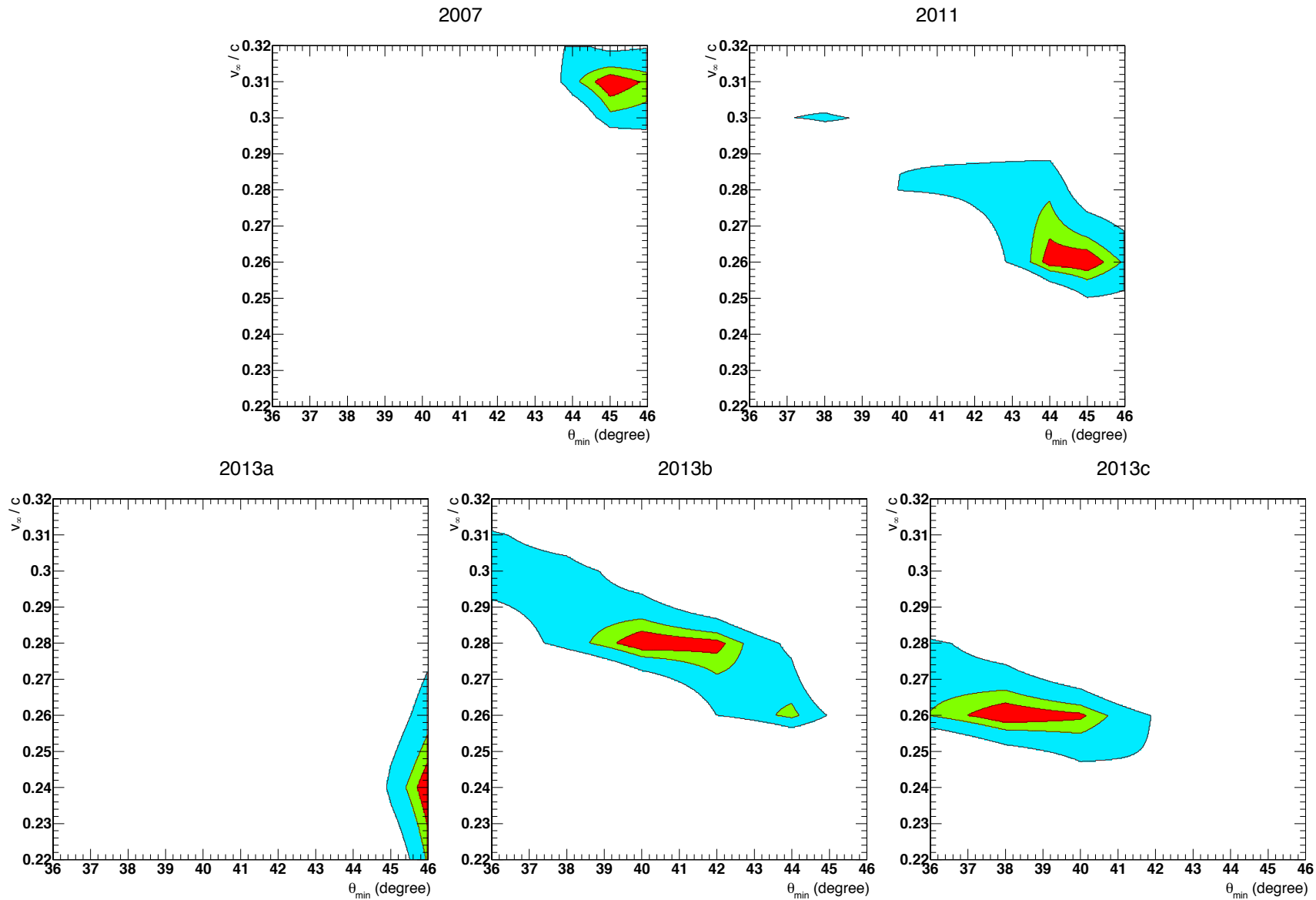


Figure 5.13: Contour plots of the wind outflowing angle θ_{\min} and the terminal velocity v_{∞}/c for all the observations (2007, 2011, 2013a, 2013b and 2013c). The contours shown in red, green and cyan represent confidence levels of 68% ($\approx 1\sigma$), 90% and 99%, respectively.

Table 5.7: MONACO parameters for all *Suzaku* observations

Parameter		Value				
		2007	2011	2013a	2013b	2013c
MONACO wind	$\dot{M}_{\text{wind}} (M_{\odot} \text{ yr}^{-1})$			8 (fix)		
	v_{∞}	$0.31^{+0.004}_{-0.008}c$	$0.26^{+0.017}_{-0.005}c$	$0.24c (< 0.254c)$	$0.28^{+0.007}_{-0.008}c$	$0.26^{+0.007}_{-0.005}c$
	θ_{min}	$45^{\circ} (> 44.2^{\circ})$	$45^{\circ+0.9^{\circ}}_{-1.5^{\circ}}$	$46^{\circ} (> 45.4^{\circ})$	$40^{\circ+2.7^{\circ}}_{-1.4^{\circ}}$	$38^{\circ+2.7^{\circ}}_{-2.0^{\circ}}$
	θ_{incl}			48° (fix)		
Continuum	$N_{\text{H}} (10^{22} \text{ cm}^{-2})$	—	$4.0^{+13.8}_{-1.7}$	$5.6^{+5.1}_{-1.5}$	$5.1^{+1.2}_{-1.1}$	$10.0^{+5.4}_{-5.4}$
	$\log \xi$	—	$-0.46 (< 2.20)$	$-0.55 (< 0.16)$	$-0.85 (< -0.33)$	$0.28 (< 1.66)$
	f_{cov}	—	$0.56^{+0.09}_{-0.14}$	$0.79^{+0.04}_{-0.09}$	$0.91^{+0.07}_{-0.07}$	$0.75^{+0.09}_{-0.04}$
	Γ			2.35 (fix)		
Fit statistics	χ^2/dof	127.9/107	89.7/96	103.2/101	106.6/95	88.5/89
	Null probability	0.08	0.66	0.42	0.20	0.50
	χ^2/dof for 6.5–10.0 keV	23.2/29	24.3/19	22.0/24	21.3/18	3.58/12

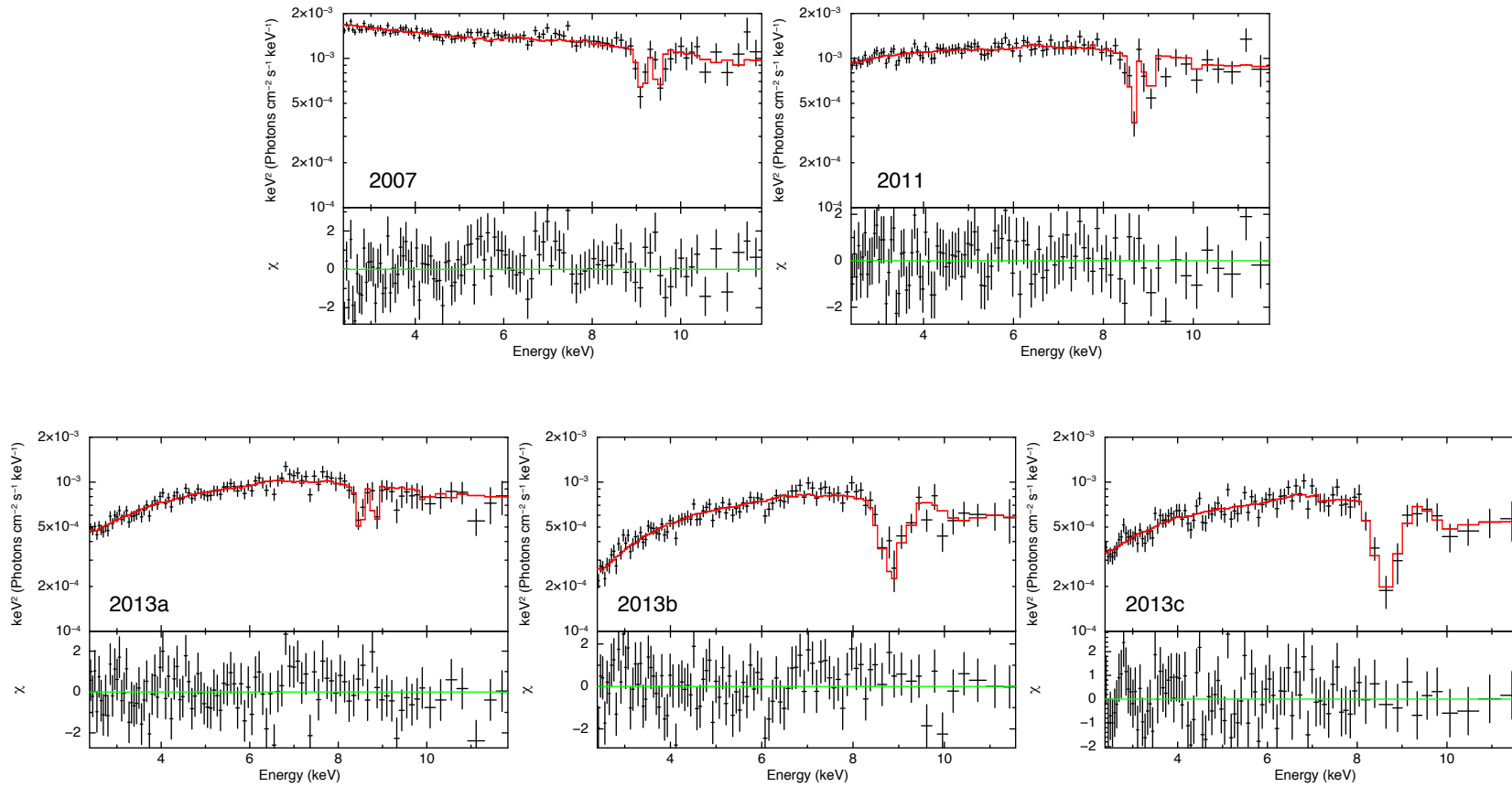


Figure 5.14: The best fit MONACO spectra (red line) with $\dot{M}_{\text{wind}} = 8 M_{\odot} \text{ yr}^{-1}$ and *Suzaku* spectra (black points) for 2011, 2013a, 2013b and 2013c. The lower panel shows the residuals in units of χ . All spectra are shown in the rest frame of PDS 456.

5.5 Summary

We have reproduced the spectra of PDS 456 observed in 2007 by *Suzaku* with our MONACO simulation. The obtained wind parameters are $\theta_{\text{incl}} - \theta_{\text{min}} \sim 2^\circ$, $v_\infty/c \simeq 0.31$ and $\dot{M}_{\text{wind}}/\dot{M}_{\text{Edd}} \sim 0.13$. Also, by comparing the observed emission line structure with our simulations, the inner angle of the wind is found to be $\sim 35^\circ$. If the disk reflection component is dominant in the emission line structure, it is $\sim 55^\circ$.

We applied our model to the other observations of PDS 456 by *Suzaku*, and successfully reproduced all the observations by keeping most of the fundamental parameters constant except for the wind velocity and the relative angle between the line of sight and wind direction. This result indicates that the variability in the wind spectra is explained by the change of the outflowing angle of the wind.

Chapter 6

Analysis of APM 08279+5255

In order to check if the spectral variability of the other AGN can also be explained by the change of the outflowing angle of the wind, we analyze APM 08279+5255 in this chapter. APM 08279+5255 is a gravitationally lensed, high redshift ($z = 3.91$) quasar, so that blueshifted H/He-like Fe lines are seen at ~ 2 keV. At such an energy, the sensitivities of current instruments are better than those obtained at the energy where absorption lines of UFOs at low redshift are observed (~ 8 keV). This enables us to detect the UFO signatures even in the relatively faint quasar APM 08279+5255, whose X-ray flux is roughly one order of magnitude lower than PDS 456.

6.1 Observational data

APM 08279+5255 has been observed by *Chandra*, *XMM-Newton* and *Suzaku*. Around 2 keV, *Suzaku* response is uncertain, and its sensitivity is worse than *XMM-Newton*. Therefore, we use the *XMM-Newton* data. *XMM-Newton* has observed APM 08279+5255 4 times between 2001 and 2007, which are listed in Tab. 6.1.

We processed EPIC-pn and -MOS data and removed dead and hot pixels by using SAS

Table 6.1: *XMM-Newton* observations of APM 08279+5255

Obs ID	Start Date	Net exposure (ks)
		MOS1/MOS2/PN
0092800101	2001-10-30	16.7/16.7/12.3
0092800201	2002-04-28	76.4/77.2/63.2
0502220201	2007-10-06	68.0/68.6/39.3
0502220301	2007-10-22	75.8/75.8/57.9

tasks `EPPROC` and `EMPROC` (SAS v.13.5.0) respectively. Time intervals when background rates of `PATTERN = 0` events at energy > 10 keV are higher than $0.35 \text{ counts s}^{-1}$ for MOS and $0.4 \text{ counts s}^{-1}$ for pn camera were removed. Only events with `PATTERN` ≤ 12 for MOS and `PATTERN` ≤ 4 for pn were considered in the spectral analysis. The total net exposure times are listed in Tab. 6.1. Spectra were extracted from circular regions of $64''$ diameter, while background spectra were extracted from circular regions of the same diameter for pn and annular regions from $100''$ to $300''$ diameter for MOS in the same chip as the source regions. We generated the corresponding response matrix (RMF) and auxiliary response (ARF) files by utilizing `RMFGEN` and `ARFGEN`. The spectra were then grouped by using `SPECGROUP` to obtain minimum 40 counts in each bin.

In order to see the absorption features reported by Hasinger, Schartel & Komossa (2002) and Chartas et al. (2009), we fit the pn spectra of each observation with a simple power law model multiplied by Galactic absorption and additional absorption in APM 08279+5255 rest frame. As shown in Fig. 6.1, in all spectra, an absorption line at ~ 8 keV and edge-like feature above $\sim 8\text{--}9$ keV can be seen. The parameters for the continuum spectra are not variable, with photon index of $\Gamma = 1.92 \pm 0.04$, 1.92 ± 0.02 , 2.08 ± 0.02 , 2.16 ± 0.02 , and absorption column density of $N_{\text{H}} = 4.8 \pm 0.5$, 5.1 ± 0.2 , 4.7 ± 0.2 , $5.3 \pm 0.2 \text{ cm}^{-2}$. The fit statistics are not good with $\chi^2_{\nu} = 1.3\text{--}1.5$, indicating the clear existence of the absorption structures of UFOs. Below, we use the spectra observed in 2002 because of their long exposure.

6.2 Comparison of the Monte Carlo simulations and the 2002 spectra

Before studying the spectral variability of APM 08279+5255, we optimize the model parameters by comparing the Monte Carlo simulations and the 2002 spectra, whose exposure time is the longest in the *XMM-Newton* data of this source.

6.2.1 Parameter choice

The black hole mass and the luminosity of APM 08279+5255 have large uncertainties due to a magnification factor μ of gravitational lensing. Riechers et al. (2009) estimated the black hole mass as $M_{\text{BH}} = 9.0 \times 10^{10} \mu^{-1} M_{\odot}$ from the spectrum by Irwin et al. (1998) by using a relation between the FWHM of C IV $\lambda 1549$, the rest frame UV continuum luminosity at 1350\AA and the black hole mass (Vestergaard & Peterson, 2006). However, compared with the bolometric luminosity $L_{\text{bol}} = 2.7 \times 10^{49} \mu^{-1} \text{ erg s}^{-1}$ (Irwin et al.,

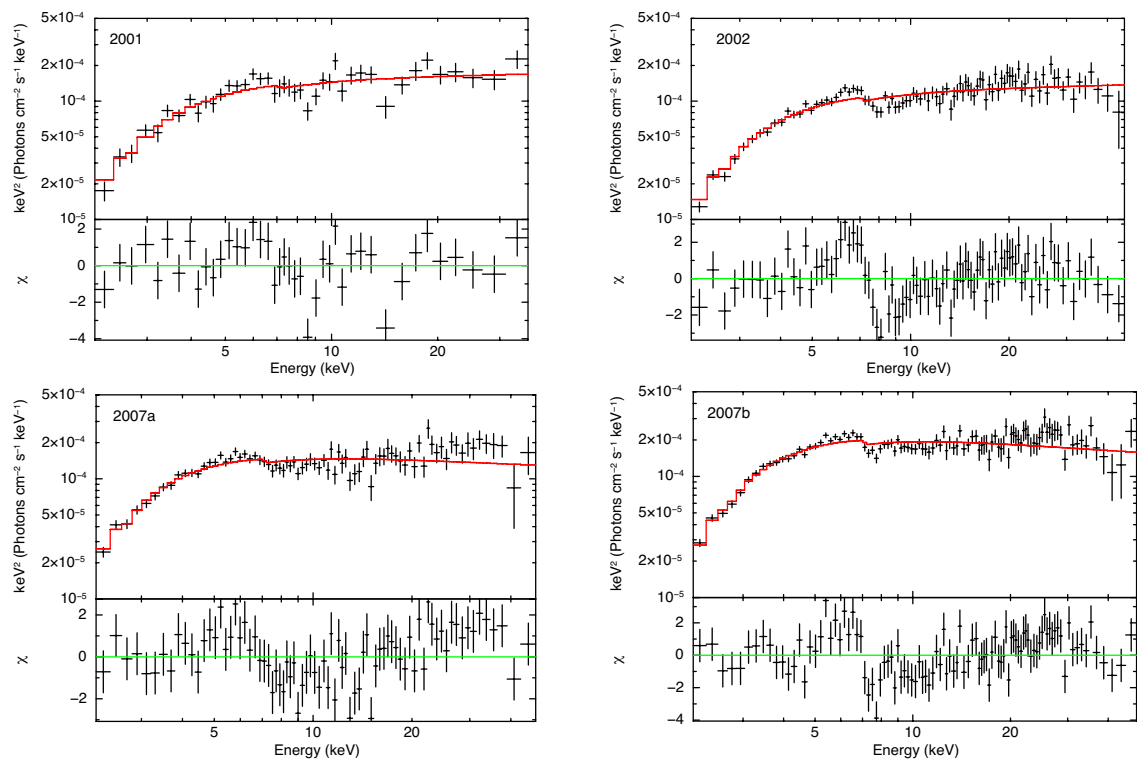


Figure 6.1: *XMM-Newton* spectra (black points) fitted with an absorbed power law model (red lines). The lower panels show the residuals in units of χ .

1998; Riechers et al., 2009), the Eddington ratio would exceed unity, $L_{\text{bol}}/L_{\text{Edd}} \simeq 2$. On the other hand, Saez, Chartas & Brandt (2009); Chartas et al. (2009); Saez & Chartas (2011) use a different value estimated by a relation between Eddington ratio $L_{\text{bol}}/L_{\text{Edd}}$ and X-ray photon index Γ (Wang, Watarai & Mineshige, 2004; Shemmer et al., 2006, 2008). The X-ray photon index of this source ~ 2.0 indicates a moderate Eddington ratio $L_{\text{bol}}/L_{\text{Edd}} \simeq 0.2\text{--}0.3$, which leads to the black hole mass of $M_{\text{BH}} \sim 10^{12}\mu^{-1} M_{\odot}$. In this thesis, we use this value as the black hole mass because it does not require super Eddington accretion.

The value of magnification factor is still very controversial. Although some papers report strong magnification with $\mu \sim 100$ (Egami et al., 2000; Weiß et al., 2007; Krips et al., 2007), others claim smaller values $\mu \sim 2\text{--}10$ (Lewis et al., 2002; Solomon & Vanden Bout, 2005; Riechers et al., 2009). However, the value of the magnification factor is not so important because our simulations do not depend on it. If we write the mass outflow rate \dot{M}_{wind} in units of Eddington accretion rate, the black hole mass M_{BH} and the luminosity L are proportional to the magnification factor μ . Therefore, two parameters controlling the observed spectra, namely $\xi = L/nR^2 \propto L/\dot{M}_{\text{wind}}$ and $N_{\text{H}} = nR \propto \dot{M}_{\text{wind}}/R$, are independent from μ . Here, we assume the geometry is fixed and the equation of mass conservation $\dot{M}_{\text{wind}} \propto nR^2$. In the following sections, we adopt the stronger magnification factor $\mu = 100$ to simulate spectra, but the results do not change if we use different magnification.

In order to determine the other MONACO parameters such as the terminal velocity and the mass outflow rate, we fit the APM 08279+5255 spectra by the MONACO model constructed for PDS 456. Since the APM 08279+5255 spectra do not show simple absorption lines but a complex feature seemingly composed of the absorption lines and edge, we do not use the simple models like Gaussian absorption lines but use the MONACO spectra. Although many parameters such as the black hole mass, the intrinsic source spectrum and its luminosity are not appropriate for this source, this exercise is very useful to roughly estimate the terminal velocity, mass outflow rate and inclination angle. As for the results, the model with lower mass outflow rate $\dot{M}_{\text{wind}} = 3 M_{\odot} \text{ yr}^{-1}$ gives a good fit with $\chi^2_{\nu} = 195.8/208$, while the other values of \dot{M}_{wind} give worse fit statistics of $\chi^2 = 244.5$ and 271.0 for $\dot{M}_{\text{wind}} = 1$ and 8 , respectively. Here, in all models, the terminal velocity is fixed at $v_{\infty} = 0.3c$. The best fit value of inclination angle is higher than that for PDS 456 because APM 08279+5255 spectra show broader absorption lines and a strong edge structure. This is because we observe materials with a variety of velocities in the wind at a higher inclination. Therefore, we use $\dot{M}_{\text{wind}}/\dot{M}_{\text{Edd}} = 0.04$ and $v_{\infty} = 0.3c$ as fiducial parameters. Fig. 6.2 shows a best fit MONACO model for PDS 456.

The absorption column density of each ion depends on the ionization structure. The

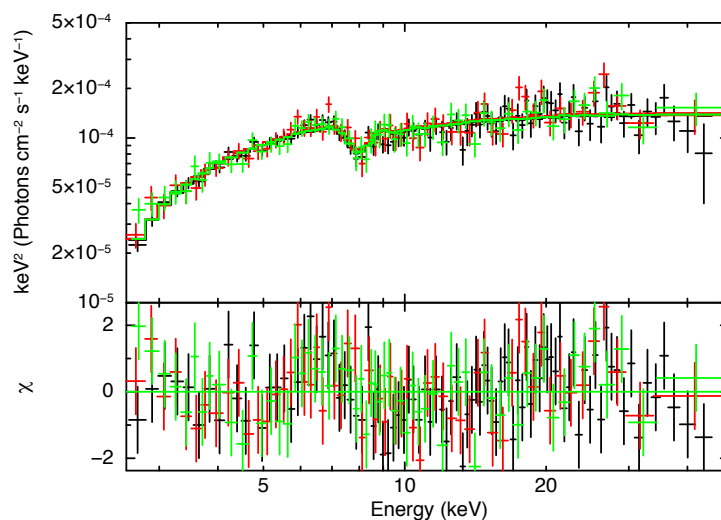


Figure 6.2: *XMM-Newton* spectra of APM 08279+5255 fitted with the MONACO model used for PDS 456. The spectra obtained by the MOS detectors and their models are plotted in red and green, respectively. The data points and the line shown in black are the data and model for the pn camera. The mass outflow rate is lower ($\dot{M}_{\text{wind}} = 3 M_{\odot} \text{ yr}^{-1}$) and the inclination angle is higher ($\theta_{\text{incl}} = 68.9^{\circ}$) compared with the best fit values for PDS 456.

continuum spectra can be reproduced by a power law with a flat photon index $\Gamma \simeq 2.0$ and a magnified luminosity $L \simeq 5 \times 10^{46} \text{ erg s}^{-1}$, absorbed by a neutral material with column density $N_{\text{H}} \simeq 5 \times 10^{22} \text{ cm}^{-2}$. Because the spectra of this source are hard compared with PDS 456 ($\Gamma = 2.3\text{--}2.4$), the wind is more ionized. Therefore, we need a larger mass outflow rate for APM 08279+5255. Actually, with $\dot{M}_{\text{wind}}/\dot{M}_{\text{Edd}} = 0.04$, i.e. $\dot{M}_{\text{wind}} = 0.15 M_{\odot} \text{ yr}^{-1}$, H- and He-like Fe ions are only $\sim 5\%$ of total Fe atoms. From above, we adopt $\dot{M}_{\text{wind}} = 50 M_{\odot} \text{ yr}^{-1}$ instead of $15 M_{\odot} \text{ yr}^{-1}$. As a summary of the above, all the fiducial parameters are listed in Tab. 6.2.

Table 6.2: Parameters for APM 08279+5255

Parameter	Value
M_{BH}	$10^{10} M_{\odot}$
L_{2-10}	$5 \times 10^{44} \text{ erg s}^{-1}$
Γ	2.0
v_{∞}	$0.3c$
R_{min}	$20R_{\text{g}}$
\dot{M}_{wind}	$50 M_{\odot} \text{ yr}^{-1}$

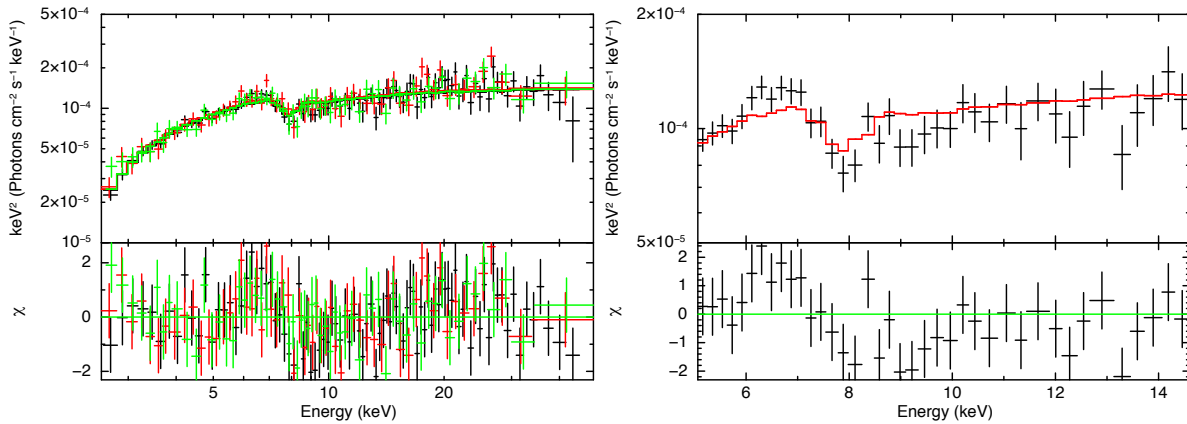


Figure 6.3: Spectra and best fit model with $v_\infty = 0.3c$, $\dot{M}_{\text{wind}} = 50 M_\odot \text{ yr}^{-1}$. *Left*: pn (black), MOS1 (red) and MOS2 (green) spectra and model. *Right*: pn zoom-in spectrum and model.

6.2.2 Parameter constraints of the 2002 spectrum

We compare the observed spectra with the MONACO spectrum with the fiducial parameter set. This gives a good fit with $\chi_\nu^2 = 208.6/208$, and $\theta_{\text{incl}} = 71.0_{-3.5}^{+2.6^\circ}$. However, as shown in Fig. 6.3, both the emission line and the absorption features are smaller in the model spectra. To improve the spectral model, there are two different approaches such as increasing the mass out flow rate or the terminal velocity. The former is easy to understand because the more massive outflow makes more absorption and emissions. Increasing the terminal velocity makes the inclination angle higher in order to fit the line center of the absorption line to the observed spectra. Then, since we observe the slower and denser materials at higher inclination angle, the absorption features and emission lines get larger.

We run the MONACO simulations with $v_\infty = 0.3c, 0.4c, 0.5c, 0.6c$ and $\dot{M}_{\text{wind}} = 50, 70, 100 M_\odot \text{ yr}^{-1}$. The inner radii of the wind are changed with the values of v_∞ . By keeping the relation of $v_{\text{esc}}(R_{\text{min}}) \sim v_\infty$ roughly, we adopt $R_{\text{min}} = 20, 10, 8$ and $6R_g$ for $v_\infty = 0.3c, 0.4c, 0.5c$ and $0.6c$, respectively. As results, we obtain the best fit statistics of $\chi_\nu^2 = 175.7/208$ with $v_\infty = 0.3c$ and $\dot{M}_{\text{wind}} = 70 M_\odot \text{ yr}^{-1}$. At the best fit parameters, the inclination angle is $72.8_{-1.5}^{+1.2^\circ}$. The best fit spectra and model are shown in Fig. 6.4, and the fit statistics for the other parameter sets can be seen in the left panel of Fig. 6.5. The absorption features are well reproduced by our MONACO model, but there are small residuals like reflected components such as the emission line at $\sim 6.4\text{--}7.0$ keV and the Compton reflection hump at ~ 20 keV.

In order to check if the reflection-like feature seen in the residuals is the disk reflection

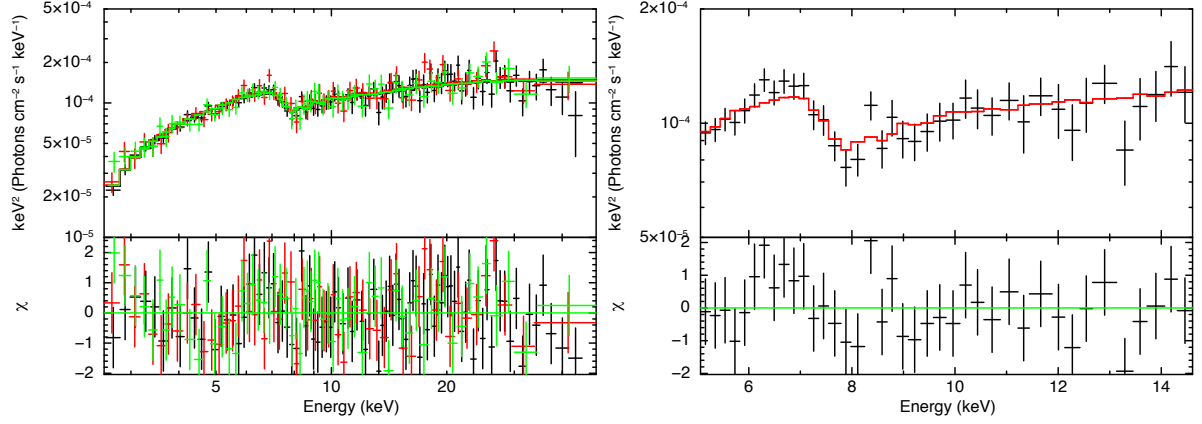


Figure 6.4: Spectra and best fit model with $v_\infty = 0.4c$, $\dot{M}_{\text{wind}} = 70 M_\odot \text{ yr}^{-1}$. *Left*: pn (black), MOS1 (red) and MOS2 (green) spectra and model. *Right*: pn zoom-in spectrum and model.

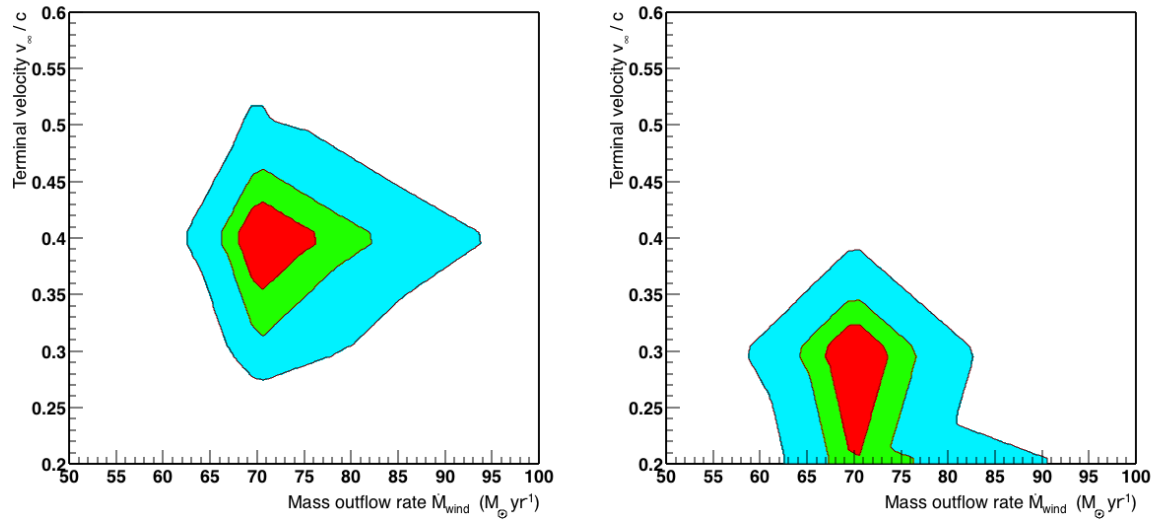


Figure 6.5: Contour plots of the terminal velocity and the mass outflow rate, fitted with powerlaw model multiplied by the MONACO spectra (left), and the model with an additional reflection component REFLIONX (right). The region filled with red represents the 1- σ confidence level, i.e. the fit statistics are smaller than $\chi_{\text{min}}^2 + 2.3$. The green and cyan regions correspond to 90% and 99% confidence levels respectively.

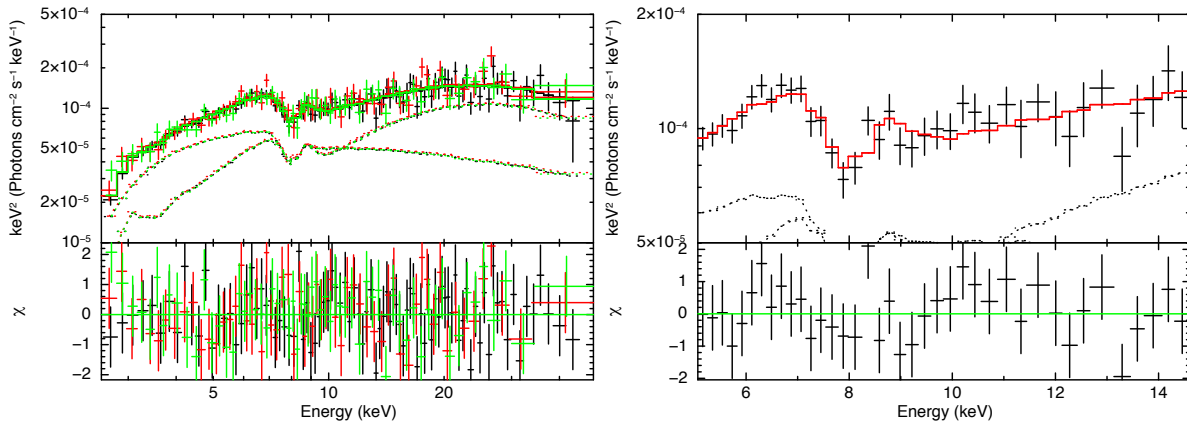


Figure 6.6: Spectra and best fit model with $v_\infty = 0.3c$, $\dot{M}_{\text{wind}} = 70 M_\odot \text{ yr}^{-1}$. The disk reflection component REFLIONX is added. *Left*: pn (black), MOS1 (red) and MOS2 (green) spectra and model. *Right*: pn zoom-in spectrum and model.

component, we add an ionized reflection model REFLIONX convolved by the relativistic blurring model KDBLUR. The MONACO model is multiplied both by reflection and power-law components. The outer and inner radius of KDBLUR are fixed at $6R_g$ and R_{min} , and emissivity is fixed at 3. As shown in the right panel in Fig. 6.5, we obtain the best fit with a slightly slower velocity but same mass loss rate, $v_\infty = 0.3c$ and $\dot{M}_{\text{wind}} = 70 M_\odot \text{ yr}^{-1}$. This is because the broadened emission line in the reflection component can fill the red side of the absorption line, so that the absorption line needs more red (slower) components. The obtained fit statistics of $\chi_\nu^2 = 161.6/206$ are significantly better than the model without the reflection component. Fig. 6.6 shows the best fit model. As shown, the reflection component is dominant above 10 keV, and the photon index get steeper to $\Gamma = 2.49_{-0.19}^{+0.15}$. The inclination angle is not affected by the disk reflection, and is $\theta_{\text{incl}} = 70.7_{-2.2}^{+1.4}^\circ$.

Even if the disk reflection component is dominant, we can reproduce the absorption feature in the observed spectra by our MONACO model with almost the same parameter sets. Therefore, we can conclude that the wind of APM 08279+5255 observed in 2002 has a terminal velocity of $v_\infty \sim 0.2\text{--}0.45c$, a mass outflow rate of $\dot{M}_{\text{wind}} \sim 70 M_\odot \text{ yr}^{-1}$, which corresponds to $\dot{M}_{\text{wind}}/\dot{M}_{\text{Edd}} \sim 0.18$ in Eddington units (efficiency η is assumed to be 0.06). These values are almost the same as the parameters of the PDS 456 wind, where the terminal velocity is $v_\infty \sim 0.2\text{--}0.3c$ and the mass outflow rate is $\dot{M}_{\text{wind}}/\dot{M}_{\text{Edd}} \sim 0.09\text{--}0.13$. The only different parameter is the inclination angle, which is $\sim 70^\circ$ for APM 08279+5255 and $\sim 50^\circ$ for PDS 456.

Table 6.3: Best fit parameters of the MONACO model for all the *XMM-Newton* observations.

Parameter		Value			
		2001	2002	2007a	2007b
MONACO wind	\dot{M}_{wind} ($M_{\odot} \text{ yr}^{-1}$)	70			
	v_{∞}	$0.4c$			
	θ_{incl}	$71.7^{+3.9}_{-2.5}$	$72.7^{+1.2}_{-1.5}$	$79.8^{+0.6}_{-1.1}$	$76.4^{+0.9}_{-0.9}$
Continuum spectra	N_{H} (cm^{-2})	$4.01^{+1.29}_{-1.23}$	$5.51^{+0.63}_{-0.61}$	$4.39^{+0.48}_{-0.38}$	$5.09^{+0.43}_{-0.41}$
	Γ	$1.90^{+0.08}_{-0.08}$	$1.93^{+0.02}_{-0.04}$	$2.04^{+0.03}_{-0.03}$	$2.12^{+0.02}_{-0.03}$
Fit statistics	χ^2/dof	95.1/81	175.7/208	210.5/202	261.5/251
	Null probability	0.14	0.95	0.33	0.31

6.3 Study of the spectral variability

We try to explain the spectral variability of APM 08279+5255 by the change of the outflowing angle of the wind. In the case of APM 08279+5255, we can observe the spectra up to high energy ~ 50 keV, where intrinsic X-ray radiation is dominant if the reflection hump is small. This means the intrinsic spectral index is accessible even in the absorbed spectra, so that the photon index is not fixed in the fitting.

The best fit models for all the spectra are shown in Fig. 6.7, and the parameters are listed in Tab. 6.3. The models without reflection are applied here. For all observations, the mass outflow rate \dot{M}_{wind} and the terminal velocity v_{∞} are fixed at the best fit values of the 2002 observation, so that only the inclination angle is a free parameter of the wind model. As shown in the figure, all the observations are successfully reproduced by our MONACO model. The inclination angle varies from $\sim 70^\circ$ to $\sim 80^\circ$ depending on the observations.

Physically, this result can be interpreted as a variation of the outflowing angle of the wind. In the case of PDS 456, the relative angle between the wind and our line of sight is found to vary $\sim 6^\circ$. Therefore, the variation of the wind angle of APM 08279+5255 is similar to PDS 456 although the spectral change is not quite large in this source. When observed with a low inclination, the spectra are more sensitive to the variation of the wind angle, so that the APM 08279+5255 spectra do not look very different between observations.

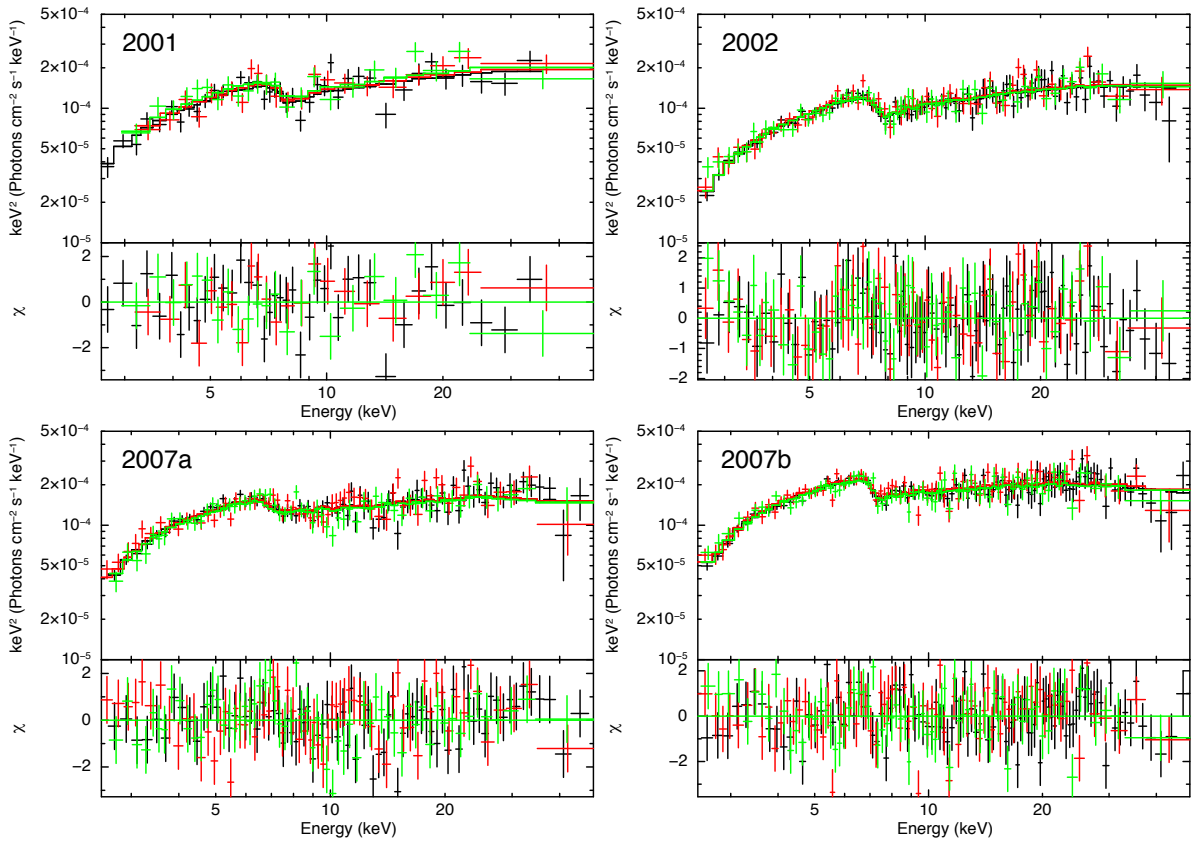


Figure 6.7: Spectra and best fit model with $v_\infty = 0.4c$, $\dot{M}_{\text{wind}} = 70 M_\odot \text{ yr}^{-1}$ for all the *XMM-Newton* observations (2001, 2002, 2007a and 2007b). The spectra and models of pn, MOS1 and MOS2 are plotted in black, red and green, respectively. The lower panels show the residuals in units of χ .

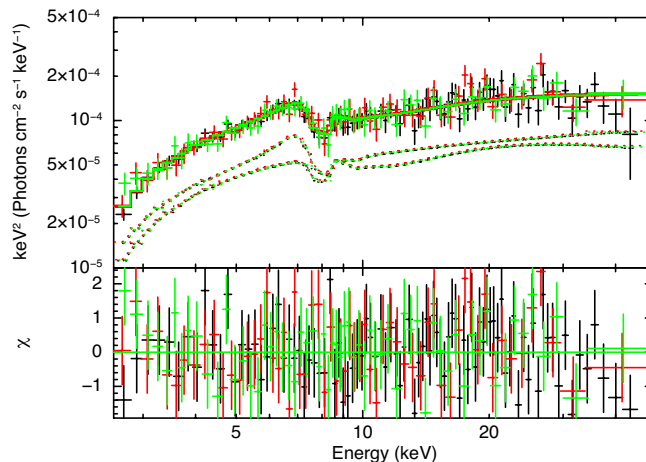


Figure 6.8: *XMM-Newton* spectra of APM 08279+5255 observed in 2002 and the best fit model. The model is composed of the absorbed power law and ionized reflection multiplied by the velocity convolved absorption lines and edges. The spectra and models of pn, MOS1 and MOS2 are plotted in black, red and green, respectively.

6.4 Searching of a large parameter space with a phenomenological model

In the previous section, the observed spectra are successfully reproduced by our MONACO simulation models. However, different from PDS 456, APM 08279+5255 shows very broad absorption feature, so that it is possible to reproduce the spectra by changing the viewing angle even with a larger velocity. Therefore, one question arises: is there any better solution for APM 08279+5255 spectra in the wide parameter space? In this section, we answer this question by introducing a new model for searching a wide range of parameter space.

We fit the spectra of APM 08279+5255 with the quick phenomenological model explained in section 4.6. For the continuum spectra, we used a power law model and the ionized reflection model REFLIONX. The spectra and model are shown in Fig. 6.8, and the parameters are listed in Tab. 6.4.

Then we interpret the spectral parameters into the physical parameters. By using Fig. 4.12, we can convert the 90% confidence contour of δ_0 - $\Delta\delta$ plane to that of v_∞ - $\Delta\theta$ plane. Here, $\Delta\theta$ is the relative angle between the line of sight θ_{incl} and the outflowing angle θ_{min} , namely $\Delta\theta \equiv \theta_{\text{incl}} - \theta_{\text{min}}$. Fig. 6.9 shows a contour plot of δ_0 and $\Delta\delta$. With $\Delta\delta < 0.25$, the parameters are independent of each other. Therefore, we plot the 90% confidence interval for each parameter on the left panel of Fig. 6.10. The confidence interval of δ_0 corresponds the narrow region distributing from top right to bottom left, and $\Delta\delta$ sets the

Table 6.4: Fitting result of the convolved absorption model

Model Component	Fit Parameter	Value (90% error)
Continuum absorption	N_{H}	$5.29^{+0.61}_{-0.57}$
Powerlaw	Γ	$1.80^{+0.10}_{-0.13}$
	$F_{2-10 \text{ keV}}$ ($10^{-13} \text{ erg s}^{-1} \text{ cm}^{-2}$)	3.1
	$L_{2-10 \text{ keV}}^1$ ($10^{44} \text{ erg s}^{-1}$)	4.7
Convolved absorption	δ_0	$1.186^{+0.027}_{-0.042}$
	$\Delta\delta$	0.140(< 0.223)
	$N(\text{Fe XXV})+N(\text{Fe XXVI})$ (10^{18} cm^{-2})	$3.19^{+2.46}_{-1.00}$
	$N(\text{Fe XXVI})/N(\text{Fe XXV})$	0.3(< 27.9)
Reflection	ξ	2700^{+1800}_{-1400}
Fit statistics	χ^2/dof	164.20/203
	Null probability	0.98

¹ The magnification factor $\mu = 100$ is assumed.

upper limit around $v_{\infty}/c \sim 0.6$. The red region in this figure is the confidence contour of v_{∞} and $\Delta\theta$, which corresponds to $v_{\infty} = 0.38^{+0.31}_{-0.25}$ and $\Delta\theta = 27.5(< 37.3)$.

As verification of our assumption that δ_0 and $\Delta\delta$ are independent, we directly convert the contour shown in Fig. 6.9. The results are shown in the right panel of Fig. 6.10. The red, green and blue regions represent 68%, 90% and 99% confidence levels, respectively. The green contour covers $v_{\infty} = 0.37^{+0.39}_{-0.22}$ and $\Delta\theta = 27.2(< 37.3)$, which is the almost same region as the left panel. The local minimum at $(\delta_0, \Delta\delta) = (1.12, 0.35)$ does not have a corresponding point in v_{∞} - $\Delta\theta$ plane. In other words, this local minimum is an unphysical solution within our assumed geometry. Thus, hereafter, we adopt the results of the former method to estimate the v_{∞} - $\Delta\theta$ contour by assuming parameter independence.

We run XSTAR to obtain the relation between \dot{M}_{wind} and the column density of Fe ions. Fig. 6.11 shows the distributions of $N(\text{Fe XXV} + \text{Fe XXVI})$ and $N(\text{Fe XXVI})/N(\text{Fe XXV})$ with $\dot{M}_{\text{wind}} = 40 M_{\odot} \text{ yr}^{-1}$ in the 90% confidence interval of v_{∞} and $\Delta\theta$. By using the obtained confidence range of $N(\text{Fe XXV} + \text{Fe XXVI})$ and $N(\text{Fe XXVI})/N(\text{Fe XXV})$, we can constrain the physical parameters. For example of Fig. 6.11, from the confidence interval of $N(\text{Fe XXV} + \text{Fe XXVI})$ of $2.19\text{--}5.65 \times 10^{18} \text{ cm}^{-2}$, v_{∞} and $\Delta\theta$ is limited within the certain region roughly corresponding to the green region. $N(\text{Fe XXVI})/N(\text{Fe XXV})$ also constrain these physical parameters. By adopting this procedure for a various values of the mass

6.4. Searching of a large parameter space with a phenomenological model 103

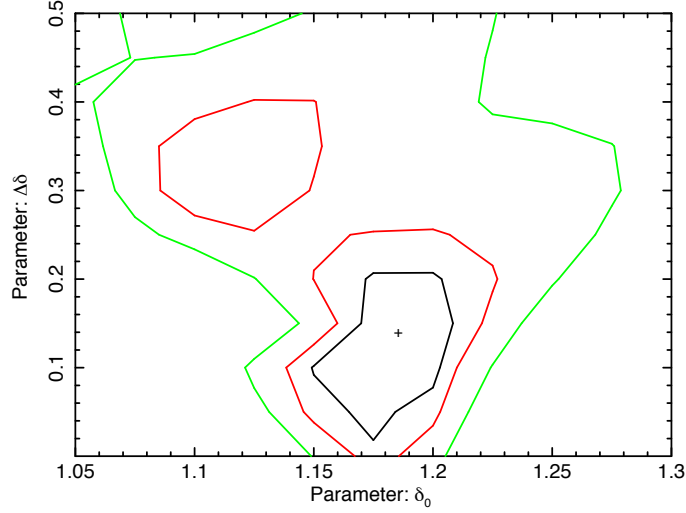


Figure 6.9: A contour plot of δ_0 and $\Delta\delta$ for the 2002 spectra. Each line corresponds to 1- σ (black), 90% (red) and 99% (green) significance levels.

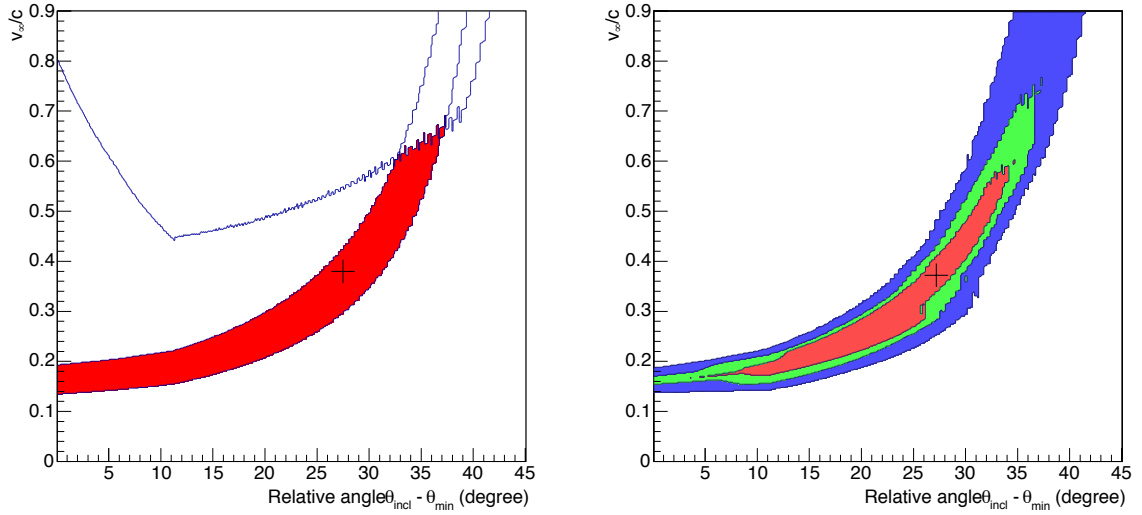


Figure 6.10: Contour plot of the relative angle $\Delta\theta$ ($\theta_{\text{incl}} - \theta_{\text{min}}$) and the terminal velocity v_∞ . The best fit value is shown by a black cross. *Left*: The red region shows a calculated from 90% error for each parameter (δ_0 and $\Delta\delta$). In this plot, correlation between δ_0 and $\Delta\delta$ is not considered. *Right*: The red, green and blue contours represent 1- σ , 90% and 99% confidence levels, respectively. The regions correspond to those shown in Fig. 6.9.

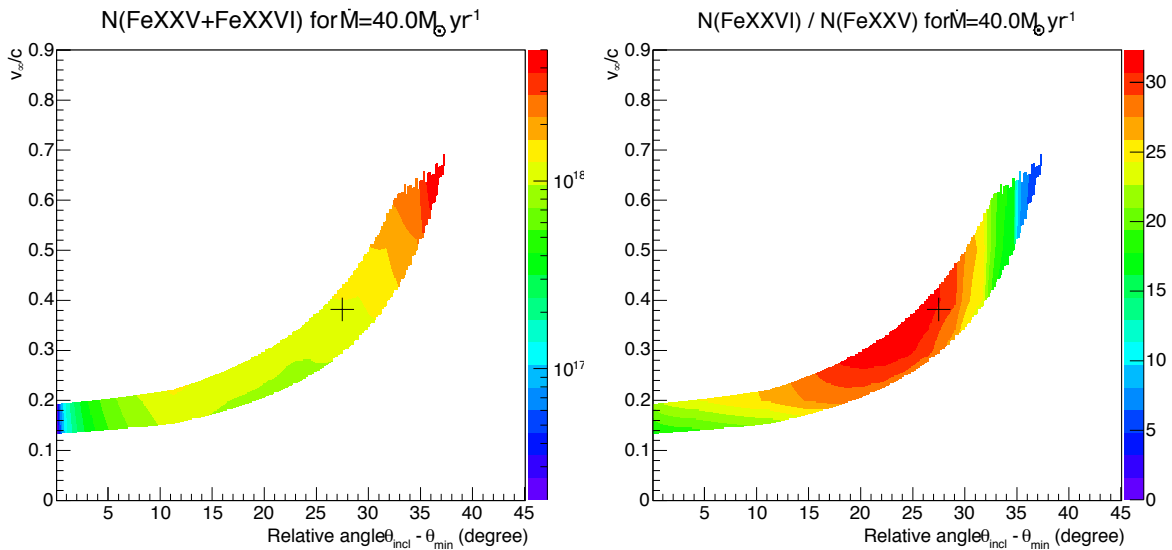


Figure 6.11: The distribution of the column density (left) and the ratio (right) of the H/He-like Fe ions with $\dot{M}_{\text{wind}} = 40 M_{\odot} \text{ yr}^{-1}$ in the 90% confidence interval of v_{∞} and $\Delta\theta$.

outflow rate \dot{M}_{wind} , we can obtain an overlapping region of confidence intervals of four spectral parameters in a v_{∞} - $\Delta\theta$ - \dot{M}_{wind} solid.

The results are shown in Fig. 6.12. The red, yellow, green and blue regions represent the 38% ($\sim 0.5\sigma$), 68% ($\sim 1\sigma$), 90% and 99% confidence levels, respectively. If compared with Fig. 6.5, the contour is located at a similar parameter space. Therefore, in this quick model, the physical parameters are estimated correctly.

Here, the most important conclusion in this section is that the solution for the wind in APM 08279+5255 is confirmed to be the only one obtained in the previous section ($\Delta\theta \sim 25^{\circ}$, $v_{\infty}/c = 0.2\text{--}0.5$ and $\dot{M}_{\text{wind}} \sim 70 M_{\odot} \text{ yr}^{-1}$). Although there is the other local minimum in the spectral parameter space, our wind model has no physical solution there. As such, this model is useful for searching a wide range of parameter space.

Also, since this model quickly provides us a good estimate of the solution, it can be used to determine the parameters for MONACO simulations. In the next chapter, we use this model for such proposes.

6.5 Summary of the analysis of APM 08279+5255

By using our MONACO simulations, the wind in APM 08279+5255 observed in 2002 by *XMM-Newton* are found to be similar to the wind in PDS 456 except for our line of sight. The obtained parameters for APM 08279+5255 are $\Delta\theta \sim 25^{\circ}$, $v_{\infty}/c = 0.2\text{--}0.5$

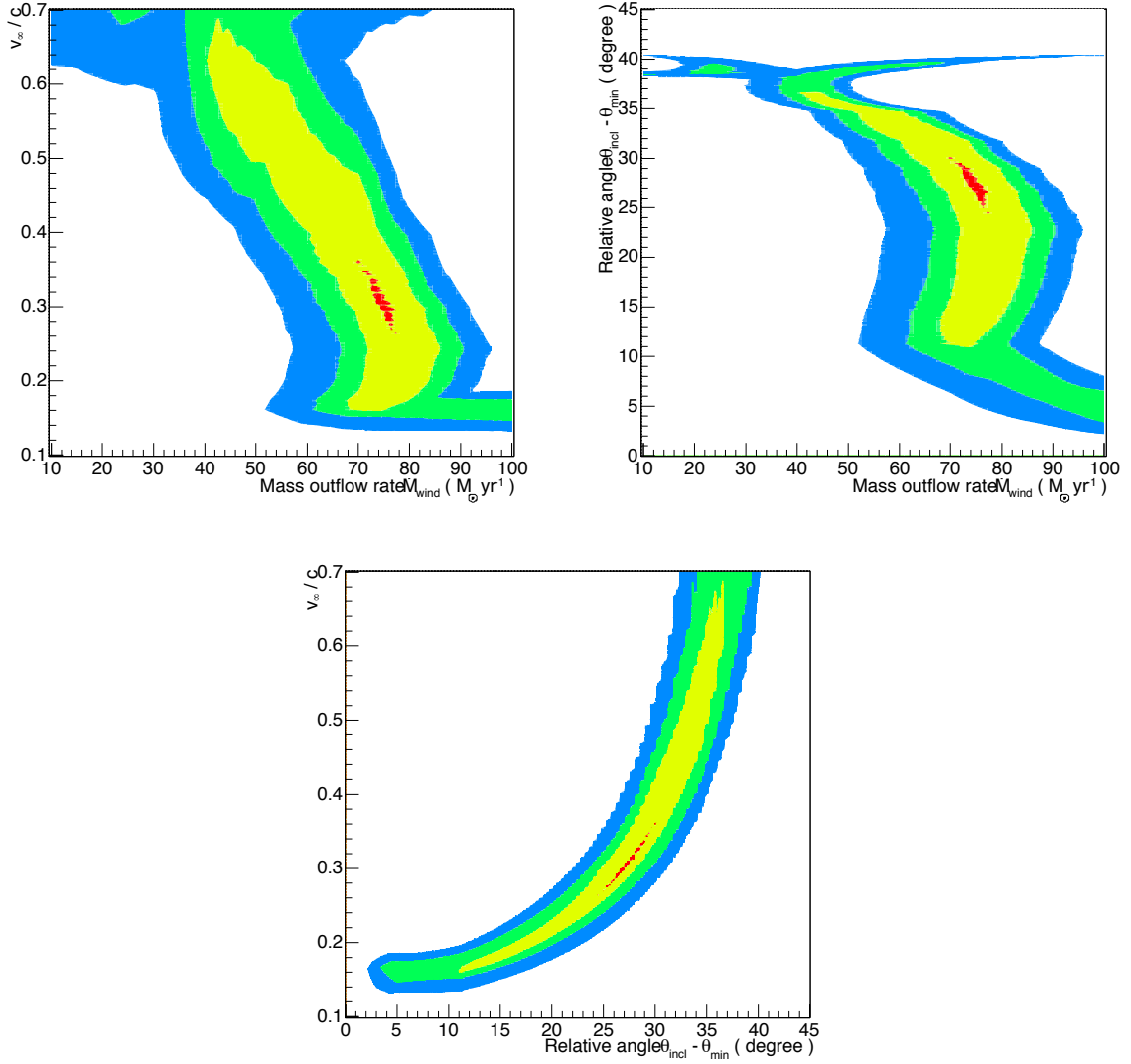


Figure 6.12: A projection of the 3-dimensional contour plot of the relative angle $\Delta\theta$ ($\theta_{\text{incl}} - \theta_{\text{min}}$), the terminal velocity v_∞ and the mass outflow rate \dot{M}_{wind} . The red, yellow, green and blue regions correspond to the 38% ($\sim 0.5\sigma$), 68% ($\sim 1\sigma$), 90% and 99% confidence intervals.

and $\dot{M}_{\text{wind}}/\dot{M}_{\text{Edd}} \sim 0.18$.

Also, we have successfully reproduced all the spectra observed by *XMM-Newton* by changing only inclination angle, which is interpreted as the outflowing angle of the wind. Again, this result is the same as PDS 456. The variation of the angle is $\sim 8^\circ$, of the same order as PDS 456 ($\sim 8^\circ$).

In order to search a large parameter space, we introduced a new simple model. It gave us almost same results obtained by the MONACO simulations except for the underestimated mass outflow rate. By searching all over the parameter space, it is confirmed that there is no other local minimum or solution for the wind in APM 08279+5255.

All in all, the wind in APM 08279+5255 is similar to PDS 456. This strongly indicates that both of the winds are driven by the same mechanism.

Chapter 7

Discussion on the accretion disk winds in high mass AGN

In chapter 5 and 6, we have analyzed high mass AGN showing strong UFO features. We revealed the physical parameters of the winds and their variation depending on the observational epochs. In this section, we discuss their implications for the wind structure and launching mechanisms.

7.1 Instability of the wind geometry

The most remarkable result obtained in the previous two chapters is that all the observed spectra in different epochs are successfully reproduced by changing the relative angle between the wind and the line of sight. This result is interpreted that the outflowing angles of the wind are different for the different epoch, and this geometrical change makes us observe the different position of the wind. Therefore, it is indicated that the outflowing angle of the wind is not stable but variable.

Actually, time evolution of the wind triggered by the hydrodynamic instability is predicted by hydrodynamic simulations of UV line-driven disk winds performed by Proga, Stone & Kallman (2000) and Nomura (2014). Snap shots of these simulations for a black hole mass of $M_{\text{BH}} = 10^8 M_{\odot}$ and a mass accretion rate of $\dot{M}_{\text{acc}}/\dot{M}_{\text{Edd}} = 0.5$ are shown in Fig. 7.1. Each panel shows a density map taken at 13.3 (left), 14.6 (middle) and 16.47 yr (right) respectively. Apparently, the wind shown in red is flapping, and sometimes it disappears as shown in the right panel of the figure.

Interestingly, the variability of the viewing angle obtained by our analysis lies in a similar range of values to the theoretical predictions. Fig. 7.2 shows time variability of the viewing angles where UFOs are detected in the hydrodynamic simulations with

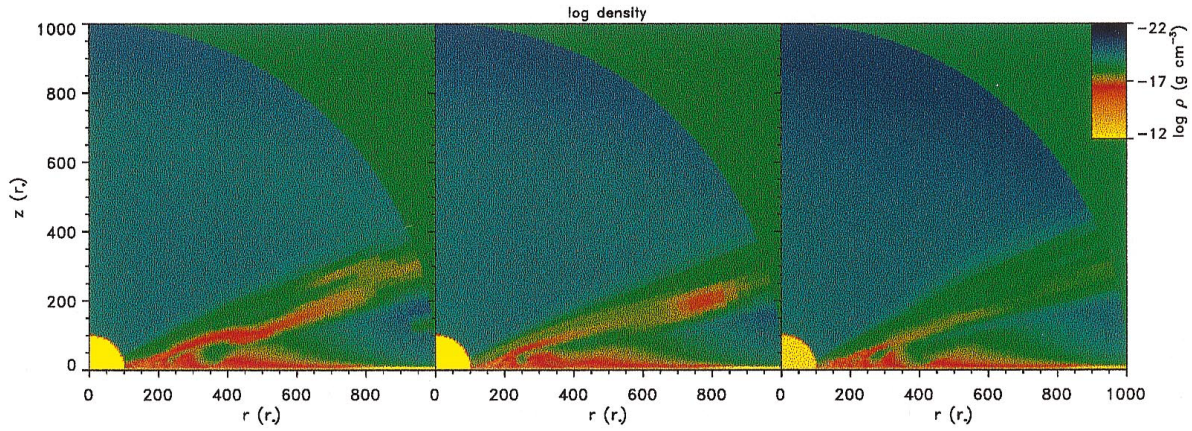


Figure 7.1: Sequence of density maps calculated by axisymmetric time-dependent hydrodynamic simulations of line-driven disk winds. The panels show the density maps at 13.3 (left), 14.6 (middle) and 16.47 yr (right) respectively. This figure is taken from Proga, Stone & Kallman (2000).

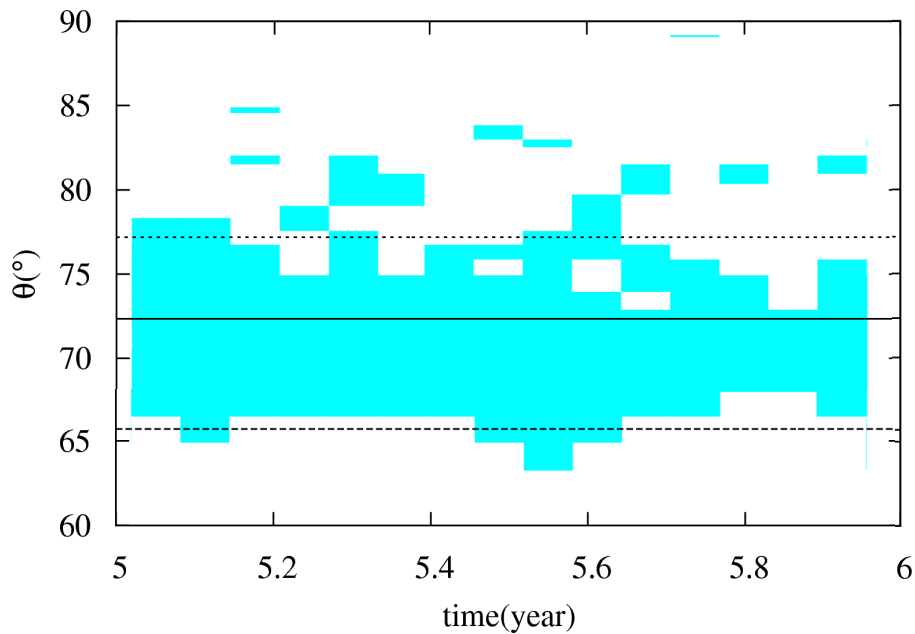


Figure 7.2: Time variability of the ranges of the viewing angle obtained by hydrodynamic simulations. The regions where the UFOs are detected are filled with cyan. The solid, dashed and dotted lines represents angles of 72.4° , 65.7° and 77.2° . This figure is taken from Nomura (2014).

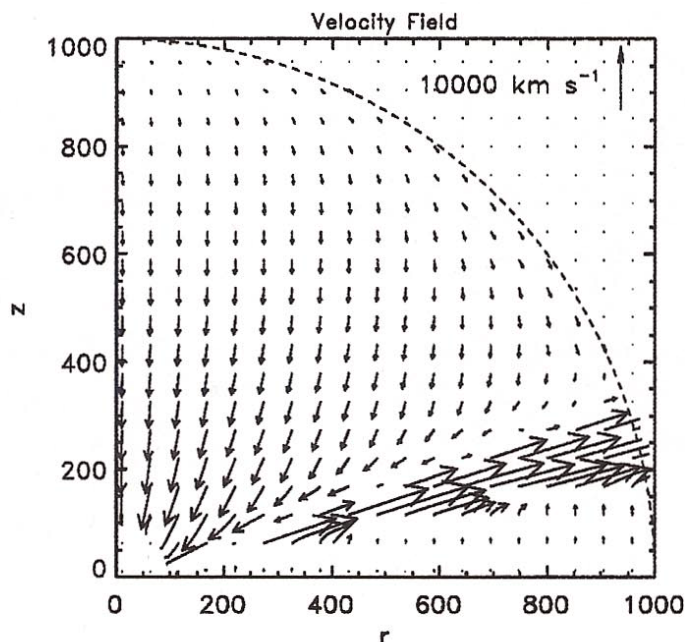


Figure 7.3: A velocity field map of the hydrodynamic simulations. Only the poloidal velocity component is plotted. This figure is taken from Proga, Stone & Kallman (2000).

same parameters as Fig. 7.1 (Nomura, 2014). From the figure, we find that the inner edge of the wind varies from $\theta \sim 63^\circ$ to $\sim 68^\circ$, while the outer edge of the wind varies from $\theta \sim 73^\circ$ to $\sim 80^\circ$ – 85° . Thus, its variation is $\sim 5^\circ$ – 12° , which is consistent with the values obtained by our analysis, namely $\sim 8^\circ$ ($\Delta\theta = 2^\circ$ – 10°) for PDS 456 and $\sim 8^\circ$ ($\Delta\theta = 27^\circ$ – 35°) for APM 08279+5255.

According to Proga, Stone & Kallman (2000), this variability is a consequence of Kelvin-Helmholtz instabilities. As shown in Fig. 7.3, a higher density wind moves outward, while lower density gas falls onto the black hole. This creates a large velocity shear, and it causes the instability. The time scale of the Kelvin-Helmholtz instability of a perturbation of length scale λ can be written as

$$\tau = \frac{\rho_1 + \rho_2}{2\pi\sqrt{\rho_1\rho_2}} \frac{\lambda}{v}, \quad (7.1)$$

where ρ_1 and ρ_2 are the densities of the wind and surrounding gas and v is the wind velocity. If we adopt typical values of our wind models for PDS 456 ($v \sim 10^{10}$ cm s $^{-1}$, $n_1 = \rho_1/m_p \sim 10^6$ cm $^{-3}$, $\lambda \sim 10^{17} \times \tan(5^\circ) \sim 10^{16}$ cm) and assume a density of the surrounding atmosphere $n_2 = \rho_2/m_p$ is one or two orders of magnitude smaller than n_1 , the time scale is $\tau \simeq 6$ – 20 days. This is consistent with the time scale of the observed variability.

In this picture, the UFOs always exist but a little fluctuation of the outflowing angle makes a large spectral variability. This means the UFOs continuously transport a large kinetic power to the surroundings, so that the total energy injection to the surroundings is larger. Thus, it is more likely that the UFOs play an important role in the coevolution of black holes and galaxies.

7.2 Inhomogeneous wind

As described in the previous section, we interpreted the variability as the change of the viewing angle, but such a variability is often interpreted as an effect of the inhomogeneity of the wind (e.g., Reeves et al., 2014; Gofford et al., 2014). In this section, we try to explain the observed variability of the absorption lines in 2013 by assuming a clumpy gas is transiting our line of sight.

If we assume that the clumpy absorber is fully covering the X-ray source in 2013c observation, the basic parameters of the absorber can be estimated by the best fit model for the 2013c spectrum ($\dot{M}_{\text{wind}} = 8 M_{\odot} \text{ yr}^{-1}$, $v_{\infty} = 0.26c$, $\theta_{\text{min}} = 38^{\circ}$ and $\theta_{\text{incl}} = 48^{\circ}$). In the best fit wind model, the ionization parameter is $\log \xi \sim 5.1$. By integrating the gas density along our line of sight, the column density is obtained to be $N_{\text{H}} = 5.7 \times 10^{23} \text{ cm}^{-2}$. The Doppler de-boosted luminosity in the energy range of 1–1000 Ry is $L \sim 2 \times 10^{45} \text{ erg s}^{-1}$.

The size, location and density of the clumpy absorber can be estimated by using the above values. The diameter of the clump ΔR is related to the rotational velocity v_{ϕ} and the time scale of the variability τ by $\tau v_{\phi} = \Delta R$. The rotational velocity follows an equation $v_{\phi} = v_{\phi 0} R_{\text{min}}/R$ (Eq. 4.6) from the conservation of the angular momentum. By combining the definitions of the column density ($N_{\text{H}} = n\Delta R$) and the ionization parameter ($\xi = L/nR^2$), the diameter ΔR , the velocity v_{ϕ} , the distance from the source R and the density n of the clumpy absorber are estimated: $\Delta R \sim 3 \times 10^{15} \text{ cm}$ ($\sim 10R_{\text{g}}$), $v_{\phi} \sim 30000 \text{ km s}^{-1}$, $R \sim 1 \times 10^{16} \text{ cm}$ ($\sim 30R_{\text{g}}$) and $n \sim 2 \times 10^8 \text{ cm}^{-3}$. Here, $\tau = 2 \times 5 \text{ day} = 8.6 \times 10^5 \text{ s}$ and $R_{\text{min}} = 20R_{\text{g}}$ are used. Therefore, the variability can be explained by the inhomogeneity of the wind if the observed absorber is located at a vicinity of the launching radius.

If such a transiting clumpy absorber is responsible for the variability of the absorption lines, the width of the absorption lines should not change. This contrasts to what is expected in the scenario of the instability of the wind geometry, where the line width increases with the increasing line depth. Since the current data do not give any lower limits of the line width (see Tab. 5.6), these two scenarios cannot be distinguished by

the line width. In the very near future, the next generation satellite *ASTRO-H* will solve this degeneracy as described in the last section in this chapter.

7.3 Launching mechanism of UFOs

7.3.1 Can UFOs be launched by UV line driving?

Although the launching mechanism of UFOs is unknown, the UV line driving mechanism is generally not thought to be important. This is because the UFOs are so highly ionized that there is no UV or even soft X-ray opacity left. Therefore, UV line driving cannot be accelerating the highly ionized material which we observe (Higginbottom et al., 2014).

However, our results imply the importance of radiative driving mechanism. By the analysis with our Monte Carlo simulations, the mass outflow rates are revealed to be $\dot{M}_{\text{wind}} = 10 (> 6.7) M_{\odot} \text{ yr}^{-1}$ for the 2007 spectrum of PDS 456 and $\dot{M}_{\text{wind}} = 66\text{--}82 M_{\odot} \text{ yr}^{-1}$ for the 2002 spectrum of APM 08279+5255, and the terminal velocities are $v_{\infty} = 0.298c\text{--}0.316c$ and $v_{\infty} = 0.4c (< 0.46c)$, respectively. These values mean the kinetic energy of the wind is $\sim 20\%$ or more of the radiation energy of each source, pointing to the importance of radiative driving in launching and accelerating the wind.

Moreover, here we suggest a solution to this issue. UV line driving could be launching and accelerating the material from the disc. As it rises higher, it is pushed outwards and ionized by the harder UV and X-ray radiation from the inner disc. The UV opacity is then mostly on the vertically rising part of the wind as shown in Fig. 7.4, which is outside of our line of sight.

We can estimate the effect of this in PDS 456. Without mass loss, such a disk should have $L(20\text{--}30R_g) = 0.64L(6\text{--}20R_g)$. If we consider the mass loss via the wind, since the mass outflow rate and mass inflow rate of PDS 456 are $\dot{M}_{\text{wind}}/\dot{M}_{\text{Edd}} = 0.13 (> 0.09)$ and $\dot{M}_{\text{acc}}/\dot{M}_{\text{Edd}} = 0.4$, the inner disk luminosity is reduced by $(\dot{M}_{\text{acc}} - \dot{M}_{\text{wind}})/\dot{M}_{\text{acc}} \simeq 2/3$, giving $L(20\text{--}30R_g) \approx L(6\text{--}20R_g)$. Assuming that the wind is launched vertically by the disk luminosity from $20\text{--}30R_g$, and pushed sideways by the inner disk luminosity from $6\text{--}20R_g$ gives an estimate for $\theta_0 \sim 45^\circ$, the angle the wind makes to the disc normal. This is even more convincingly close to our fiducial geometry than with the standard (no mass loss in a wind) disk (see Section 5.3.1).

Laor & Davis (2014) have done a much more exact calculation of the effect of mass loss on the disk structure. Their models include the energy to power the wind to its local escape velocity ($\epsilon = 1$) on the structure of the remaining disc, as well as the effect of angular momentum losses and decrease in mass accretion rate. They parameterize the mass loss rate from each surface element of the disc by using observed O star winds i.e.

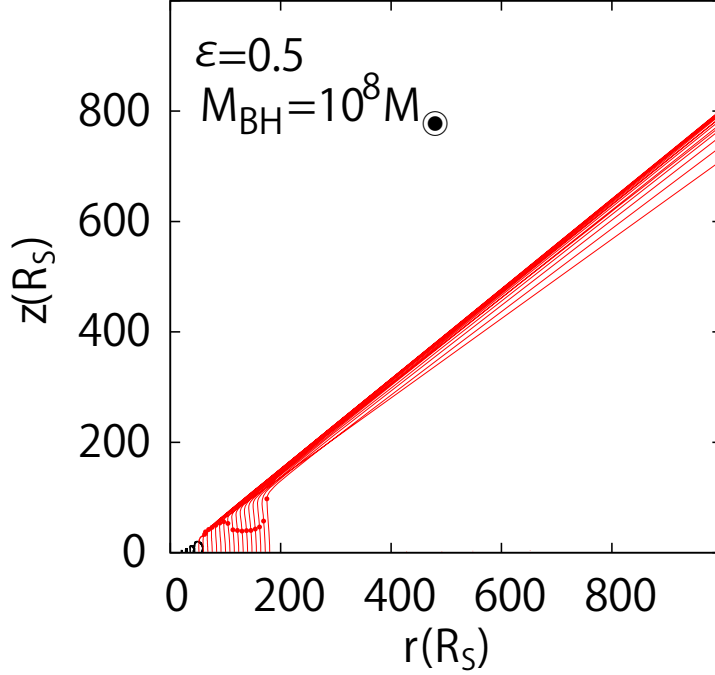


Figure 7.4: Steady structure of the line-driven disk wind for the Eddington ratio of $\epsilon = 0.5$ and black hole mass of $M_{\text{BH}} = 10^8 M_{\odot}$, calculated by a non-hydrodynamical method. This figure is taken from Nomura et al. (2013).

they assume that the winds are UV line driven, and scale for the different gravity (g) conditions. This gives a surface density mass loss rate of $\dot{\Sigma} \propto F^{2.32}/g^{1.11}$, where $F \propto T^4$ is the local surface flux. One should note that their results are applicable only for a high mass black hole such as PDS 456 and APM 08279+5255 because the temperature of O stars $\sim 2.8\text{--}5 \times 10^4$ K (Howarth & Prinja, 1989) is close to the disk temperatures expected for a high mass black hole.

Tab. 7.1 shows the full numerical calculation of UV-line driven winds (Shane Davis, private communication). This calculation is done for $10^9 M_{\odot}$ black hole for spin $a_* = 0$ (non-rotating black hole) and 0.9 (rotating black hole), accreting at $L/L_{\text{Edd}} = 0.3$ and 1. These show that mass loss rates of 30–50% of the mass inflow rate are expected from UV line driven disc winds assuming that the central X-ray flux does not overionize the wind. Therefore, the UFOs with $\dot{M}_{\text{wind}}/\dot{M}_{\text{acc}} \simeq 0.3$ observed in PDS 456 can be launched by UV line driving. In the case of APM 08279+5255, although many critical parameters including Eddington ratio and black hole mass are uncertain, the wind with $\dot{M}_{\text{acc}}/\dot{M}_{\text{acc}} = 0.43\text{--}0.55$ can be launched if Eddington ratio is similar to PDS 456.

Table 7.1: Full numerical calculation of UV-line driven winds. All accretion rates are in units of the Eddington accretion rate. (Shane Davis, private communication)

L/L_{Edd}	a^1	\dot{M}_{in}^2	\dot{M}_{acc}^3	\dot{M}_{wind}^4
0.3	0	0.302	0.515	0.21
	0.9	0.302	1.174	0.87
1.0	0	1.007	2.282	1.09
	0.9	1.007	5.588	4.58

¹ a is a black hole spin parameter.

² \dot{M}_{in} is the amount of mass that is actually accreted.

³ \dot{M}_{acc} is the accretion rate at large radius before the outflow set in.

⁴ \dot{M}_{wind} is the mass outflow rate. Therefore, \dot{M}_{acc} equals to $\dot{M}_{\text{in}} + \dot{M}_{\text{wind}}$.

7.3.2 Prediction of the relation between black hole mass and UFO acceleration

The X-ray power then becomes critically important in order not to overionize the wind. Here, the observational anti-correlation of X-ray flux with L/L_{Edd} in AGN is important (Vasudevan & Fabian 2007; Jin et al. 2012; Jin, Ward & Done 2012; Done et al. 2012 see their Fig 8a and b). While the underlying reason for this is not well understood, it is clear that as a source approaches L_{Edd} then radiation pressure alone means that winds become important, while the drop in the X-ray luminosity means that UV line driving becomes more probable since the X-ray ionization drops. This combination of continuum and UV line driving seems the most likely way to drive the most powerful winds.

This predicts that fast winds should be suppressed in lower L/L_{Edd} objects, as $L/L_{\text{Edd}} \ll 1$ means that the wind cannot be powered by continuum driving (definition of the Eddington limit) and the higher X-ray flux means that UV line driving is strongly suppressed. It also predicts that the fastest winds should be seen in the highest mass objects with $L/L_{\text{Edd}} \sim 1$ as these are the ones where the disk luminosity peaks in the UV rather than the far UV/soft X-rays, where the disk itself contributes to overionizing the wind.

Fig 7.5 shows the predicted spectral energy distributions for $L/L_{\text{Edd}} = 1$ for Schwarzschild black holes of mass 10^6 (blue) and $10^9 M_{\odot}$ (red). These assume that the accretion energy is dissipated in a standard (constant mass inflow rate) disc, and thermalizes to a (color temperature corrected) blackbody down to $10R_g$, and that 30% of the accretion energy

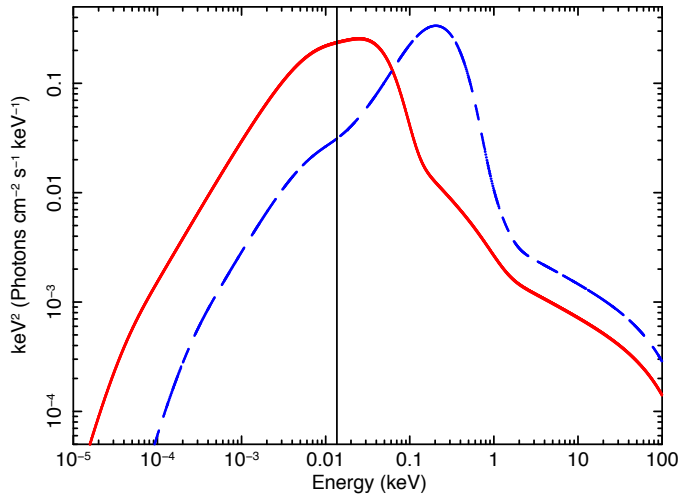


Figure 7.5: Predicted spectral energy distributions for spin zero black holes of mass 10^6 (blue) and $10^9 M_{\odot}$ (red). The black vertical line is at 13.6 eV Hydrogen ionization point which corresponds to the UV line driving bandpass. Here, we use OPTXAGNF (Done et al., 2012) and assume $L/L_{\text{Edd}} = 1$.

below this powers a tail to high energies with $\Gamma = 2.4$, while the remainder powers a low temperature, optically thick corona ($kT_e = 0.2$, $\tau = 15$: see Done et al. 2012). The black vertical line marks the 13.6 eV Hydrogen ionization point. A blackbody at O star temperatures will peak in the 10–18 eV range, so this indicates the UV line driving bandpass. Clearly the disk for the more massive black hole will have much stronger UV line driving than the less massive one. Simply assigning all of the disk luminosity to a UV band as is often done in hydrodynamic calculations to make them numerically tractable (Proga & Kallman, 2004; Nomura, 2014) does not include this mass dependence, so may overestimate the wind mass loss rates for lower mass AGN (e.g. Laor & Davis 2014).

Thus we expect the most powerful winds to be powered by a combination of continuum and UV line driving, and for these winds to be found in the most massive AGN. This is clearly the case, with the winds in PDS 456 and APM 08279+5255, both high mass ($> 10^9 M_{\odot}$) black holes at $L \sim L_{\text{Edd}}$, standing out as by far the highest velocity, highest mass loss rate objects (Tombesi et al., 2010; Gofford et al., 2013).

7.4 Future prospects

In this thesis, by using our new Monte Carlo simulation code, we have analyzed the *Suzaku* data of PDS 456, which is currently the highest quality data of the UFOs. As the results, we obtain a new possible picture for the origin of the spectral variability

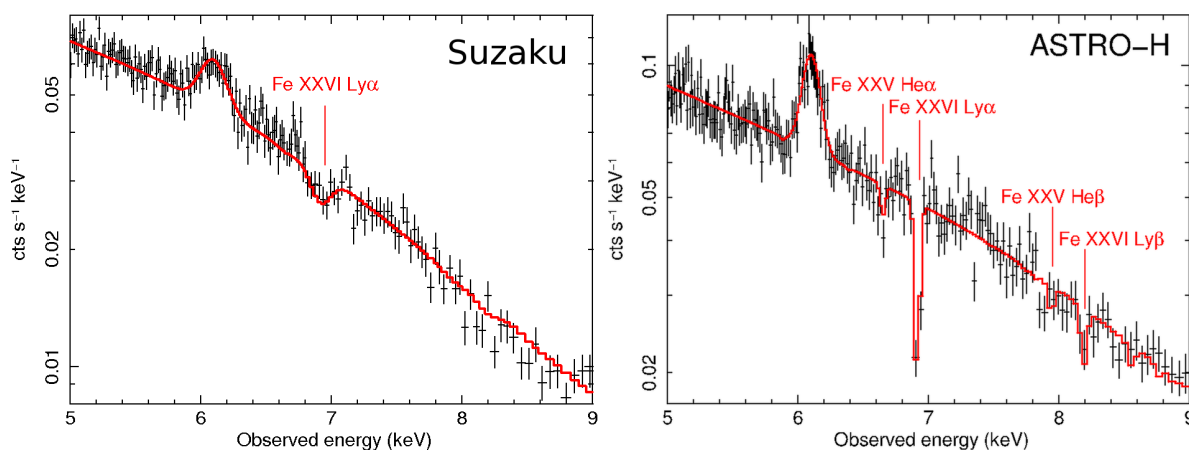


Figure 7.6: The observed (left) and simulated (right) spectra of the radio galaxy 3C 111. The left panel shows the *Suzaku* spectrum observed in 2008 with a 100 ks exposure time. The spectrum in the right panel is a simulated SXS spectrum with the same exposure time of 100 ks. In the SXS spectrum, the absorption lines of the UFO is clearly detected. These figures are taken from Kaastra et al. (2014).

and an important implication for the launching mechanism of the UFOs. However, the current instruments do not allow us to obtain any definitive conclusions for the launching mechanisms or the origin of the spectral variability. This is because the sensitivity of the current instruments are not so good above ~ 7 keV, where the absorption lines of the UFOs are observed.

In a little while, the quality of the observational data will be dramatically improved by the next generation X-ray satellite, *ASTRO-H* (Takahashi et al., 2012). The *ASTRO-H* is the sixth X-ray satellite led by the Institute of Space and Astronautical Science (ISAS) of Japan Aerospace Exploration Agency (JAXA), and is scheduled for launch in 2015.

The soft X-ray spectrometer (SXS) onboard *ASTRO-H* will provide us a high spectral resolution of ≤ 7 eV in the energy range from 0.3 to 12 keV, which is over one order of magnitude better than *Suzaku*. This great improvement is essential for the significant detection of the UFOs. Fig. 7.6 shows the simulated SXS spectrum (right) and observed *Suzaku* spectrum (left) of the radio galaxy 3C 111. The absorption lines of the UFO, which is marginally detected in the *Suzaku* spectrum, are clearly detected at the $\sim 20\sigma$ level. Therefore, we can investigate the ubiquitousness of the UFOs, which strongly relates to the UFO's contribution to the evolution of the galaxies.

Also, in the case of the SXS spectrum of 3C 111, the line width can be constrained with $\sim 5\%$ errors. This will possibly give us an answer for the question whether the UFO is an inhomogeneous clumpy wind or a homogeneous wind (just like our wind model)

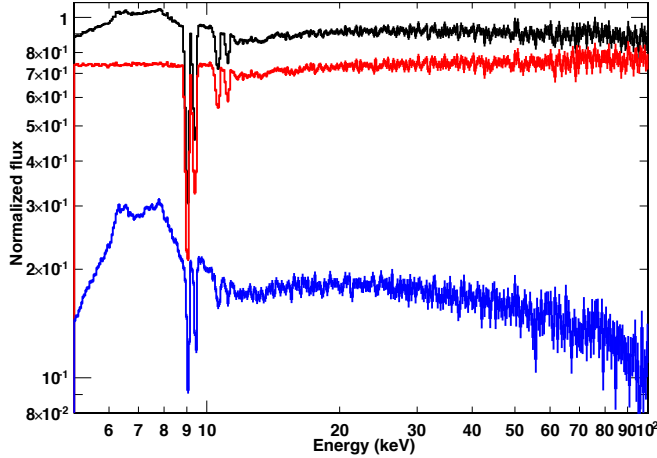


Figure 7.7: The expected spectra of the UFOs in the energy range of 5–100 keV calculated by our Monte Carlo simulation. The direct components are plotted in red, the reprocessed components are in blue and the sums of these components are in black.

because the clumpy wind should not show broad absorption lines in general. For much brighter sources such as PDS 456, the line profiles can be studied for the first time. This gives an essential information of the launching mechanism of the UFOs because the line profiles reflect the relation between the velocity (blue-shift) and the column density (line depth), which directly depend on how the materials are accelerated.

In the higher energy band, the UFO spectra is expected to be distorted by the reprocessed component (blue line in Fig. 7.7), which gives informations of the materials located at the outside of our line of sight. Just like the emission line (see section 5.3.3), the reprocessed spectra in higher energy band can be a probe of the geometry. The hard X-ray imager (HXI) onboard *ASTRO-H* can achieve a 100 times better sensitivity than *Suzaku* in the energy range from 10 keV up to 80 keV. This will probably provide us a new insight on the geometrical structure of the UFOs, which is a direct verification of the scenario of the instability of the wind geometry.

In the *ASTRO-H* era, our simulation code will be of great importance for the spectral analysis. Especially, modeling of the reprocessed component from the realistic geometry with nonuniform distributions of the velocity and the density is possible only by Monte Carlo simulations.

Chapter 8

Disk wind interpretation of peculiar spectra in 1H 0707-495

A narrow-line Seyfert 1 galaxy 1H 0707-495 ($z = 0.040568$) is a very famous source for its huge and sharp spectral drop at 7 keV (Boller et al., 2002), whose origin is unknown. Some works claim such a peculiar feature is evidence that we are observing emission from the material at the vicinity of the black hole (Fabian et al., 2004). In this model, the spectral drop is explained as the blue end of the broad Fe fluorescence line. The other explanation is that it is the Fe K edge resulting from partial covering absorbers (Gallo et al., 2004; Tanaka et al., 2004).

However, we try to explain such a peculiar spectrum with UFOs. Reproducing such a feature with our wind model would provide a novel pathway for its production. Moreover, this source is a low mass system with black hole mass of $\sim 10^6 M_{\odot}$ while PDS 456 and APM 08279+5255 harbor large black holes $\sim 10^{9-10} M_{\odot}$, so that the disk temperatures are completely different. Therefore, investigating this source is also meaningful to study the launching mechanisms of the UFOs.

8.1 Observational data

1H 0707-495 has been observed by *Suzaku* and *XMM-Newton* for many times as listed in Tab. 8.1. We reduce both *XMM-Newton* and *Suzaku* data in the same way as performed for PDS 456 and APM 08279+5255. The screening conditions are completely the same as described in chapter 5 and 6. When MOS detectors are operated in small window modes, we do not use them because we are not able to select the background region from the same chip as the source region. The observed data show a large variability in continuum spectra as seen in Fig. 8.1. The change in continuum shape looks the same as that of PDS 456

Table 8.1: *XMM-Newton* and *Suzaku* observations of 1H 0707-495

Name	Obs ID	Start Date	Net exposure (ks) ¹
<i>XMM-Newton</i>			
Obs1	0110890201	2000-10-21	42.7/42.7/37.8
Obs2	0148010301	2002-10-13	76.1/76.3/68.1
Obs3	0506200301	2007-05-14	-/-/35.8
Obs4	0506200201	2007-05-16	-/-/26.9
Obs5	0506200501	2007-06-20	-/-/32.6
Obs6	0506200401	2007-07-06	-/-/14.7
Obs7	0511580101	2008-01-29	-/-/99.6
Obs8	0511580201	2008-01-31	-/-/66.4
Obs9	0511580301	2008-02-02	-/-/59.8
Obs10	0511580401	2008-02-04	-/-/66.6
Obs11	0653510301	2010-09-13	-/-/103.7
Obs12	0653510401	2010-09-15	-/-/102.1
Obs13	0653510501	2010-09-17	-/-/95.8
Obs14	0653510601	2010-09-19	-/-/97.7
Obs15	0554710801	2011-01-12	-/-/64.5
<i>Suzaku</i>			
SuzakuObs	700008010	2005-12-03	97.9/100.4/97.2/97.8

¹ Net exposure time of MOS1/MOS2/PN for *XMM-Newton* and XIS0/XIS1/XIS2/XIS3 for *Suzaku*, respectively.

if we ignore the soft excess emission below 2 keV. Therefore, we assume an additional absorber makes the continuum variability and the intrinsic spectrum is stable.

For the purpose of determining the intrinsic spectral shape, we fit the 2–6 keV spectra for each observational data. The data named Obs12 observed on 2010-09-15 shows a steepest spectrum with photon index of $\Gamma = 2.60 \pm 0.05$. With our assumption of an additional absorber, the steepest spectra are the less absorbed spectra, so it is approximately the intrinsic spectra.

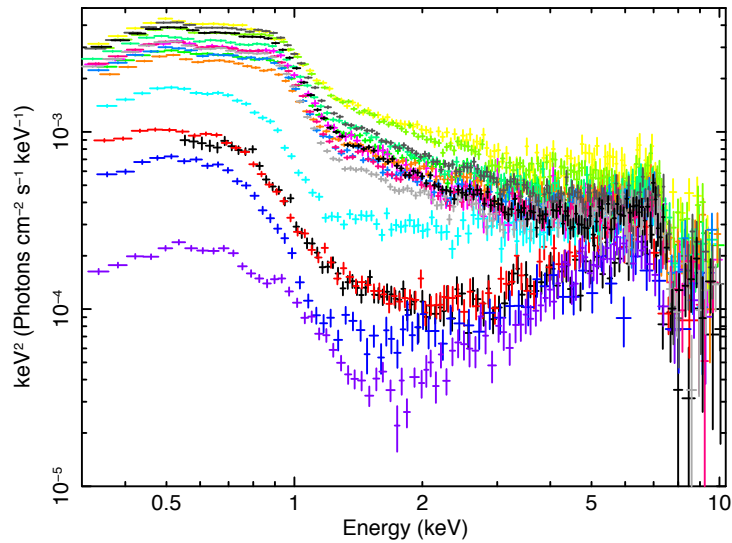


Figure 8.1: All spectra observed by *XMM-Newton*/pn and *Suzaku*/FI detectors, unfolded against a $\Gamma = 2$ power law.

8.2 Parameter estimation with the phenomenological model

Firstly, we fit the spectra of Obs12 with the phenomenological model introduced in section 6.4, because its spectrum is thought to be an unabsorbed spectrum. The reflection components from the wind or the disk are represented by an ionized reflection model REFLIONX. For this source, the ratio of He-like and H-like ions is fixed at unity because the broadened absorption feature is not sensitive to this parameter. Actually, we can obtain no constraints on this parameter even if it is allowed to vary. The obtained best fit model are plotted in the left panel of Fig. 8.2 and the parameters are listed in Tab. 8.2. The peculiar spectral dropping structure above ~ 7 keV is well reproduced by the convolved absorption lines and edge.

As an alternative to REFLIONX, we try to represent the emission component with the simple Gaussian line. The model spectra and parameters are shown in Fig. 8.2 and Tab. 8.2. We obtained an extremely broadened Gaussian line and steeper powerlaw continuum but it is not unusual if the wind velocity is as fast as $\sim 0.3c$, which can make blue shifted and red shifted 6.7/7.0 keV lines ranging from 4.9 keV up to 9.5 keV. The fit statistics are worse than that with REFLIONX although the Gaussian model has more free parameters.

As the spectral parameters of the phenomenological model are obtained, we convert them to the physical parameters. To do so, we need to know the black hole mass

Table 8.2: Fitting result of Obs12 spectrum with the convolved absorption model

Model Component	Fit Parameter	Value (90% error)	
Powerlaw	Γ	$2.61_{-0.04}^{+0.05}$	$2.81_{-0.10}^{+0.17}$
	$F_{2-10 \text{ keV}} (10^{-12} \text{ erg s}^{-1} \text{ cm}^{-2})$	1.2 ¹	1.1
	$L_{2-10 \text{ keV}} (10^{42} \text{ erg s}^{-1})$	4.3	3.9
Convolved absorption	δ_0	$1.174_{-0.015}^{+0.014}$	$1.169_{-0.012}^{+0.014}$
	$\Delta\delta$	$0.067_{-0.056}^{+0.052}$	$0.109_{-0.051}^{+0.040}$
	$N(\text{Fe XXV})+N(\text{Fe XXVI}) (10^{18} \text{ cm}^{-2})$	$9.1_{-3.2}^{+4.8}$	$11.4_{-3.6}^{+4.7}$
Reflection	ξ	> 5000	—
Gaussian emission	E (keV)	—	$6.21_{-0.70}^{+0.50}$
	σ	—	$1.43_{-0.44}^{+0.76}$
	EW (keV)	—	$1.40_{-1.17}^{+0.96}$
Fit statistics	χ^2/dof	101.8/84	106.0/83
	Null probability	0.09	0.05

¹ Both of direct and reflection component are included.

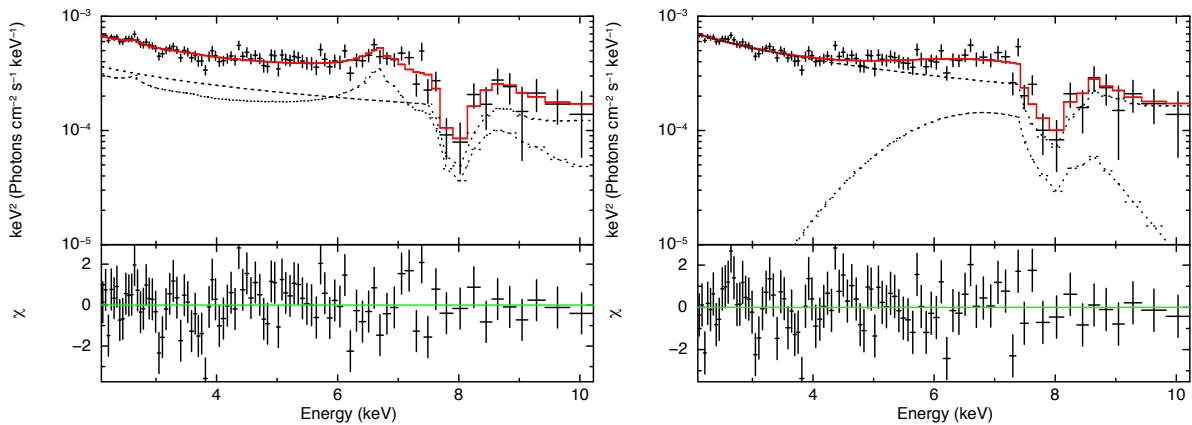


Figure 8.2: Best fit model and spectrum of Obs12. Left: ionized reflection REFLIONX, right: Gaussian emission

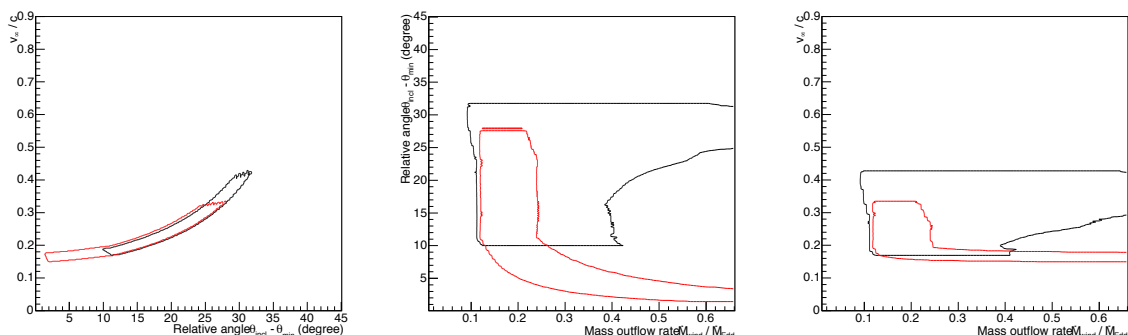


Figure 8.3: Contour plots of the physical parameters with the 90% confidence level for the Obs12 spectrum. The result from the model with ionized reflection REFLIONX is shown in red, and Gaussian emission model is in black.

of this source because the observed luminosity should be written in Eddington units. Tanaka et al. (2004) reported the black hole mass is higher than $2 \times 10^6 M_{\odot}$ if required to be smaller than the Eddington limit. Fabian et al. (2009) estimated the mass to be $\sim 5 \times 10^6 M_{\odot}$ from the observed lag of the relativistic reflection component by assuming the distance of the emission region from the black hole. Therefore, we adopt $M_{\text{BH}} = 5 \times 10^6 M_{\odot}$.

The resulted wind parameters are $\Delta\theta = 12.90_{-11.40}^{+15.10}$, $v_{\infty}/c = 0.20_{-0.05}^{+0.13}$ and $\dot{M}_{\text{wind}}/\dot{M}_{\text{Edd}} = 0.17 (> 0.12)$ for the model with REFLIONX. For the model with a Gaussian emission line, slightly different parameters are obtained: $\Delta\theta = 24.70_{-14.70}^{+7.00}$, $v_{\infty}/c = 0.30_{-0.13}^{+0.13}$ and $\dot{M}_{\text{wind}}/\dot{M}_{\text{Edd}} = 0.25_{-0.15}^{+0.41}$. The contour plots of the physical parameters are shown in Fig. 8.3. The black contour is obtained by using Gaussian model to reproduce the observed emission feature while the red contour is by the ionized reflection model REFLIONX. As shown, two contours are consistent within 90% errors but the black contour is larger. If we use the Gaussian model for the emission feature, the obtained confidence contour becomes a little higher inclination and velocity. This corresponds to a larger value of $\Delta\delta$. Also, the contour extends to a larger mass outflow rate, which is caused by a larger value of column density.

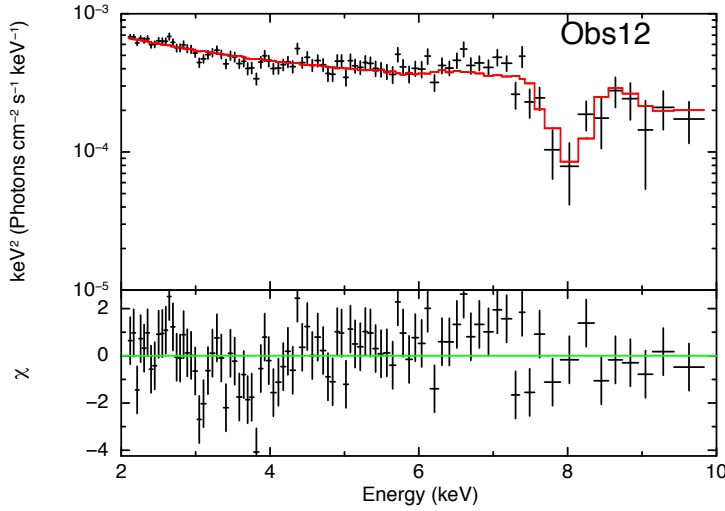


Figure 8.4: Observed spectrum and MONACO model with $v = 0.2c$ and $\dot{M}_{\text{wind}}/\dot{M}_{\text{Edd}} = 0.20$ for Obs12.

8.3 Comparison with the Monte Carlo simulations of the disk wind

We run the MONACO with the parameters around the values obtained in the previous section. We choose $v_{\infty} = 0.2c$ and $\dot{M}_{\text{wind}}/\dot{M}_{\text{Edd}} = 0.13, 0.20, 0.26$. These parameters are almost at the center of the 90% contour of v_{∞} and \dot{M}_{wind} for the model with Gaussian emission as well as the model with REFLIONX. Thus, this parameter set is thought to give us an acceptable fit independent from the emission line model used to estimate these parameters.

These models give good fit statistics of $\chi^2 = 139.7, 132.0$ and 133.3 for degree of freedom of 89, respectively for $\dot{M}_{\text{wind}}/\dot{M}_{\text{Edd}} = 0.13, 0.20, 0.26$. The best fit spectra with $\dot{M}_{\text{wind}}/\dot{M}_{\text{Edd}} = 0.20$ is plotted in Fig. 8.4. Although χ^2 is not quite good, the absorption structure is well reproduced.

We apply the model with $\dot{M}_{\text{wind}}/\dot{M}_{\text{Edd}}$ to all the observations of 1H 0707-495. All the spectra and models are plotted in Fig. 8.5, and parameters are listed in Tab. 8.3. For all observations, the photon index is fixed at $\Gamma = 2.6$. The continuum absorptions are represented by ZXIPCF model as in the case of PDS 456. For Obs8 and Obs12, the continuum absorption component is not included because the significance of adding ZXIPCF does not exceed the 99% confidence level of F-test.

As shown in Fig. 8.5, our MONACO models roughly reproduce the absorption feature all the observed spectra. The best fit values of inclination angle ranges from $\sim 58^\circ$ to

75° , which is a much wider range than the cases of PDS 456 and APM 08279+5255. If compared with the previous two targets, the mass outflow rate and the terminal velocity are almost same: $\dot{M}_{\text{wind}}/\dot{M}_{\text{Edd}} = 0.2$, $v_\infty = 0.2c$ for this target, and $\dot{M}_{\text{wind}}/\dot{M}_{\text{Edd}} = 0.1$ – 0.2 , $v_\infty = 0.2$ – $0.5c$ for PDS 456 and APM 08279+5255.

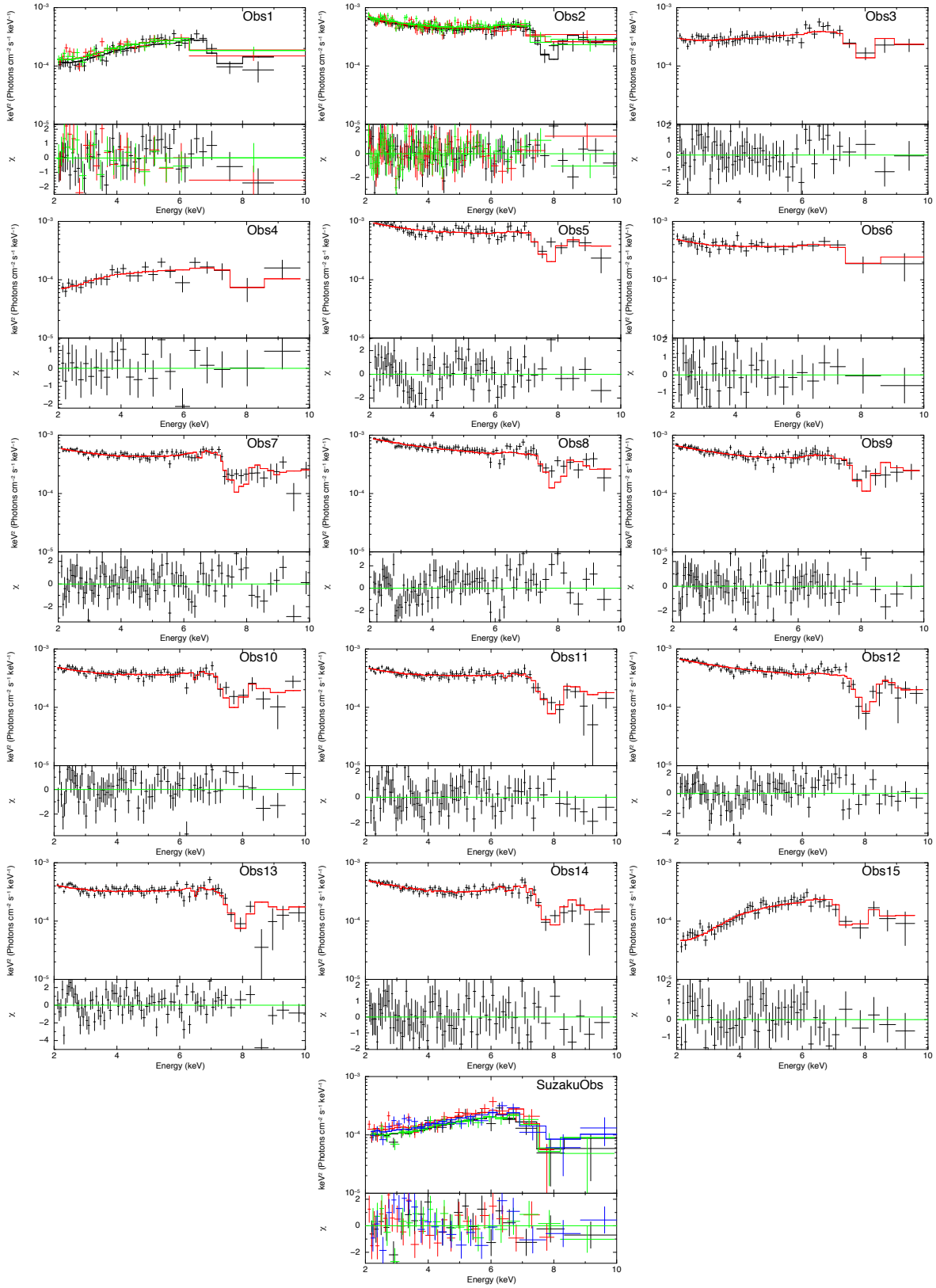


Figure 8.5: Observed spectra and MONACO models with $v = 0.2c$ and $\dot{M}_{\text{wind}}/\dot{M}_{\text{Edd}} = 0.2$ for all the observations.

Table 8.3: MONACO fit with $v = 0.2c$ and $\dot{M}_{\text{wind}}/\dot{M}_{\text{Edd}} = 0.2$

Name	Continuum absorption		MONACO wind		Fit statistics	
	N_{H} (cm^{-2})	$\log \xi$	f_{cov}	θ_{incl}	χ^2/dof	Null probability
Obs1	23_{-4}^{+16}	$1.80_{-0.41}^{+0.38}$	$0.82_{-0.02}^{+0.04}$	$74.5_{-3.9}^{+2.8}$	76.3/78	0.53
Obs2	63_{-26}^{+83}	1.90 (< 2.34)	$0.45_{-0.07}^{+0.09}$	$64.0_{-3.1}^{+1.2}$	203.1/203	0.48
Obs3	15_{-6}^{+37}	1.69×10^{-3} (< 1.63)	$0.68_{-0.05}^{+0.05}$	$64.1_{-6.3}^{+2.8}$	52.7/55	0.56
Obs4	$8.2_{-6.3}^{+18.2}$	0.14 (< 2.28)	$0.80_{-0.06}^{+0.19}$	57.9 ¹	15.1/21	0.82
Obs5	23_{-16}^{+72}	0.21 (< 2.14)	$0.28_{-0.09}^{+0.44}$	$68.0_{-1.6}^{+1.5}$	102.6/69	0.005
Obs6	$8.4_{-4.5}^{+90.6}$	-2.58 (< 2.02)	$0.42_{-0.14}^{+0.29}$	$63.4_{-12.7}^{+5.6}$	28.2/34	0.75
Obs7	151_{-95}^{+11}	$2.71_{-0.56}^{+0.10}$	$0.71_{-0.25}^{+0.06}$	$68.3_{-1.7}^{+1.7}$	115.1/87	0.02
Obs8	—	—	—	$64.0_{-2.3}^{+2.5}$	129.12/84	0.001
Obs9	65_{-31}^{+73}	1.24 (< 2.26)	$0.42_{-0.21}^{+0.41}$	$58.3_{-1.9}^{+2.9}$	88.6/79	0.22
Obs10	124_{-109}^{+33}	$2.71_{-1.90}^{+0.19}$	$0.58_{-0.14}^{+0.16}$	$68.2_{-2.6}^{+2.2}$	87.4/72	0.10
Obs11	121_{-73}^{+32}	$2.76_{-0.46}^{+0.21}$	$0.60_{-0.24}^{+0.20}$	$63.1_{-2.6}^{+3.3}$	100.3/81	0.07
Obs12	—	—	—	$60.6_{-1.8}^{+2.5}$	132.0/89	0.002
Obs13	117_{-63}^{+28}	$2.73_{-0.31}^{+0.15}$	$0.63_{-0.20}^{+0.13}$	$63.2_{-2.6}^{+2.4}$	154.9/78	5×10^{-7}
Obs14	181_{-8}^{+203}	$2.82_{-0.09}^{+0.10}$	$0.82_{-0.08}^{+0.07}$	$63.1_{-2.6}^{+2.3}$	75.3/77	0.53
Obs15	23_{-6}^{+47}	$1.61_{-0.78}^{+1.02}$	$0.93_{-0.02}^{+0.04}$	$70.9_{-3.8}^{+3.7}$	43.1/51	0.78
SuzakuObs	109_{-69}^{+27}	$2.72_{-1.47}^{+0.07}$	$0.89_{-0.08}^{+0.08}$	$67.0_{-5.4}^{+5.9}$	97.9/86	0.18

¹ No constraints on this parameter were obtained.

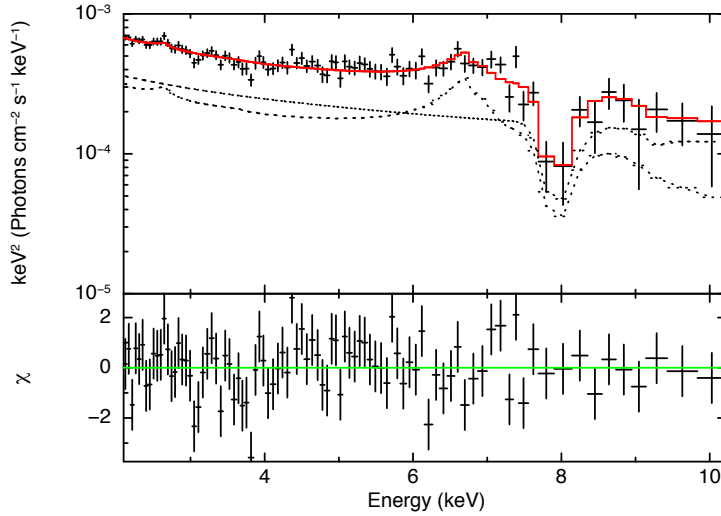


Figure 8.6: Best fit model and spectra of Obs12 with a large turbulence model.

8.4 Solution of the failed wind

In the model used in the previous section, the absorption lines are broadened by a large range of velocity components due to a high inclination. Instead, there is the other possible solution for 1H 0707-495, where a large turbulent velocity accounts for the absorption line broadening. This solution is based on the idea that a material is accelerated up to a certain velocity but it does not reach to the escape velocity, so that it comes back to the disk surface. Such materials are often referred to as “failed wind”, which is expected to be formed at the very inner region in the radiation driven disk wind model.

First, we determine the parameters by the phenomenological model with a large turbulence. In this model, the lines are not convolved, so that the line is broadened by only the turbulence. The best fit model is shown in Fig. 8.6, and parameters are listed in Tab. 8.4. The parameter kT in the table corresponds to the turbulence. The best fit value $kT = 1000\text{--}65000$ keV is interpreted as the turbulent velocity of $v_t = 2000\text{--}15000$ km s⁻¹. Interestingly, the lower limit of the Doppler factor δ_0 is 1.168 corresponding to $\sim 0.15c$ if $\theta = 0$, so that δ_0 must be larger than $\sim 0.15c$. This constraint is come from the fact that the position of spectral drop in Obs12 is at ~ 7.5 keV in the source rest frame. In this section, since we are thinking of the failed wind, the outflow velocity should be zero or very small. Thus, we adopt the slowest values of $v_\infty = 0.15c$ and $v_t = 10000$ km s⁻¹. Also, in the slowest solution, the inclination angle should be close to the wind angle ($\sim \theta_{\min}$).

The mass outflow rate is determined by the fitting parameter $N(\text{Fe XXV}) + N(\text{Fe XXVI})$. If $\dot{M}_{\text{wind}}/\dot{M}_{\text{Edd}}$ is 0.66 ($\dot{M}_{\text{wind}} = 0.125 M_\odot \text{ yr}^{-1}$), the column density can be values on

Table 8.4: Fitting result of Obs12 spectrum with the phenomenological absorption model without a velocity convolution ($\Delta\delta = 0$).

Model Component	Fit Parameter	Value (90% error)
Powerlaw	Γ	$2.61^{+0.05}_{-0.04}$
	$F_{2-10 \text{ keV}}$ ($10^{-12} \text{ erg s}^{-1} \text{ cm}^{-2}$)	1.2^1
	$L_{2-10 \text{ keV}}$ ($10^{42} \text{ erg s}^{-1}$)	4.3
Wind absorption	δ_0	$1.179^{+0.048}_{-0.011}$
	kT (keV)	$1.7^{+4.8}_{-1.6} \times 10^4$
	$N(\text{Fe XXV})+N(\text{Fe XXVI})$ (10^{18} cm^{-2})	$8.0^{+181.9}_{-3.5}$
	$N(\text{Fe XXVI})/N(\text{Fe XXV})$	0.4^2
Reflection	ξ	> 5000
Fit statistics	χ^2/dof	$101.4/83$
	Null probability	0.08

¹ Both of direct and reflection component are included.

² No constraints on the confidence intervals.

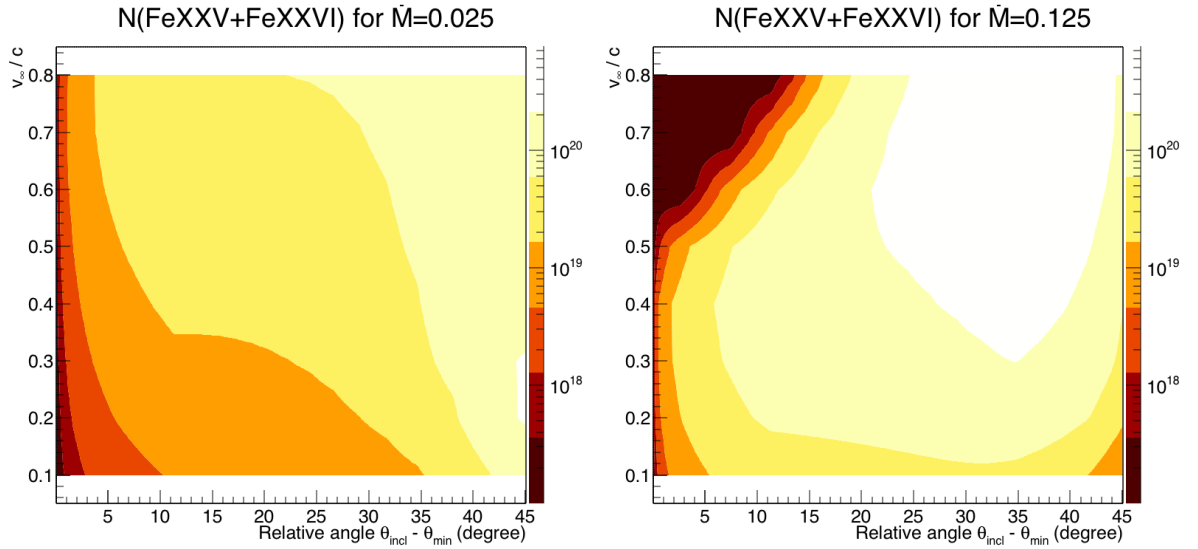


Figure 8.7: Dependence of $N(\text{Fe XXV} + \text{Fe XXVI})$ on the terminal velocity v_∞ and relative angle $\theta_{\text{incl}} - \theta_{\text{min}}$. Left panel is for $\dot{M}_{\text{wind}} = 0.025 M_\odot \text{ yr}^{-1}$, and right panel is for $\dot{M}_{\text{wind}} = 0.125 M_\odot \text{ yr}^{-1}$.

the right panel in Fig. 8.7. The column density at $v_\infty = 0.15c$ and $\Delta\theta \equiv \theta_{\text{incl}} - \theta_{\text{min}} \lesssim 5^\circ$ is $4 \times 10^{17} - 3 \times 10^{19} \text{ cm}^{-2}$, which matches with the fitting results listed in Tab. 8.4. On the other hand, in the left panel with $\dot{M}_{\text{wind}}/\dot{M}_{\text{Edd}} = 0.13$, the column density is smaller than $\sim 4 \times 10^{18} \text{ cm}^{-2}$. Thus, the mass outflow should be between these values.

We run MONACO simulation with $\dot{M}_{\text{wind}}/\dot{M}_{\text{Edd}} = 0.5$, $v_\infty = 0.15c$ and $v_t = 10000 \text{ km s}^{-1}$, and apply it to all the observations. The best fit parameters are listed in Tab. 8.4, and the spectra and models are plotted in Fig. 8.8. We obtained comparably good fits with that in the previous section. As expected, the inclination angles are close to $\theta_{\text{min}} = 45^\circ$. This means the absorption lines are maximally blue shifted with $v_\infty = 0.15c$, so that this parameter set is the slowest solution.

Table 8.5: MONACO fit with $v = 0.15c$, $v_t = 10000 \text{ km s}^{-1}$ and $\dot{M}_{\text{wind}}/\dot{M}_{\text{Edd}} \simeq 0.5$

Name	Continuum absorption			MONACO wind	Fit statistics	
	$N_{\text{H}} \text{ (cm}^{-2}\text{)}$	$\log \xi$	f_{cov}	θ_{incl}	χ^2/dof	Null probability
Obs1	23_{-4}^{+8}	$1.91_{-0.45}^{+0.15}$	$0.81_{-0.02}^{+0.08}$	$70.3_{-5.6}^{+7.5}$	74.8/78	0.58
Obs2	138_{-82}^{+30}	$2.80_{-2.04}^{+0.31}$	$0.48_{-0.30}^{+0.18}$	$46.9_{-0.7}^{+0.9}$	200.8/203	0.53
Obs3	18_{-13}^{+32}	1.53 (< 2.56)	$0.65_{-0.08}^{+0.07}$	47.1 (< 49.6)	49.0/55	0.70
Obs4	$8.4_{-5.2}^{+17.4}$	0.51 (< 2.42)	0.81 (> 0.74)	47.2 (< 58.2)	15.3/21	0.81
Obs5	—	—	—	46.0 (< 47.4)	115.1/72	9.4×10^{-4}
Obs6	$8.4_{-5.9}^{+55.9}$	-1.25 (< 3.26)	$0.35_{-0.13}^{+0.24}$	49.4 (< 54.7)	28.3/34	0.74
Obs7	66_{-22}^{+60}	$2.72_{-0.25}^{+0.20}$	$0.36_{-0.05}^{+0.20}$	$47.0_{-0.7}^{+0.9}$	117.6/87	0.02
Obs8	—	—	—	46.5 (< 47.4)	110.8/84	0.03
Obs9	—	—	—	46.4 (< 47.6)	93.7/82	0.18
Obs10	54_{-31}^{+64}	$2.73_{-0.37}^{+0.33}$	$0.35_{-0.07}^{+0.24}$	$47.3_{-1.0}^{+1.4}$	91.2/72	0.06
Obs11	55_{-27}^{+64}	$3_{-0.44}^{+0.21}$	$0.52_{-0.21}^{+0.32}$	$48.5_{-1.3}^{+1.5}$	103.1/81	0.05
Obs12	—	—	—	$49.0_{-1.3}^{+1.2}$	123.8/89	0.009
Obs13	65_{-25}^{+45}	$2.75_{-0.23}^{+0.30}$	$0.43_{-0.05}^{+0.25}$	$48.9_{-1.5}^{+1.4}$	153.1/78	8.2×10^{-7}
Obs14	184_{-22}^{+126}	$2.94_{-0.14}^{+0.12}$	$0.78_{-0.12}^{+0.08}$	$48.3_{-1.1}^{+1.5}$	77.8/77	0.45
Obs15	61_{-8}^{+17}	$2.73_{-0.18}^{+0.04}$	0.96 (> 0.93)	46.5 (< 49.8)	54.3/51	0.35
SuzakuObs	34_{-29}^{+60}	2.20 (< 2.74)	$0.88_{-0.14}^{+0.07}$	$60.0_{-3.8}^{+5.9}$	92.9/86	0.29

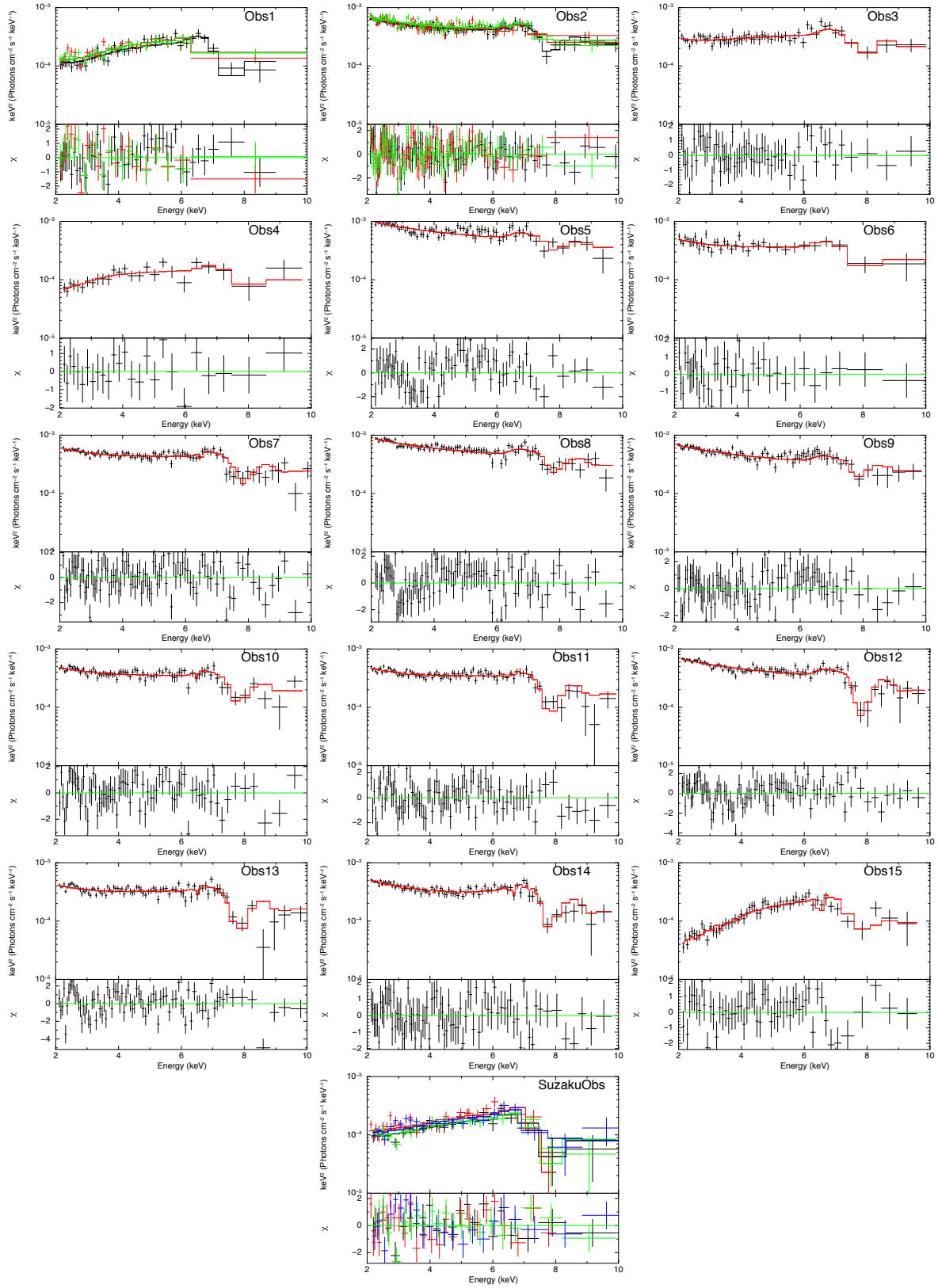


Figure 8.8: Observed spectra and MONACO models with $v = 0.15c$, $v_t = 10000 \text{ km s}^{-1}$ and $\dot{M}_{\text{wind}}/\dot{M}_{\text{Edd}} \simeq 0.5$ for all the observations.

8.5 Discussion on the peculiar spectral drop

8.5.1 Self-similar disk wind

The spectral drop at ~ 7 keV in a narrow line Seyfert 1 1H 0707-495 was successfully reproduced by our wind model. Although the fit statistics are not quite good for some observations, absorption features in our model match the observed spectra. The best estimates of the mass outflow rate and the terminal velocity are $\dot{M}_{\text{wind}}/\dot{M}_{\text{Edd}} = 0.2$ and $v_{\infty} = 0.2c$, respectively, which are almost same as PDS 456 and APM 08279+5255.

This result indicates that the 1H 0707-495 has the similar UFO as PDS 456 and APM 08279+5255 in spite of a large difference of their black hole mass. The black hole mass of 1H 0707-495 is $\sim 10^6 M_{\odot}$, while that of PDS 456 and APM 08279+5255 are $\sim 10^9 M_{\odot}$ and $\sim 10^{10} M_{\odot}$, respectively. These independency of the black hole mass is sometimes called “self-similarity”.

As discussed in Chapter 7, UV line driven wind should not be self-similar. As shown in Fig. 7.5, these AGN with different black hole masses should have different UV luminosities. In the case of $\sim 10^9 M_{\odot}$ and $\sim 10^6 M_{\odot}$ black holes, the UV luminosities normalized by their bolometric luminosities are one order of magnitude different. In addition to this, the soft X-ray flux is relatively higher in a low mass black hole, which overionizes the wind and reduce the cross-section for the UV photons.

Therefore, the possible driving mechanisms are the magnetic driving and the radiation pressure driving by the continuum radiation, but currently we cannot distinguish these two mechanisms. The magnetic driving mechanism predicts a large rotational velocity because the wind should corotate with the accretion disk (e.g., Proga, 2007). This would make a difference on the emission line structure, but current data cannot allow us to investigate it. In the future, it would be possible when the higher quality data are obtained by the future X-ray missions such as *ASTRO-H* and *Athena*.

8.5.2 The failed wind in UV-line driving model

Alternatively, a model with a large turbulence instead of a large velocity range due to a high inclination angle is also able to explain the observed spectral drop. The MONACO simulation with $\dot{M}_{\text{wind}}/\dot{M}_{\text{Edd}} = 0.5$, $v_{\infty} = 0.15c$ and the large turbulent velocity $v_t = 10000 \text{ km s}^{-1}$ gives a comparably good fits to the model with $\dot{M}_{\text{wind}}/\dot{M}_{\text{Edd}} = 0.2$ and $v_{\infty} = 0.2c$. Also, we found that the terminal velocity should be larger than $v_{\infty} \simeq 0.15c$ to reproduce the observed spectra no matter how large the turbulence is.

This wind model with a large turbulent velocity is interpreted as the failed wind, which is expected to be formed at the innermost region of the disk in the UV-line driven

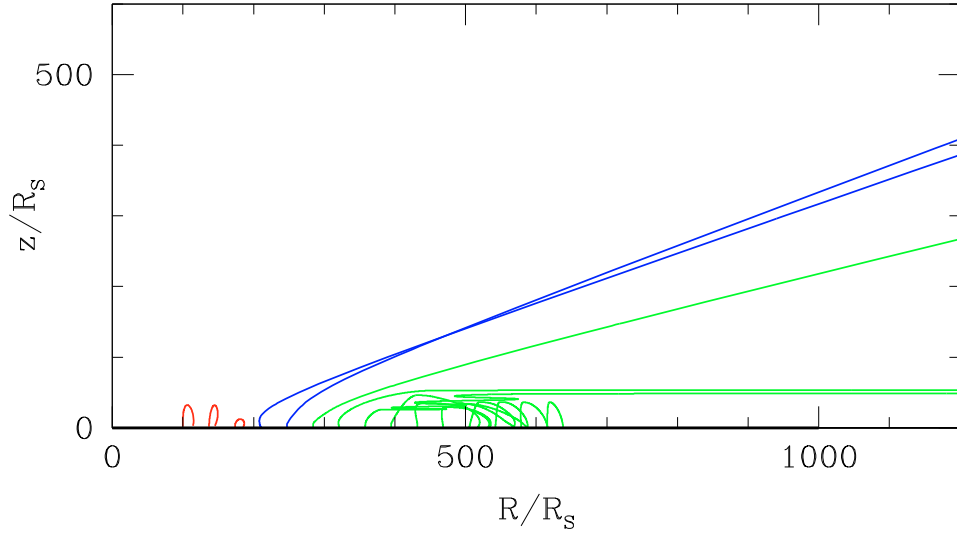


Figure 8.9: The wind geometry calculated by a non-hydrodynamical method. The failed wind is shown in red lines. This figure is taken from Risaliti & Elvis (2010).

wind model (e.g., Murray & Chiang, 1995; Proga & Kallman, 2004; Risaliti & Elvis, 2010; Nomura et al., 2013). In the failed wind, materials are lifted up from the disk, but do not reach to the escape velocity. Thus, the materials eventually turn back to the disk as shown by red lines in Fig. 8.9. This up-and-down motion generates a large turbulent velocity less than the escape velocity.

The large bulk velocity of $\gtrsim 0.15c$ required in our analysis is also understandable with the failed wind. In the vertical direction, the failed wind should not have such a large bulk velocity because the upward velocity is cancelled by the downward velocity. However, in the horizontal direction, the failed wind can have a large bulk velocity because the failed wind is pushed sideways by the radiation from the inner disk (see Fig. 8.9). If we observe the failed wind from a relatively high inclination like the line of sight labeled “Complex NLS1” in Fig. 8.10, a large bulk velocity can be observed.

In the context of UV line driven disk wind model, low mass black hole systems like 1H 0707-495 cannot accelerate to such a high velocity as high mass systems, but form the failed wind (e.g., Gardner & Done, 2014). This is because in the low mass systems, the accretion disk temperature is hotter than the high mass systems (see Fig. 7.5). Therefore, our model with a large turbulence can be understood by the UV-line driving scenario. Since PDS 456 and APM 08279+5255 can be well explained by the UV-line driving as discussed in Chapter 7, all the UFOs we analyzed are understandable within the same scenario.

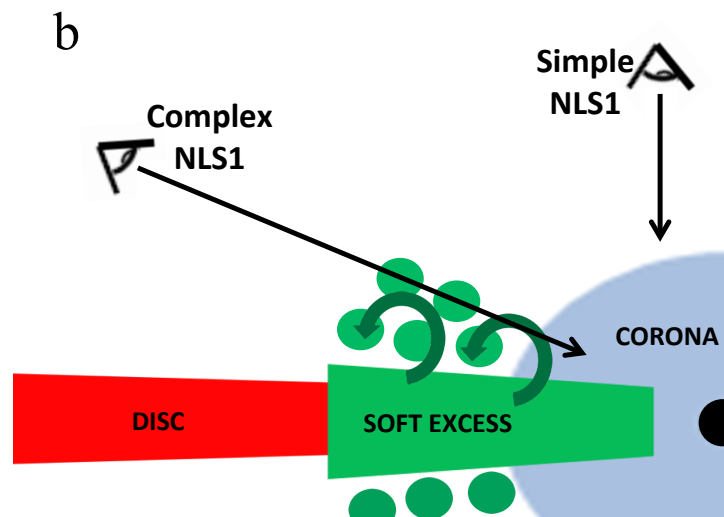


Figure 8.10: A schematic view of the failed wind in the low mass systems such as narrow line Seyfert 1s. This figure is taken from Gardner & Done (2014).

Chapter 9

Conclusion

We have newly developed an X-ray spectral model for the ultra-fast outflows by assuming the realistic geometry and the distributions of the velocity and density. In order to investigate the origin of variation of the UFO spectra, we applied such a realistic spectral model to a variety of observational data of the UFOs (PDS 456 and APM 08279+5255) for the first time. Based on our analysis, we obtained the following results.

- Most importantly, all the spectra of PDS 456 and APM 08279+5255 in different observational epochs have been successfully reproduced while keeping all the fundamental parameters constant except for the terminal velocity and the outflowing angle. The other explanations such as the inhomogeneity of the wind can not be rejected, but this result indicates a possibility that the spectral variability of the UFO is caused by the instability of the outflowing angle of the wind.
- The mass outflow rate of $\dot{M}_{\text{wind}}/\dot{M}_{\text{Edd}} = 0.09\text{--}0.13$ and $\dot{M}_{\text{wind}}/\dot{M}_{\text{Edd}} = 0.18$ are obtained for PDS 456 and APM 08279+5255, respectively. These values are consistent with the values expected by the theoretical calculation of the UV-line driven disk wind.
- By comparing the observed emission line structure in PDS 456 with our simulations, the inner angle of the wind is found to be $\sim 35^\circ$. If the disk reflection component is dominant in the emission line structure, it is $\sim 55^\circ$. This is the first time that the wind angle has been constrained by using the emission line structure.

We also analyzed a peculiar AGN 1H 0707-495, whose spectra show a steep spectral drop above ~ 7 keV, with our disk wind models. Although many attempts to explain the origin of this spectral feature have been made, no one has tried to explain this as a UFO. We tried to reproduce the observed spectra with a realistic disk wind model for the first time, and obtained following results.

-
- All the observed spectra are reproduced by our wind model with a mass outflow rate of $\dot{M}_{\text{wind}}/\dot{M}_{\text{Edd}} = 0.20$ and a terminal velocity of $v_{\infty} = 0.2c$. Therefore, the peculiar spectra of 1H 0707-495 can be interpreted as a UFO. The obtained values are also similar to PDS 456 and APM 08279+5255 despite the large difference of the black hole masses, which are $\sim 10^{9-10} M_{\odot}$ for PDS 456 and APM 08279+5255 and $\sim 10^6 M_{\odot}$ for 1H 0707-495. This result implies that the UFOs are launched independently of the black hole mass.
 - A wind model with a large turbulent velocity $v_t = 10000 \text{ km s}^{-1}$ and a slower terminal velocity $v_{\infty} = 0.15c$ also reproduce the observed spectra, giving comparably good fits with the model similar to PDS 456. This model can be interpreted as a “failed wind” which is theoretically expected in the UV-line driven wind model (Gardner & Done, 2014).

Our analysis demonstrated the power of the Monte Carlo simulations of the wind for probing the geometry and physical conditions of the wind, but with current instruments, our simulations are applicable to only a few sources. The future X-ray missions such as *ASTRO-H* and *Athena* will enable us to observe a large number of UFOs with an extremely improved data quality. By applying our simulations to such high quality data, the physical mechanism of the UFOs will be revealed, and also their importance in the coevolution of black holes and galaxies will be established.

Bibliography

- Agostinelli S. et al., 2003, Nuclear Instruments and Methods in Physics Research Section A: Accelerators, Spectrometers, Detectors and Associated Equipment, 506, 250
- Allen J. T., Hewett P. C., Maddox N., Richards G. T., Belokurov V., 2011, MNRAS, 410, 860
- Allison J. et al., 2006, IEEE TRANSACTIONS ON NUCLEAR SCIENCE, 53, 270
- Antonucci R., 1993, ARA&A, 31, 473
- Antonucci R. R. J., Miller J. S., 1985, ApJ, 297, 621
- Awaki H., Koyama K., Inoue H., Halpern J. P., 1991, PASJ, 43, 195
- Begelman M. C., McKee C. F., Shields G. A., 1983, ApJ, 271, 70
- Behar E., Kaspi S., Reeves J., Turner T. J., Mushotzky R., O'Brien P. T., 2010, ApJ, 712, 26
- Bentz M. C., Peterson B. M., Netzer H., Pogge R. W., Vestergaard M., 2009a, ApJ, 697, 160
- Bentz M. C., Peterson B. M., Pogge R. W., Vestergaard M., 2009b, ApJ, 694, L166
- Bentz M. C. et al., 2009c, ApJ, 705, 199
- Blandford R. D., McKee C. F., 1982, ApJ, 255, 419
- Blomme R., 1990, A&A, 229, 513
- Blustin A. J., Page M. J., Fuerst S. V., Branduardi-Raymont G., Ashton C. E., 2005, A&A, 431, 111
- Boehringer H., Voges W., 1993, MNRAS, 264, L25

Boller T. et al., 2002, MNRAS, 329, L1

Brenneman L. W. et al., 2014, ApJ, 788, 61

Castor J. I., Abbott D. C., Klein R. I., 1975, ApJ, 195, 157

Chartas G., Brandt W. N., Gallagher S. C., Garmire G. P., 2002, ApJ, 579, 169

Chartas G., Saez C., Brandt W. N., Giustini M., Garmire G. P., 2009, ApJ, 706, 644

Ciotti L., Ostriker J. P., Proga D., 2010, ApJ, 717, 708

Dadina M., 2008, A&A, 485, 417

Dewangan G. C., Griffiths R. E., Dasgupta S., Rao A. R., 2007, ApJ, 671, 1284

Done C., 2010, ArXiv e-prints

Done C., Davis S. W., Jin C., Blaes O., Ward M., 2012, MNRAS, 420, 1848

Done C., Sobolewska M. A., Gierlinski M., Schurch N. J., 2007, MNRAS, 374, L15

Draine B., 2010, Physics of the Interstellar and Intergalactic Medium, Princeton Series in Astrophysics. Princeton University Press

Egami E., Neugebauer G., Soifer B. T., Matthews K., Ressler M., Becklin E. E., Murphy, Jr. T. W., Dale D. A., 2000, ApJ, 535, 561

Elvis M., 2000, ApJ, 545, 63

Fabian A., 2012, ARA&A, 50, 455

Fabian A. C., Miniutti G., Gallo L., Boller T., Tanaka Y., Vaughan S., Ross R. R., 2004, MNRAS, 353, 1071

Fabian A. C., Sanders J. S., Allen S. W., Crawford C. S., Iwasawa K., Johnstone R. M., Schmidt R. W., Taylor G. B., 2003, MNRAS, 344, L43

Fabian A. C. et al., 2009, Nature, 459, 540

Ferrarese L., Merritt D., 2000, ApJ, 539, L9

Fukumura K., Kazanas D., Contopoulos I., Behar E., 2010, ApJ, 715, 636

Gallo L. C., Tanaka Y., Boller T., Fabian A. C., Vaughan S., Brandt W. N., 2004, MNRAS, 353, 1064

- Ganguly R., Brotherton M. S., 2008, *ApJ*, 672, 102
- Gardner E., Done C., 2014, arXiv preprint arXiv:1411.6425, 14, 1
- Gibson R. R. et al., 2009, *ApJ*, 692, 758
- Gofford J. et al., 2014, *ApJ*, 784, 77
- Gofford J., Reeves J. N., Tombesi F., Braito V., Turner T. J., Miller L., Cappi M., 2013, *MNRAS*, 430, 60
- Goulding A. D., Alexander D. M., Lehmer B. D., Mullaney J. R., 2010, *MNRAS*, 406, 597
- Gültekin K. et al., 2009, *ApJ*, 698, 198
- Hagino K., Odaka H., Done C., Gandhi P., Watanabe S., Sako M., Takahashi T., 2015, *MNRAS*, 446, 663
- Hamann F., Korista K. T., Morris S. L., 1993, *ApJ*, 415, 541
- Hasinger G., Schartel N., Komossa S., 2002, *ApJ*, 573, L77
- Hewett P. C., Foltz C. B., 2003, *AJ*, 125, 1784
- Higginbottom N., Proga D., Knigge C., Long K. S., Matthews J. H., Sim S. A., 2014, *ApJ*, 789, 19
- Howarth I. D., Prinja R. K., 1989, *ApJS*, 69, 527
- Irwin M. J., Ibata R. A., Lewis G. F., Totten E. J., 1998, *ApJ*, 505, 529
- Jansen F. et al., 2001, *A&A*, 365, L1
- Jin C., Ward M., Done C., 2012, *MNRAS*, 425, 907
- Jin C., Ward M., Done C., Gelbord J., 2012, *MNRAS*, 420, 1825
- Kaastra J. S. et al., 2014, *Science*, 345, 64
- Kaastra J. S. et al., 2014, ArXiv e-prints
- Kallman T. R., Palmeri P., Bautista M. A., Mendoza C., Krolik J. H., 2004, *ApJS*, 155, 675

-
- Kaspi S., Smith P. S., Netzer H., Maoz D., Jannuzi B. T., Giveon U., 2000, *ApJ*, 533, 631
- Katayama H., Takahashi I., Ikebe Y., Matsushita K., Freyberg M. J., 2004, *A&A*, 414, 767
- Kellermann K. I., Sramek R., Schmidt M., Shaffer D. B., Green R., 1989, *AJ*, 98, 1195
- King A., 2003, *ApJ*, 596, L27
- King A. R., 2010, *MNRAS*, 402, 1516
- King A. R., Pounds K. A., 2003, *MNRAS*, 345, 657
- Knigge C., Woods J. A., Drew J. E., 1995, *MNRAS*, 273, 225
- Komossa S., 2008, *Rev. Mex. Astron. Astrophys*, 92, 86
- Kormendy J., Ho L. C., 2013, *ARA&A*, 51, 511
- Kormendy J., Richstone D., 1995, *ARA&A*, 33, 581
- Kotani T., Ebisawa K., Dotani T., Inoue H., Nagase F., Tanaka Y., Ueda Y., 2000, *ApJ*, 539, 413
- Koyama K. et al., 2007, *PASJ*, 59, S23
- Krips M., Peck A. B., Sakamoto K., Petitpas G. B., Wilner D. J., Matsushita S., Iono D., 2007, *ApJ*, 671, L5
- Lamers H., Cerruti-Sola M., Perinotto M., 1987, *ApJ*, 314, 726
- Laor A., Davis S. W., 2014, *MNRAS*, 438, 3024
- Lawrence A., Elvis M., 1982, *ApJ*, 256, 410
- Lewis G. F., Carilli C., Papadopoulos P., Ivison R. J., 2002, *MNRAS*, 330, L15
- Longair M., 2011, *High Energy Astrophysics*. Cambridge University Press
- Lubiński P., Zdziarski A. A., Walter R., Paltani S., Beckmann V., Soldi S., Ferrigno C., Courvoisier T. J.-L., 2010, *MNRAS*, 408, 1851
- Marconi A., Risaliti G., Gilli R., Hunt L. K., Maiolino R., Salvati M., 2004, *MNRAS*, 351, 169

- McKernan B., Yaqoob T., Reynolds C. S., 2007, MNRAS, 379, 1359
- McLure R. J., Jarvis M. J., 2002, MNRAS, 337, 109
- Merritt D., Ferrarese L., 2001, ApJ, 547, 140
- Misawa T., Charlton J. C., Eracleous M., Ganguly R., Tytler D., Kirkman D., Suzuki N., Lubin D., 2007, ApJ Supplement Series, 171, 1
- Mitsuda K., Bautz M., Inoue H., Kelley R., Koyama K., Kunieda H., Makishima K., Ogawara Y., 2007, PASJ, 59, 1
- Miyoshi M., Moran J., Herrnstein J., Greenhill L., Nakai N., Diamond P., Inoue M., 1995, Nature, 373, 127
- Murray N., Chiang J., 1995, ApJ, 454, L105
- Nelson C. H., 2000, ApJ, 544, L91
- Nomura M., 2014, PhD thesis, Ochanomizu University
- Nomura M., Ohsuga K., Wada K., Susa H., Misawa T., 2013, PASJ, 65, 40
- Odaka H., Aharonian F., Watanabe S., Tanaka Y., Khangulyan D., Takahashi T., 2011, ApJ, 740, 103
- Ojha R., Zacharias N., Hennessy G. S., Gaume R. A., Johnston K. J., 2009, AJ, 138, 845
- Osterbrock D., Ferland G., 2006, Astrophysics of Gaseous Nebulae and Active Galactic Nuclei. University Science Books
- Osterbrock D. E., Pogge R. W., 1985, ApJ, 297, 166
- Owocki S., 2000, Encyclopedia of A&A, 1
- Owocki S., 2004, EAS Publications Series, 13, 163
- Pauldrach A., Puls J., Kudritzki R., 1986, A&A, 164, 86
- Peterson B., 1997, An Introduction to Active Galactic Nuclei. Cambridge University Press
- Peterson B. M., 2013, Space Science Reviews, 183, 253

-
- Peterson B. M. et al., 2004, *ApJ*, 613, 682
- Piconcelli E., Jimenez-Bailón E., Guainazzi M., Schartel N., Rodríguez-Pascual P. M., Santos-Lleó M., 2005, *A&A*, 432, 15
- Pounds K., Done C., Osborne J. P., 1995, *MNRAS: Letters*, 277, L5
- Pounds K. A., King A. R., Page K. L., O'Brien P. T., 2003a, *MNRAS*, 346, 1025
- Pounds K. A., Reeves J. N., King A. R., Page K. L., O'Brien P. T., Turner M. J. L., 2003b, *MNRAS*, 345, 705
- Proga D., 2007, in *Astronomical Society of the Pacific Conference Series*, Vol. 373, *The Central Engine of Active Galactic Nuclei*, Ho L. C., Wang J.-W., eds., p. 267
- Proga D., Kallman T. R., 2004, *ApJ*, 616, 688
- Proga D., Stone J., Kallman T., 2000, *ApJ*, 10, 686
- Reeves J., O'Brien P., Ward M., 2003, *ApJ*, 593, L65
- Reeves J. N. et al., 2014, *ApJ*, 780, 45
- Reeves J. N. et al., 2009, *ApJ*, 701, 493
- Reeves J. N., Wynn G., O'Brien P. T., Pounds K. A., 2002, *MNRAS*, 336, L56
- Reynolds C. S., 2012, *ApJ*, 759, L15
- Riechers D. A., Walter F., Carilli C. L., Lewis G. F., 2009, *ApJ*, 690, 463
- Risaliti G., Elvis M., 2004, in *Astrophysics and Space Science Library*, Vol. 308, *Supermassive Black Holes in the Distant Universe*, Barger A. J., ed., p. 187
- Risaliti G., Elvis M., 2010, *A&A*, 516, A89
- Rybicki G., Lightman A., 2008, *Radiative Processes in Astrophysics*, Physics textbook. Wiley
- Saez C., Chartas G., 2011, *ApJ*, 737, 91
- Saez C., Chartas G., Brandt W. N., 2009, *ApJ*, 697, 194
- Sako M. et al., 2001, *A&A*, 365, L168
- Schurch N. J., Done C., 2007, *MNRAS*, 381, 1413

- Serlemitsos P. J. et al., 2007, PASJ, 59, S9
- Shemmer O., Brandt W. N., Netzer H., Maiolino R., Kaspi S., 2006, ApJ, 646, L29
- Shemmer O., Brandt W. N., Netzer H., Maiolino R., Kaspi S., 2008, ApJ, 682, 81
- Shemmer O., Netzer H., Maiolino R., Oliva E., Croom S., Corbett E., di Fabrizio L., 2004, ApJ, 614, 547
- Shlosman I., Vitello P., 1993, ApJ, 409, 372
- Silk J., Rees M., 1998, A&A, 331, L1
- Sim S. A., Long K. S., Miller L., Turner T. J., 2008, MNRAS, 388, 611
- Sim S. A., Miller L., Long K. S., Turner T. J., Reeves J. N., 2010a, MNRAS, 404, 1369
- Sim S. A., Proga D., Miller L., Long K. S., Turner T. J., 2010b, MNRAS, 408, 1396
- Simpson C., 2005, MNRAS, 360, 565
- Solomon P., Vanden Bout P., 2005, ARA&A, 43, 677
- Spitzer L., 1978, Physical Processes in the Interstellar Medium, A Wiley-Interscience Publication. John Wiley
- Stevens I. R., Kallman T. R., 1990, ApJ, 365, 321
- Strüder L. et al., 2001, A&A, 365, L18
- Sulentic J. W., Bachev R., Marziani P., Negrete C. A., Dultzin D., 2007, ApJ, 666, 757
- Takahashi T. et al., 2012, in Society of Photo-Optical Instrumentation Engineers (SPIE) Conference Series, Vol. 8443, Society of Photo-Optical Instrumentation Engineers (SPIE) Conference Series, p. 1
- Tanaka Y., Boller T., Gallo L., Keil R., Ueda Y., 2004, PASJ, 56, L9
- Tarter C. B., Tucker W. H., Salpeter E. E., 1969, ApJ, 156, 943
- Tatum M. M., Turner T. J., Sim S. A., Miller L., Reeves J. N., Patrick A. R., Long K. S., 2012, ApJ, 752, 94

-
- Thompson A., Lindau I., Attwood D., Liu Y., Gullikson E., Pianetta P., Howells M., Robinson A., Kim K., Scofield J., Kirz J., Underwood J., Kortright J., Williams G., Winick H., eds., 2009, X-ray Data Booklet. Lawrence Berkeley National Laboratory, University of California
- Tombesi F., Cappi M., Reeves J. N., Nemmen R. S., Braito V., Gaspari M., Reynolds C. S., 2013, MNRAS, 430, 1102
- Tombesi F., Cappi M., Reeves J. N., Palumbo G. G. C., Yaqoob T., Braito V., Dadina M., 2010, A&A, 521, A57
- Tremaine S. et al., 2002, ApJ, 574, 740
- Turner M. J. L. et al., 2001, A&A, 365, L27
- Urry C. M., Padovani P., 1995, Publications of the Astronomical Society of the Pacific, 107, 803
- Vasudevan R. V., Fabian A. C., 2007, MNRAS, 381, 1235
- Véron-Cetty M.-P., Véron P., Gonçalves A. C., 2001, A&A, 372, 730
- Vestergaard M., Peterson B. M., 2006, ApJ, 641, 689
- Wandel A., Peterson B. M., Malkan M. A., 1999, ApJ, 526, 579
- Wang J.-M., Netzer H., 2003, A&A, 398, 927
- Wang J.-M., Watarai K.-Y., Mineshige S., 2004, ApJ, 607, L107
- Watanabe S. et al., 2006, ApJ, 651, 421
- Wei A., Downes D., Neri R., Walter F., Henkel C., Wilner D. J., Wagg J., Wiklind T., 2007, A&A, 467, 955
- Weymann R. J., Morris S. L., Foltz C. B., Hewett P. C., 1991, ApJ, 373, 23

Acknowledgements

I would like to express my best gratitude to Prof. Tadayuki Takahashi who has been guiding and encouraging me over the 5 years of my graduate course. I am also deeply grateful to Dr. Hirokazu Odaka who has been continuously advising me and giving precise and useful comments on data analysis, simulations and astrophysics. His simulation code MONACO is essential for this thesis. I would also like to thank Dr. Shin Watanabe and Prof. Masao Sako for their great contributions to developing the MONACO.

I greatly appreciate Prof. Chris Done for giving me the opportunities to stay in Durham. She also strongly supported me throughout this work, which started from her idea. I also express my thanks to Dr. Poshak Gandhi who also helped me in Durham. Moreover, he have been continuously supported me since he was in ISAS. He is my first teacher of AGN.

I thank all colleagues in ISAS. Especially, Dr. Lukasz Stawarz has been helped me for 5 years by giving me interesting scientific topics. I really enjoyed the work in collaboration with him.

Finally, I greatly thank my family for supporting me. My wife always supported me even when she was really exhausted by her work, taido and child rearing. My son healed me by his cute smile.